THE ANALYSIS AND TESTING OF MEMS AND MACRO SCALE PIEZOELECTRIC DEVICES

by

Ryan Robert Knight

B.S. in Mechanical Engineering, University of Pittsburgh, 2005

Submitted to the Graduate Faculty of

the School of Engineering in partial fulfillment

of the requirements for the degree of

Master of Science

University of Pittsburgh

2007

UNIVERSITY OF PITTSBURGH

SCHOOL OF ENGINEERING

This thesis was presented

by

Ryan Knight

It was defended on

June 20th, 2007

and approved by

Dr. Daniel G. Cole, Associate Professor, Department of Mechanical Engineering and Materials Science

Dr. Jeffrey S. Vipperman, Associate Professor, Department of Mechanical Engineering and Materials Science

Dr. Lisa Mauck Weiland, Assistant Professor, Department of Mechanical Engineering and Materials Science

Thesis Advisor: Dr. William W. Clark, Professor, Department of Mechanical Engineering and Materials Science

Copyright © by Ryan Robert Knight

2007

THE ANALYSIS AND TESTING OF MEMS AND MACRO SCALE PIEZOELECTRIC DEVICES

Ryan Robert Knight, M.S.

University of Pittsburgh, 2007

Piezoelectric materials are incorporated into many of today's commercial and research devices. Accelerometers, crystal oscillators, sonar devices, audio transducers, igniters, position systems, and vibration absorbers are to name a few. The applications associated with piezoelectricity can be categorized into three groups: 1) sensors, 2) actuators, and 3) energy harvesters. Clark (2000), Lesieutre (2004) and Muriuki (2004) illustrate a shunt method technique that can tune the stiffness of sensors, actuators and energy harvesters. This thesis focuses on the two common designs (d_{31} or d_{33} structure) associated with the piezoelectric device applications. MEMS interdigitated electrode beams are frequency tested via μLDV and showed to be tunable. Additionally, optimal interdigitated electrode layouts are investigated and reported. A design methodology is provided to help one conclude what type of piezoelectric device should be developed.

TABLE OF CONTENTS

NOMENCLATURE .... **XIII**

ACKNOWLEDGEMENTS .... **XVI**

1.0 INTRODUCTION **1**

2.0 LITERATURE REVIEW **3**

2.1 PIEZOELECTRIC MATERIALS **3**

2.1.1 Domain Poling **4**

2.1.2 Piezoelectric Notation **5**

2.1.3 Mechanical-Electrical Coupling **7**

2.1.4 Capacitance Model **11**

2.2 PROCESSING OF PZT **13**

2.3 ENERGY HARVESTING **16**

2.3.1 Quantifying Energy **17**

2.3.2 d_{31} and d_{33} Modes **18**

2.3.3 MEMS Energy Harvesting **20**

2.4 TUNING **22**

3.0 MATHEMATICAL PIEZOELECTRIC BEAM MODELS **24**

3.1 LINEAR PIEZOELECTRICITY **25**

3.2 STATIC BENDING MODELS **26**

3.2.1 Unimorph d_{31} Beam model 30

3.2.2 Interdigitated Unimorph d_{33} Beam Model 33

3.2.3 Comparing Unimorphs 35

3.3 DYNAMIC BENDING MODEL 37

3.4 MATHEMATICAL MODEL INACCURACIES 41

3.4.1 Clamped End Effect 42

3.4.2 Linear Bending Assumption 43

3.4.3 Neglecting Damping 45

3.4.4 Neglecting Shear Stress 46

4.0 MEMS BEAM DESIGN AND PROCESSING 47

4.1 DIE DESIGN 47

4.2 PROCESSING STEPS 48

4.3 XEON DIFLUORIDE ETCHING 50

4.4 PHOTORESIST REMOVAL 53

4.5 CURLING OF BEAMS 54

4.6 XEON DIFLUORIDE UNDERCUT 59

5.0 MODAL FININTE ELEMENT ANALYSIS 62

5.1 FEA BEAM MODEL 63

5.1.1 Diagonal Beam 64

5.1.2 Trapezoidal Beam 66

5.1.3 Simulation Results 67

5.2 MODELING UNDERCUT 68

5.3 MODELING BEAM CURL 70

5.4 COMPARING THE UNDERCUT AND CURVED FEA MODEL 71

6.0 FREQUENCY TESTING AND EXPERIMENTATION 73

6.1 LASER DOPPLER VIBROMETER FREQUENCY AND MODE SHAPE TESTING 73

6.1.1 Wire Bonding 74

6.1.2 Poling the MEMS d_{33} IDE Beams 76

6.1.3 Vibration Stage 78

6.1.4 MEMS µLDV and Mode Shape Measurements 82

6.1.5 µLDV Results 89

6.2 MACRO-SCALE OPEN CIRCUIT TESTING 91

6.3 RESULTS SUMMARY 95

7.0 INTERDIGITATED ELECTRODE ANALYSIS AND OPTIMIZATION 96

7.1 SIMULATION OF POLING ELECTRIC FIELD 96

7.2 IDE ELECTRO-MECHANICAL LOSS 99

7.3 INTERDIGITATED ELECTRODE FEA OPTIMIZATION 100

7.4 PLANAR INTERDIGITATED ELECTRODE LOSS 107

7.5 INTERDIGITATED RESULTS SUMMARY 109

8.0 CONCLUSION 112

8.1 FUTURE WORK 113

APPENDIX A 116

BIBLIOGRAPHY 117

LIST OF TABLES

Table 1. The transformation from indicial notation to engineering notation................................ 6

Table 2. Plane stress and plane strain simplified constitutive equations 26

Table 3. The equations for plane strain/stress for each beam design (Figures 2.6 and 2.7) 30

Table 4. Parameters used to equate the deflections shown in Figure 3.8 45

Table 5. Different layer thicknesses.. 49

Table 6. CMU's XeF_2 dry etching parameters.. 50

Table 7. Pitt's XeF_2 dry etching parameters 52

Table 8. Mechanical properties and residual stresses of films deposited in Jeon (2005) 55

Table 9. Residual stress values for various beams across the wafer.. 58

Table 10. Material property values used in FEA model in μMKS units 63

Table 11. Simulation results from the diagonal and trapezoidal d_{33} unimorph beam model....... 68

Table 12. Compares a single layer beam with and with out an undercut 69

Table 13. Compares single layer beam natural frequencies with and without an initial curvature 71

Table 14. First vibration measurement data and calculated surface spring constants 80

Table 15. The experimental and simulation percent tuning... 90

Table 16. Electrical values used for IDE Optimization 101

Table 17. Values obtained from FEA for the percent output of PZT that is poled in the Length/3-Direction with respect to electrode spacing 106

Table 18. Total of PZT poled in the length direction for diagonal and trapezoidal beams 110

LIST OF FIGURES

Figure 2.1. A d_{31} unimorph fixed-free beam having an end load in the negative 3 direction. A negative voltage is produced when this structure is deflected downwards 8

Figure 2.2. A small volume of PZT from the loaded structured depicted in Figure 2.1................ 8

Figure 2.3. A d_{33} unimorph fixed-free beam having an end load in the negative 1 direction. A positive voltage is produced when this structure is deflected downwards 9

Figure 2.4. A small volume of PZT from the loaded structured depicted in Figure 2.3.............. 10

Figure 2.5. a) d_{33} b) d_{31} c) d_{32} d) d_{15} and e) d_{24} 10

Figure 2.6. Typical d_{33} energy harvester... 18

Figure 2.7. Typical d_{31} energy harvester... 19

Figure 3.1. Beam deflection plot for both the plane strain and plane stress 28

Figure 3.2. Weighted modulus method for composite beams 29

Figure 3.3. Unimorph d_{31} beam 31

Figure 3.4. Typical interdigitated unimorph d_{33} beam... 34

Figure 3.5. Magnified view of the piezoelectric layer of IDE d_{33} beam.................................... 34

Figure 3.6. A d_{33} unimorph cantilever beam illustrating the areas underneath the electrode that have different stiffness properties 39

Figure 3.7. The y-stress of cantilever plate that is deflected into the page.................................. 42

Figure 3.8. Plot represents the cantilever beam deflection for a linear and nonlinear model....... 44

Figure 4.1. The die design for the mask layout... 48

Figure 4.2. "Process Plan 2: RIE BCl_3:Cl_2 Step after Electrode Patterning"(Frederick, 2006) ... 49

Figure 4.3. Horizontal and vertical etch rates for a 20μm opening using the process parameters in Table 6 51

Figure 4.4. Horizontal and vertical etch rates for a larger opening using the process parameters in Table 6 52

Figure 4.5. SEM photograph of the released beams 54

Figure 4.6. Plot of the internal stress gradient of a beam after release but before bending........ 57

Figure 4.7. Diagonal beam, (110) direction, with a large etching channel illustrating the undercut resulting from the XeF_2 etching 60

Figure 4.8. Transverse beam, (100) direction, with a small etching channel illustrating the undercut resulting from the XeF_2 etching 60

Figure 5.1. The diagonal d_{33} unimorph beam model illustrating the alternating poling directions 64

Figure 5.2. The dimensions of the trapezoidal d_{33} unimorph beam 67

Figure 5.3. The diagonal d_{33} unimorph model with an undercut 69

Figure 5.4. Single layer curve beam FEA model 70

Figure 6.1. Trapezoidal beam illustrating the wire bonded to the gold pads 75

Figure 6.2. MEMS piece wire bonded to chip 76

Figure 6.3. Illustration of a beam that literally exploded during poling. This was the result from an electric field that was too large 78

Figure 6.4. Overhead view of the low-pass vibration stage used 79

Figure 6.5. The frequency response of the vibration stage when the PZT shaker is excited........ 81

Figure 6.6. Schematic of the μLDV measuring system used at CMU 83

Figure 6.7. Diagonal Beam Excitation- Displacement-out per displacement-in frequency response 84

Figure 6.8. Base Excitation, Open Circuit Diagonal Beam- Displacement-out per displacement-in frequency response 85

Figure 6.9. Base Excitation, Short Circuit Diagonal Beam- Displacement-out per displacement-in frequency response ... 86

Figure 6.10. Trapezoidal Beam Excitation- Displacement-out per displacement-in frequency response ... 87

Figure 6.11. Trapezoidal Beam– Open and short circuit frequency response for the 1st mode ... 88

Figure 6.12. Trapezoidal Beam– Open and short circuit frequency response for the 2nd mode ... 88

Figure 6.13. Plot illustrates how the OC frequency can be shifted if the beam's electrode is partially removed ... 93

Figure 6.14. Close up of the second mode ... 94

Figure 7.1. 3-D FEA model of the diagonal beam ... 97

Figure 7.2. Electric field between two electrodes for the diagonal beam ... 98

Figure 7.3. Illustration of the non-uniform electric field that exists underneath the electrodes during poling ... 99

Figure 7.4. 2-D ANSYS model with variable dimensions ... 101

Figure 7.5. ANSYS IDE spacing optimization for various electrode width to piezoelectric layer thickness ratios ... 103

Figure 7.6. The percent output associated for increasing electrode width to thickness ratios and various spacing ... 105

Figure 7.7. Top view of IDE layout ... 107

Figure 7.8. % of poling plot under a constant electric field for the IDE layout in Figure 7.6 ... 108

NOMENCLATURE

Notation	Description	Units
A_c	Area	square meter
C	Capacitance	farad
c_{ijkl}^E, c_{pq}	Elastic stiffness constant	newton per square meter
d_{ijk}, d_{ij}	Piezoelectric constant	meter per volt
dU	Stored energy density	
D_i	Electric displacement component	coulomb per square meter
e_{ijk}, e_{ip}	Piezoelectric constant	coulomb per square meter
E	Isotropic Young's modulus	newton per square meter
E_c	Energy of capacitor	joule
E_k	Electric field component	volt per meter
$E_3(s)$	Electric field	volt per meter
^{E} (superscript)	At constant electric field	
f	Frequency	hertz
f_{oc}	Open circuit frequency	hertz
f_{sc}	Short circuit frequency	hertz
$F_a(s)$	Loading force	newton

g_{ijk}, g_{ip}	Piezoelectric constant	volt meter per Newton
h	Beam thickness	meter
h_m	Metal layer thickness	meter
h_p	Piezoelectric layer thickness	meter
$I(s)$	Current	Ampere
$I_c, I(n)$	Moment of inertia	meter to the fourth power
k, k_{eff}	Stiffness, effective stiffness	newton per meter
K_{31}, K_{33}	Electro-mechanical coupling	
L	Beam length	meter
$M, M(n)$	Moment	newton meter
P	End load	newton
Q	Charge	coulomb
s_i	Electrode spacing	meter
s_{ijkl}, s_{pq}	Elastic compliance constant	square meter per newton
^{S} (superscript)	At constant strain	
$S(s)$	Strain	
S_{ij}, S_i	Strain component	
$T(s)$	Stress	newton per square meter
T_{kl}, T_j	Stress component	newton per square meter
U	Energy	joules
$V, V(s)$	Voltage	volt
w_e	Electrode width	meter

W	Beam width	meter
$Y(s)$	Displacement	meter
z_c	Neutral axis	meter
Z^{EL}	Impedance	ohm
β_{il}^{T}	Impermittivity component	meter per farad
ε_{ik}	Permittivity component	farad per meter
δ, δ_L	Deflection	meter
Δ_f	Percent change in frequency	
ν	Poisson's ratio	
ρ	Radius of curvature	per meter
ρ_m, ρ_p	Mass density	kilogram per cubic meter
ω	Angular frequency ($2\pi f$)	hertz

ACKNOWLEDGEMENTS

First and foremost, I would like to thank Dr. William W. Clark, my academic advisor, for supplying my work with the necessary funds for research. Additionally, the prudent guidance provided by him as a teacher, boss, and friend was proven to be paramount for my academic development.

I would also like to thank Dr. Sandy Hu for her help during the work associated with my thesis. Dr. Hu always provided good direction when I did not know where to go next.

Finally, I would to thank both the people in the Vibration and Control Lab and the Sound, Systems, and Structures Labs. They provided good technical assistance and an atmosphere that made it enjoyable to work around.

1.0 INTRODUCTION

Piezoelectric materials are incorporated into many of today's commercial and research applications. Accelerometers, crystal oscillators, sonar, audio transducers, igniters, positioning systems, and vibrations absorbers are to name a few. The applications associated with piezoelectricity can be categorized into three groups: 1) sensors, 2) actuators, and 3) energy harvesters. The third group is actually a branch from the first group and can be considered quasi-sensing, except the signal is stored rather than measured. However, since energy harvesting has been receiving much attention, it deserves its own category.

A more recent development in the application of piezoelectric materials is the potential for tuning. The mechanical stiffness can be passively or actively controlled thus allowing a change in the mechanical operation of the device. Tuning has an important impact on the manufacture of the piezoelectric device. Manufacturing tolerances can be relaxed which can in turn reduce processing and overhead costs.

The single relation that each piezoelectric category has in common is the electro-mechanical coupling. The electro-mechanical coupling causes the material to produce electrical energy whenever a mechanical load is applied and also works vice versa. Without the electro-mechanical coupling the piezoelectric applications and tuning capability would not exist.

In order to produce adequate and commercially competitive sensors, actuators, and harvesters, the electro-mechanical coupling has to be effectively exploited. The work presented

in this thesis focuses on two types of common piezoelectric mechanical designs and their electro-mechanical coupling. The mechanical designs are the d_{31} unimorph cantilever beam and the d_{33} unimorph cantilever beam. The term unimorph describes a beam that has one piezoelectric layer. These two designs are compared.

Frequency testing is conducted to help quantify the electromechanical coupling. From the frequency testing, the interdigitated electrode design performed poorly and further analysis was explored. The electrode layout was proved to be the main culprit for poor performance. Subsequently, the interdigitated electrode layout was optimized. This was done both mathematically and by finite element analysis.

2.0 LITERATURE REVIEW

In order to understand the MEMS and macro scale piezoelectric applications, piezoelectricity is first reviewed. After the piezoelectric phenomena, material properties, notation and electro-mechanical coupling are also discussed. The processing of a particular piezoelectric material, lead zirconate titanate, is examined. The processing literature review focuses on current techniques used in MEMS fabrication. The first piezoelectric application reviewed is the area of energy harvesting. Analogous to solar panels, piezoelectric energy harvesting uses ambient vibrations that are naturally occurring in a system and converts the vibrations into a more useable electrical energy source. The other application reviewed focuses on the tuning of resonating structures. The ability to tune resonant structures opens up a window of sub-applications such as passive vibration absorbers (Davis, 2003) and adjustable oscillator or frequency sources. Many recent literature sources were found that investigate mechanical structures incorporating piezoelectric materials.

2.1 PIEZOELECTRIC MATERIALS

Piezoelectric materials have the capability to produce a charge when the material is subjected to an applied strain. The Latin word piezo relates to a mechanical pressure and hence the combination of piezo and electric literally means to produce electricity under an applied

pressure. The amount that a material strains under an applied electric field is typically known as the electro-mechanical coupling. Depending on the material, more importantly whether or not it is a piezoelectric ceramic, the electro-mechanical coupling factor can be reversible. Many piezoelectric materials possess the capability to strain under an applied electric field (also known as electrostriction) but cannot produce a voltage under an applied strain because of material symmetry. Conversely, some piezoelectric ceramics, known as ferroelectric ceramics, are reversible and can produce both a strain and electric field under an applied electric field and strain, respectively. Since resonators and likewise energy harvesters rely on reversible piezoelectric materials only the ferroelectric subclass of materials will be covered.

Among the 32 classes of single-crystal piezoelectric materials 11 possess a center of symmetry. These 11 classes locally produce a charge when subjected to an applied strain but because of symmetry the net charge produced across the volume of material is zero. The remaining 21 classes are non-centrosymmetric, and 20 of these exhibits the piezoelectric and electrostrictive effects.

From the 20 available piezoelectric ceramic materials, lead zirconate titante (PZT), possessing the perovskite structure $Pb(Ti,Zr)O_3$, was developed in the 1950s (Baerwald, 1957). PZT is the most widely used piezoelectric ceramic because the material possesses high electro-mechanical coupling factors that increase the overall sensitivity in both actuation and sensing and because it is relatively inexpensive.

2.1.1 Domain Poling

Domains are regions within each grain of the piezoelectric material that have a common orientation of a spontaneous dipole. Since most piezoceramic grains have dipoles that are

randomly oriented, a large electric field must be applied to the material to align dipoles in a common direction. This procedure is referred to as poling which is analogous to the magnetization of magnets (Kouvatov, 2002). After poling many grains never reach their fully oriented value. This is because of intergranular stresses that tend to reverse the polarity of some domains. Therefore, common poling techniques usually apply high electric fields under elevated temperatures making the material as stress free as possible. Manufacturer provided piezoelectric material properties only consider a percentage of the domains being in the correct orientation. In Baerwald (1957) the theoretical maximum polarization for a completely poled ceramic can only reach 83% of the single crystal value.

2.1.2 Piezoelectric Notation

From the linear theory of piezoelectricity (IEEE Std 176-1997) the constitutive equations for the piezoelectric continuum are defined by equations (2.1) and (2.2)

$$S_{ij} = s^{E}_{ijkl} T_{kl} + d_{kij} E_k \tag{2.1}$$

$$D_i = d_{ikl} T_{kl} + \varepsilon^{T}_{ik} E_k \tag{2.2}$$

where, S_{ij} and T_{kl} are the strain and stress component, respectively. D_i and E_k are the electric displacement and electric field component, respectively. The 3rd order tensor, d_{ijk}, and correspondingly g_{ijk} and e_{ijk} dictate the electro-mechanical coupling of piezoelectric materials. The tensors g_{ijk} and e_{ijk} are related to d_{ijk} directly through other material properties. The d_{ijk}, g_{ijk}, and e_{ijk} are referred to as the piezoelectric constants and are related to each other by relations (2.3) and (2.4). From the piezoelectric constitutive equations (2.1-2.2), when the

piezoelectric constants are multiplied by a stress a charge is produced. Superscripts "T" and "E" correspond to the material parameter under constant stress or electric field, respectfully.

$$g_{ijk} = \beta_{il}^{T} d_{ljk} \tag{2.3}$$

$$e_{ijk} = d_{ilm} c_{lmjk}^{E} \tag{2.4}$$

β_{il}^{T} and c_{lmjk}^{E} are impermittivity and elastic stiffness material properties.

In engineering notation (also known as Voigt notation), as stated in Table 1, the d_{ijk} tensor for PZT can be viewed as a 3x6 matrix provided in relation (2.5). Engineering (Voigt) notation consists of replacing *ij* or *kl* by *p* or *q*, where *i, j, k, l* take the values 1, 2, 3 and *p, q* take the values 1, 2 , 3, 4, 5, 6.

Table 1. The transformation from indicial notation to engineering notation

ij or kl	p or q
11	1
22	2
33	3
23 or 32	4
31 or 13	5
12 or 21	6

A *p* or *q* value of 1, 2, 3 refers to a 1, 2, or 3 direction (x,y,z) on the respective 1, 2, or 3 plane. The 4, 5, or 6 *p* or *q* values refer to a 2 or 3 direction, 3 or 1 direction, 1 or 2 direction on

the respective 3 or 2 plane, 1 or 3 plane, and 2 or 1 plane. Relating the *p* or *q* values to stress, the 1, 2, 3 values are normal stresses and the 4, 5, 6 values are shear stresses.

$$[d] = \begin{bmatrix} 0 & 0 & 0 & 0 & d_{15} & 0 \\ 0 & 0 & 0 & d_{24} & 0 & 0 \\ d_{31} & d_{32} & d_{33} & 0 & 0 & 0 \end{bmatrix} \tag{2.5}$$

However, because of symmetries in PZT the [*d*] matrix is more formerly known as relation (2.6)

$$d_{15} = d_{24}$$

$$d_{31} = d_{32}$$

$$[d] = \begin{bmatrix} 0 & 0 & 0 & 0 & d_{15} & 0 \\ 0 & 0 & 0 & d_{15} & 0 & 0 \\ d_{31} & d_{31} & d_{33} & 0 & 0 & 0 \end{bmatrix} \tag{2.6}$$

where $d_{31} < 0$ and both $d_{33}, d_{15} > 0$.

2.1.3 Mechanical-Electrical Coupling

From the IEEE Standard on Piezoelectricity (IEE Std 179-1997), the ith and j^{th} component of d_{ij} are denoted as follows: 1) the direction in which the dipoles are aligned in piezoelectric medium is always denoted as the 3-direction, 2) the corresponding perpendicular planar direction is denoted as the 1-direction and 3) the 2-direction comes from the right handed system where unit vectors

$$e_3 \times e_1 = e_2 \tag{2.7}$$

After the directions are established the ith and jth component of d_{ij} can be thought of as a charge created in the ith direction under a jth direction stress. Figure 2.1 shows a fixed-free beam eliciting the d_{31} component of PZT which will be referred to as a d_{31} unimorph beam.

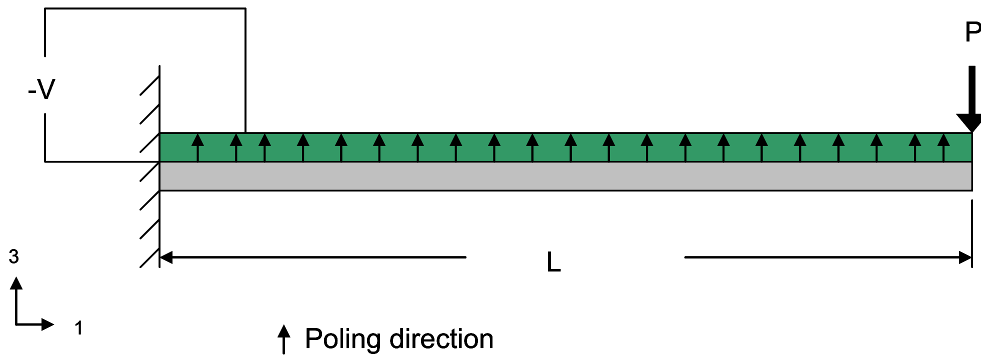

Figure 2.1. A d_{31} unimorph fixed-free beam having an end load in the negative 3 direction. A negative voltage is produced when this structure is deflected downwards

The arrows in Figure 2.1 depict the dipole direction or the poling direction. From this point on, the dipole direction will be referred to as the poling direction (or the 3-direction). Figure 2.2 is a local view of the PZT and the corresponding stresses and electric field.

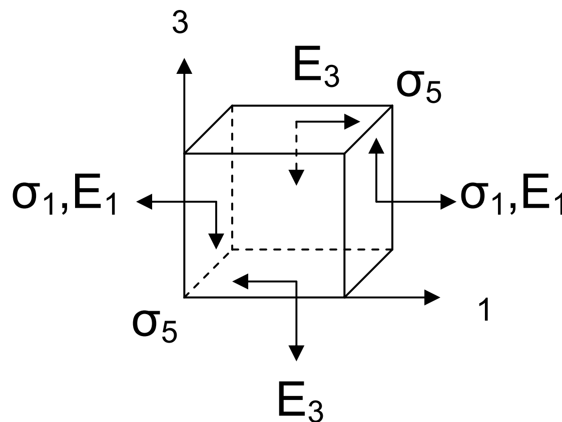

Figure 2.2. A small volume of PZT from the loaded structured depicted in Figure 2.1

Another type of fixed-free beam is poled in the manner to elicit the d_{33} term. This type of fixed-free beam will be referred to as d_{33} unimorph beam. Figure 2.3 illustrates this type of configuration.

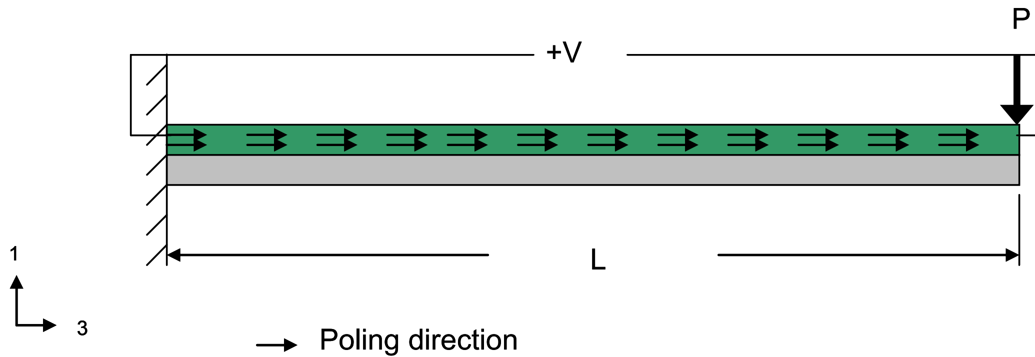

Figure 2.3. A d_{33} unimorph fixed-free beam having an end load in the negative 1 direction. A positive voltage is produced when this structure is deflected downwards

The difficulty with Figure 2.3's layout when considering a length scale greater than 1mm is the extremely high poling voltage required to align the dipoles. However, the interdigitated electrode layout, to be discussed later, lowers the poling voltage alleviating any high voltage concerns that may occur with Figure 2.3 design. Poling procedures and further details will be provided later but PZT manufactures typically require 2-4 V/µm or 2000-4000 V/mm. When the poling length is too long, high voltage arching may occur.

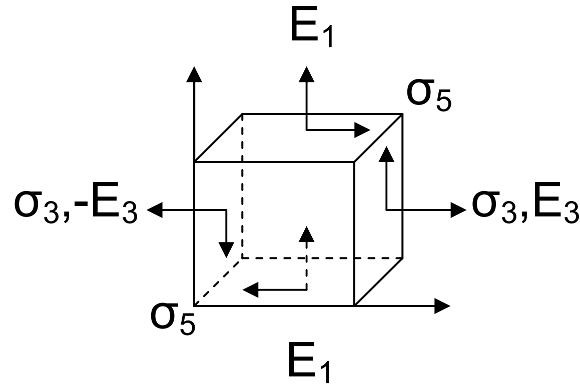

Figure 2.4. A small volume of PZT from the loaded structured depicted in Figure 2.3

Figure 2.4 shows the stresses for the applied load in Figure 2.3 and the corresponding electric fields generated. In both d_{31} and d_{33} unimorph beams, shear stress from the applied load will generate electric fields in the 1 direction. Since the stress perpendicular to the applied load is much greater than the shear stress in the beams, the electric field in the 1-direction is typically ignored. Mathematical reasoning for this is to be provided in Section 3.2. The following 5 cubic arrangements, Figure 2.5, illustrate different types of mechanical loading to elicit the 5 different d_{ij} constants.

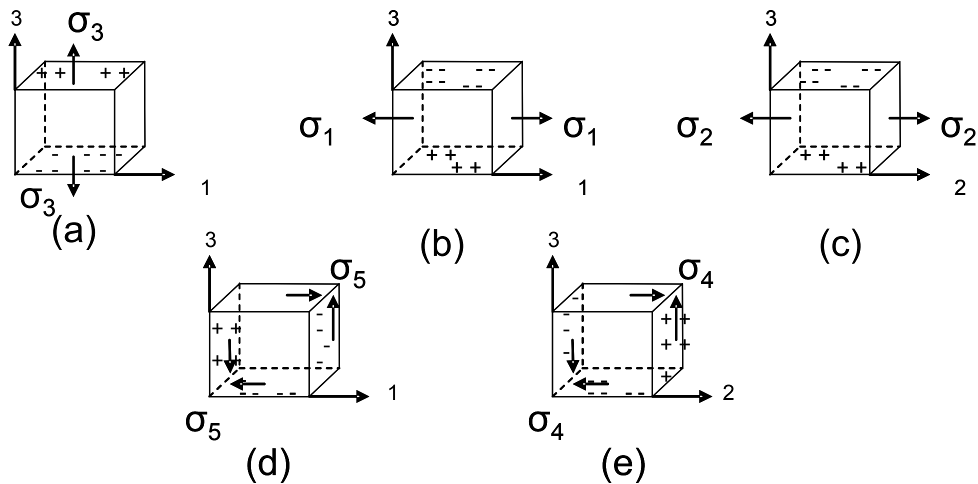

Figure 2.5. a) d_{33} b) d_{31} c) d_{32} d) d_{15} and e) d_{24}

If electrodes are placed on the electric field plane, charge will accumulate on these electrodes and an average voltage will therefore be produced.

2.1.4 Capacitance Model

PZT is a ceramic material that has high permittivity properties. For these reasons PZT structures are modeled and electrically thought of as capacitors. Capacitance in a mechanical sense refers to the stiffness of a structure. Thus, PZT has two types of stiffness: 1) mechanical stiffness from the $[c]$ parameter (material stiffness matrix) and 2) electrical stiffness from capacitance.

The impedance of a capacitor is related to the inverse of its capacitance. Thus, if the electrodes on PZT are electrically connected the capacitance theoretically approaches infinity because of the short circuit (SC) condition. The resulting effect is that the PZT no longer has the electro-mechanical coupling factor and is purely a mechanical structure.

Now consider an electrical model with an inductor and capacitor. Electrical current frequency is proportional to the inverse of capacitance C.

$$f \propto \sqrt{\frac{1}{C}} \tag{2.8}$$

Increasing the capacitance decreases the current frequency and vice versa. Therefore it is postulated that shunting or adding a parallel impedance component such as a capacitor will decrease frequency. Three resources were found that exploited the impedance shunting method. 1) In Clark (2000), he showed that shunting a piezoelectric vibration absorber with a state-switching resistive shunt could semi-actively dissipate energy stored in the absorber. 2) Shunting a piezoelectric element with an energy harvesting circuit (a form of electrical

impedance) was shown in Lesieutre (2004) to decrease the beam's frequency to an operating point somewhere in between open and short circuit frequencies. 3) Muriuki (2004) showed that a piezoelectric resonator could be tuned between open circuit and short circuit frequencies values by varying a shunt capacitor. Frederick (2006) follows the work of Clark (2000) and Muriuki (2004). Frederick investigated methods of increasing the tunability of a resonant structure. She reported that eliciting the d_{33} constant of PZT would result in higher tunability relative to the eliciting the d_{31} constant. At the end of her work, Frederick (2006) fabricated MEMS IDE (interdigitated electrode) beams. The work of this thesis picks up where Frederick (2006) left off.

A piezoelectric structure when excited will vibrate at various modal frequencies. If one considers a purely bending 1st mode frequency, as for a clamped-free cantilever, positive or negative charge will accumulate on the electrode relative to the direction of stress. If the electrodes are short-circuited (SC) the electrical stiffness will reduce to zero and the structure will vibrate at a frequency lower than the open-circuit (OC) frequency.

$$f_{oc} > f_{sc} \tag{2.9}$$

Adding a shunt capacitor to the PZT, as shown in Lesieutre (2004), Muriuki (2004) and Charnegie (2007) can passively tune the structures frequency between f_{oc} and f_{sc}.

In this work, creating structures that utilize the d_{ij} coefficients in a manner to optimize f_{oc} is reviewed and modeled. Certain electrode layouts, poling voltage recipes, structural properties, and geometries can maximize f_{oc}. In order to understand the current research covering piezoelectric structures, PZT and sol-gel processing, energy harvesters, resonators, and vibration tuning are reviewed. The progress and dilemmas are reviewed and identified from the past research.

2.2 PROCESSING OF PZT

Lead zirconate titanate (PZT) has been being produced since the 1950's. Currently, many different companies produce various types of PZT (e.g. hard and soft) and provide sensors and actuators for commercial and laboratory use. Thus, the processing of bulk sheets has been performed for many years and currently only some research has been dedicated to the processing parameters such as changing texture. However, since the advent of MEMS, producing PZT in a manner compatible with MEMS has been becoming more and more attractive.

When thin film PZT first became an attractive area of research many different processing techniques were investigated. Electron-beam evaporation, RF sputtering, ion-beam deposition, epitaxial growth by RF sputtering, magnetron sputtering, MOCVD, laser ablation, screen printing, jet deposition and solid gel (or sol-gel) were all considered and tried as potential fabrication approaches (Kim, 2004 and Sze, 1994). However, as research progressed RF sputtering and sol-gel deposition became the most popular areas of thin film PZT.

Park (2005) investigated the combination of the two processes. He showed that if one first uses the sol-gel method to create a seed layer followed by an RF magnetron sputtering step a highly (100) oriented layer can be created. Additionally, a thick layer of approximately 4μm can be produced crack free. They also showed that highly oriented (100) PZT will subsequently have good piezoelectric material properties.

Although RF magnetron sputtering of PZT produces good piezoelectric properties, there are some drawbacks that can create difficulty during the MEMS processing steps. Rapid thermal annealing can be problematic and can produce cracks throughout the layer. The PZT quality is highly dependent on the processing steps during RF magnetron sputtering and is very susceptible

to processing changes. Because of these discerning processing techniques for RF magnetron sputtering of PZT, processing focus began to veer away from this method.

Sol-gel processing has remained a viable candidate for thin layer PZT and continues to recieve a consistent amount of research attention. Hsueh (1990) showed the superiority of sol-gel PZT in comparison to RF magnetron sputtering. Through TEM analyses, denser sol-gel films where found to have much better dielectric properties and ferroelectric properties.

Since the mid 1990s, sol-gel PZT has been proven to be a promising method for thin film and MEMS applications. Cooney (1996) provided one of the first PZT processing recipes. Cooney explained that beyond certain layer thicknesses, cracks could not be avoided. Cooney's processing recipe was applied to non-planar substrates to illustrate that the processing technique could be applied to MEMS.

Early in the sol-gel method development, Ballato (1995) provided motivation for potential applications of sol-gel PZT for thin film and high frequency membrane resonators. Ballato showed mathematically that if thin film piezoelectric layers can be accurately grown, resonant frequency devices could be extended into the GHz frequency range. However, this application is highly dependent upon the capability of controlling the layer's thickness accurately. More recently, Zhao (2003) provided empirical data illustrating the high-frequency properties and capabilities of PZT for RF-communications. They concluded that dielectric loss becomes significant in the transition regime from MHz to GHz. Moreover, using PZT in the GHz region would yield low quality resonators.

Many MEMS sensor and actuator applications have exploited the use of sol-gel derived PZT. Micro-mirrors, accelerometers, and vibration absorbers (Collet, 2004) are to name a few. Xu (1999) showed as an early MEMS sol-gel application that ZrO_2 is a reliable adhesion layer

for the PZT. Since SiO_2 is a common MEMS structural material Xu showed that using ZrO_2 as the buffer layer between the structural layer and piezoelectric layer provided both good adhesion and piezoelectric properties. In order to produce promising MEMS PZT actuators and sensors, cracks and hillocks (to be described layer) cannot exist.

The thermal effects from sol-gel processing steps were investigated by Dai (2004). A titanium adhesion layer was used, proving to be less reliant in comparison to ZrO_2. During the annealing process, the titanium began to diffuse into their platinum layer. The diffusion and thermal annealing led to large grains. Dai showed that the recrystallization of these grains was the main culprit for hillocks and cracks. Dai provided more understanding of hillock and crack creation and discussed two different methods for crack and hillock alleviation. To reduce these problems Dai recommended to either decrease the annealing temperature which subsequently hurts the piezoelectric properties or to increase the thickness of the titanium layer.

Chen (2003) researched methods of improving the processing of PZT deposited by sol-gel method. This publication provided a good processing recipe for crack alleviation and also explained how a critical thickness exists where thereafter cracking cannot be avoided. Cheng (2001) published a paper also relating to the thickness-dependent sol-gel PZT layer. However, Cheng discussed how the piezoelectric properties, namely the *d* constants, do not change after poling when the film thickness is $< 0.3\mu m$. Conversely, Cheng also discovered how the layer properties changed drastically when the layer's thickness was greater than $1.0\mu m$. Cheng and Chen both provide good reasoning for why PZT layers have to be a certain thickness for optimal properties.

In 2007 there was a plethora of sol-gel derived PZT research publications, including Faheem (2007), Ko (2007), Che (2007), Chou (2007), Wang (2007a), Wang (2007b), Ohya

(2007) and Lee (2007) to name a few. In this regard PZT MEMS devices are becoming more and more reliable thus motivating sol-gel fabrication processes. The future in PZT MEMS depends on easy fabrication methods with high quality and consistent reproducible material properties. New and exciting applications are being developed and will continue to be developed with the increase in sol-gel processing research.

2.3 ENERGY HARVESTING

In many places vibration energy is abundant. Motors, rotating objects, subways, pipelines, HVAC systems, bridges, and even the human body are to name a few. Piezoelectric material and more specifically PZT (in regard to the content of this thesis) can be used to scavenge or harvest mechanical vibration and produce electrical energy. Roundy (2005) present's basic equations for using piezoelectric and other types of mechanical to electrical coupling. A table is provided in Roundy (2005) that shows some peak acceleration values at specific frequencies in random vibrational settings. 60Hz to 400Hz was found to be the most common range of peak frequency values for machine tools, clothes dryer, door frame just as door closes, notebook computer, external window next to a busy street and many more. That paper also states that for any harvester, the power output depends on the system's coupling coefficient, the dynamic quality factor, density of the generator (proof mass/mass of harvester), and electrical load resistance. Roundy also explains that piezoelectric materials with large coupling coefficients are best for harvesting. Moreover, using PZT in energy harvesting devices could provide sustainable energy for electronic devices.

2.3.1 Quantifying Energy

In order for electronic devices to be continuously powered, energy harvesting structures have to produce an equivalent amount of power that the electronic device is dissipating. Otherwise, the harvesting devices will only increase the battery life and not make the sensor sustainable. In Sodano (2004a) a mathematical model is provided for a piezoelectric harvesting beam. Utilizing a clamped-free cantilever beam, like Figures 2.1 and 2.3, with dimensions that allow the structure to vibrate at its first mode that is common to the source's highest amplitude frequency, a cantilever was shown to be a good harvesting device (Wu, 2006). Sodano verifies this design with both a mathematical model and empirical results.

The most common method of storing the energy produced from a vibrating piezoelectric structure is by first rectifying the AC signal, then using an electrical storage device like a capacitor or battery to store the rectified signal. Guan (2006) investigated the best means of energy storage generated by a vibrating piezoelectric source. Guan compared a super-capacitor to a battery and regular capacitor. From this study, Guan concluded that the super-capacitor is the best means of storing energy. The parameters that determined this are charge/discharge efficiency, adaptability, lifetime, and self-discharge.

Providing electrical results for a piezoelectric structure and showing that it can store electrical energy, however, is not enough to prove that these devices can power an electrical circuit. By showing that a piezoelectric structure can power something useful like a signal transmitter will open up a window of applications for this type of device. Therefore, Sodano (2005a) investigated the necessary circuitry needed to power an AM transmitter. This publication showed how it is possible to charge a battery and power a transmitting device.

Sodano, Guan, and Roundy all provided reasoning that a piezoelectric structure can be a useful means of powering low energy consumption electronics. Since these publications are the preliminary work done in the energy harvesting area, the energy harvesting research and design still has much room for improvement.

2.3.2 d_{31} and d_{33} Modes

When utilizing PZT as means of harvesting energy, there are two common types of harvesting modes: d_{31} and d_{33}. Each design has an advantage over the other depending on the harvesting application. The following two figures depict common d_{33} and d_{31} harvesting designs.

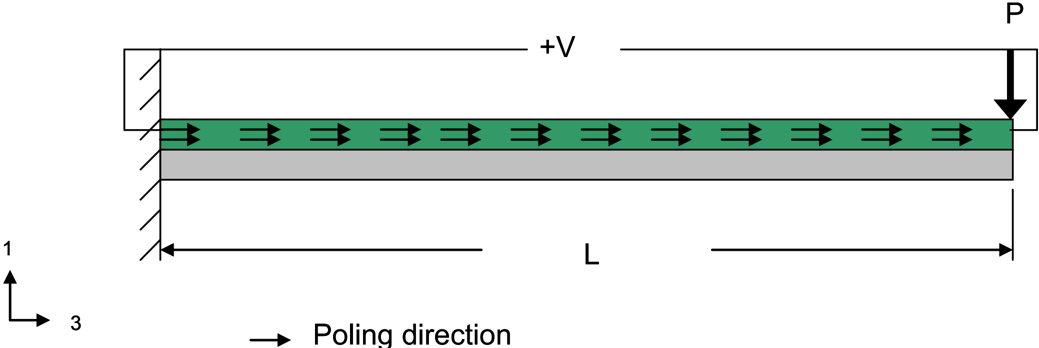

Figure 2.6. Typical d_{33} energy harvester

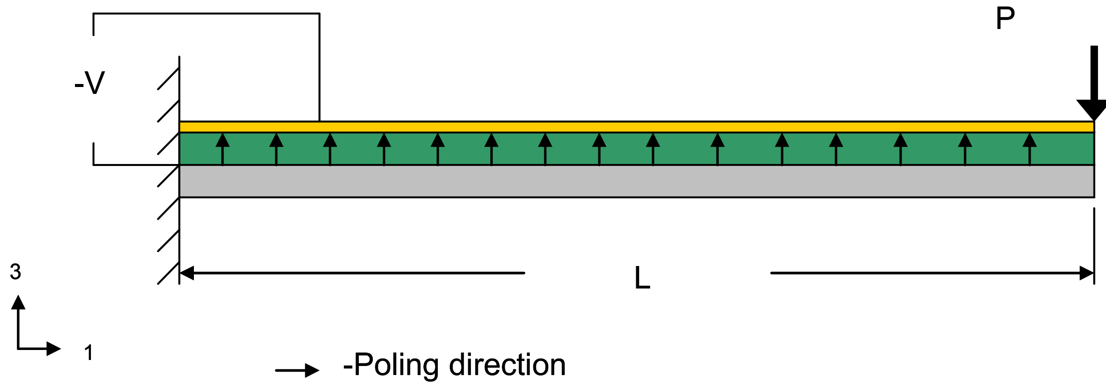

Figure 2.7. Typical d_{31} energy harvester

Sodano (2004b, 2005b) compared these two types of harvesting designs for power generation. More specifically Sodano compared a lab fabricated PZT beam, a commercial Quikpak® beam, a commercial IDE (interdigitated electrode) Quikpak® beam, and a MFC (microfiber composite) beam developed by NASA Langley Research Center. Sodano experimentally found that the d_{31} unimorph, Figure 2.7, performed the best in comparison to the IDE Quikpak® and MFC setups. These experimental results are also supported mathematically in Mo (2005). The underlining culprit for the poor harvesting characteristics of the d_{33} design is that area is sacrificed when using the interdigitated electrode (IDE) layout. This can simply be seen from the following energy equation (2.10)

$$E_c = \frac{1}{2}CV^2 \tag{2.10}$$

Equation (2.10) states that the energy of a capacitor is equivalent to half the capacitance multiplied by the corresponding voltage squared. The IDE layouts investigated significantly decrease the capacitance which limits the energy harvesting capabilities. However, a properly

designed d_{33} beam has the capability to produce the same energy as a d_{31} beam and possibly even more. This is because the d_{33} constant is significantly greater than the d_{31} constant.

Energy harvesting has a bright and energetic future. d_{31} and d_{33} designs are still being researched to produced more energy per volume. Other efforts, to be discussed in the next subsection, are reducing the size of the current harvesting structures to the MEMS scale. MEMS energy harvesting research has the capability to actually put the harvesting power source on the electronics that it will be driving. Energy harvesting is still in its infant stage of research. As seen in any field that is studied, the more researched an area becomes the more commercially available respective applications become. This is the direction for energy harvesting.

2.3.3 MEMS Energy Harvesting

The advent of sol-gel derived PZT and all of the research dedicated to it has spawned many applications in MEMS. Of those, MEMS piezoelectric harvester structures have been investigated, built, and tested by Jeon (2005), Choi (2006), Zhang (2003), Hong (2006), and Lee (2006).

In Jeon (2005) and Choi (2006), IDE d_{33} mode MEMS cantilevers where developed and test. Jeon utilized the d_{33} mode because the high output voltage of the device would be able to overcome the forward bias from the rectifying circuit. Their MEMS structure could produce about 1μW of power. Lee also created MEMS energy harvesting structures, however, no power data was provided.

Other efforts by Hong (2006) and John (2005) looked at using a PMN-PT as the piezoelectric material for the MEMS harvesting structure. PMN-PT is a relatively new

piezoelectric material. The advantage of this material is the four-fold enhancement in the piezoelectric coefficients. However, the two main disadvantages of this material are the price and the fact that PMN-PT is still in its infant stage of development. PMN-PT is a promising piezoelectric material and the future of MEMS energy harvesting may be centered around the use of this material.

Jeon (2005) was the first to develop MEMS scale energy harvesting structures. From the literature presented and extensive searching, no one else beside Jeon has presented empirical power data for MEMS scale structures. Therefore, much more research is needed to develop this area.

The direction for more recently developed electronics has been towards wireless capabilities. Wireless electronics implies the existence of an on board battery to power the device. As the market demands more wireless electronics, the drive for better sustainable sensors and electronics will increase. Efforts in energy harvesting on both the macro and MEMS scale is necessary to further exploit the capabilities of these harvesters. The future in wireless electronics is having the capacity for sustainable power that eliminates the need for manual charging. At this point in time, wireless electronics in environments that are not easily accessible is promoting research in energy harvesting areas. The cost of replacing a battery in these situations is very costly. Piezoelectric structures have been so far proved to be the best vibrational energy harvesting technique. Hopefully this technique in the end will allow for battery-less world.

2.4 TUNING

It was shown in Section 2.1 that a piezoelectric material can be modeled as a capacitor. Changing capacitance by adding a parallel or shunt capacitor will increase the systems overall capacitance. Increasing the piezoelectric equivalent capacitance will increase the compliance of the material and therefore decrease its stiffness. Clark (2000) showed that by varying the shunt capacitor connected to a piezoelectric material, the corresponding material stiffness will eventually (with increasing capacitance) decrease to the mechanical stiffness parameters. Moreover, Clark (2000) and Lesieutre (2004) presented a method of tuning vibrating piezoelectric structures by adding a parallel capacitor.

Tuning resonant frequencies is a highly important feature. Some applications include energy harvesting, electromechanical filters (Zhu, 2006), and resonators. Frederick (2005) applied the tuning technique to a cantilever beam. Frederick compared the d_{31} and d_{33} layouts. Analyzing the ratio of the open-circuit stiffness to the short circuit stiffness, Frederick reported that d_{33} design has a larger stiffness ratio. The larger stiffness ratio corresponds to a larger range of tuning which is of utmost importance when thinking purely about tuning.

With sol-gel PZT processing, thin film PZT can be produced. Devices like film bulk acoustic resonators (FBAR) and surface acoustic resonators (SAW) utilize thin films to produce high resonate frequencies. These devices operate in the ultra high frequency range (UHF). Being able to tune FBAR, SAW, and other high frequency resonators will help account for any manufacturing tolerances, device aging, and thermal effects which can change operating frequencies. In Frederick (2006) a comprehensive list of resonators and tuning techniques are

presented. Appling the capacitance tuning technique is presented as a definite competitor for tuning.

Advantages of the capacitive tuning technique include the nature of it being non-destructive, passive, and easy to adjust. One drawback of the passive shunt tuning technique is that structures can only be tuned one way. The open-circuit frequency of a piezoelectric resonator is the highest tangible frequency. Adding shunt capacitance will decrease the resonate frequency below the open-circuit frequency. Thus, if a frequency higher then the open circuit frequency is desired no passive measure can be taken to reach that frequency.

However, if a negative shunt capacitance could be added the corresponding resonant frequency should be increased. Date (1999) showed that by applying a negative capacitance to a piezoelectric structure the material's corresponding stiffness can be increased. Negative capacitance can increase the stiffness ratio by almost a two-fold range. Therefore, by applying both the passive shunt capacitance and the negative capacitance methods a broader tuning range can be developed. No piezoelectric tuning publications were found that covered both methods of tuning.

3.0 MATHEMATICAL PIEZOELECTRIC BEAM MODELS

Mathematical models are used to help predict the behavior seen by experiment. The linear constitutive piezoelectric equations (IEEE Std176-1997) are first examined. The constitutive equations illustrate the coupling between stress, strain, electric field and electric displacement. The piezoelectric constitutive equations are then applied to two beam models: d_{31} unimorph and d_{33} unimorph. The assumptions used to model the mechanics of the unimorphs are described. An exact analysis of a multilayer or composite piezoelectric beam is available in Shi (2006). Secondly, an energy model for each beam is given. The energy model considers the charge generated under an applied load and the capacitance of the structure. Both unimorph energy models are compared and discussed as possible design tools. Thirdly, two different dynamic mathematical models are derived for each unimorph. This is because of the different electrode layouts associated with the d_{31} and d_{33} unimorphs. Finally, mathematical inaccuracies are discussed for completeness. Each are analyzed and discussed based on the severity of the inaccuracy.

3.1 LINEAR PIEZOELECTRICITY

From the linear theory of piezoelectricity (IEEE Std 176-1997) the constitutive equations for the piezoelectric continuum are defined by equations (3.1) and (3.2)

$$S_{ij} = s^{E}_{ijkl} T_{kl} + d_{kij} E_k \tag{3.1}$$

$$D_i = d_{ikl} T_{kl} + \varepsilon^{T}_{ik} E_k \tag{3.2}$$

where S_{ij} = strain component, s^{E}_{ijkl} = elastic compliance constants at constant electric field, d_{kij} = piezoelectric constants, E_k = electric field component, D_i = electric displacement component, T_{kl} = stress component, and ε^{T}_{ik} = permittivity component at constant stress. Equations (3.1) and (3.2) can be reduced and expanded to (3.3-3.6) when utilizing engineering notation described in Table 1.

$$S_p = s^{E}_{pq} T_q + d_{kp} E_k \tag{3.3}$$

$$D_i = d_{iq} T_q + \varepsilon^{T}_{ik} E_k \tag{3.4}$$

$$T_p = c^{E}_{pq} S_q - e_{kp} E_k \tag{3.5}$$

$$D_i = e_{iq} S_q + \varepsilon^{S}_{ik} E_k \tag{3.6}$$

where e_{kij} = piezoelectric constants and

$$S_{ij} = S_p \quad when \quad i = j, p = 1,2,3$$

$$2S_{ij} = S_p \quad when \quad i \neq j, p = 4,5,6$$

remembering that for this notation (also described in Table 1) all *i, j, k, l* indices are summed from 1 to 3 and all *p, q* indices are summed from 1 to 6. The stored energy density of the piezoelectric continuum is defined by equation (3.7)

$$dU = \frac{1}{2} c_{ijkl}^{E} S_{ij} S_{kl} + \frac{1}{2} \varepsilon_{ij}^{S} E_i E_j \tag{3.7}$$

3.2 STATIC BENDING MODELS

When modeling a beam two models are typically considered, one of plane stress and one of plane strain. Using the piezoelectric axes notation, plane stress is defined as $T_2 = T_4 = T_6 = 0$. Plane strain is defined as $S_2 = S_4 = S_6 = 0$. Applying these conditions to equation (3.3-3.6), using the PZT d matrix equation (2.4), and neglecting the electric field in the E_2 direction yields

Table 2. Plane stress and plane strain simplified constitutive equations

Plane Stress	*Plane Strain*
$T_1 = c_{1j}^{E} S_j - e_{31} E_3$	$S_1 = s_{1j}^{E} T_j + d_{31} E_3$
$T_3 = c_{3j}^{E} S_j - e_{33} E_3$	$S_3 = s_{3j}^{E} T_j + d_{33} E_3$
$T_5 = c_{5j}^{E} S_j - e_{15} E_1$	$S_5 = s_{5j}^{E} T_j + d_{15} E_1$

Using a generalized plane stress/strain approach the clamped-free cantilever beam with an applied end load P can be modeled using the Airy Stress function (Slaughter, 2002)

$$\Phi = \frac{P}{6I_c} \left(X_a X_b^3 - \frac{3}{4} h^2 X_a X_b \right) \tag{3.8}$$

The remainder of the derivation is available in Slaugther (2002). The displacement equation thus becomes

$$u_a(X_a, X_b) = \frac{(1+\nu)}{E} \left(-\frac{P(1+\alpha)}{6I_c} X_b^3 + \frac{P\alpha}{2I_c} X_a^2 X_b + \left(\frac{Ph^2}{8I_c} - \alpha G \right) \right) \tag{3.9}$$

$$u_b(X_a,X_b)=\frac{(1+\nu)}{E}\left(-\frac{P\alpha}{6I_c}X_a^3-\frac{P(1-\alpha)}{2I_c}X_aX_b^2+\left(\frac{Ph^2}{8I_c}+\alpha G\right)+\alpha H\right) \tag{3.10}$$

where $u_a(X_a,X_b)$ is the deflection in the length direction and $u_b(X_a,X_b)$ is the deflection in the thickness direction. α is defined as

$$\alpha \equiv \begin{cases} 1-\nu & \text{for plane strain} \\ \dfrac{1}{1+\nu} & \text{for plane stress} \end{cases} \tag{3.11}$$

and ν = Poisson's ratio, E = Young's modulus, X_a is the length direction, X_b is the thickness direction, h is the thickness, and I_c = second moment of inertia. The subscripts "*a*" and "*b*" are used to generalize the length and thickness direction, respectively. This generalization is done because the axes are swapped for the d_{31} and d_{33} models. $X_a = 0$ is the free end, $X_b = 0$ is the center of the beam, and

$$G=\frac{PL^2}{2I_c} \tag{3.12}$$

$$H=-\frac{PL^3}{3I_c}-\frac{Ph^2L}{8\alpha I_3} \tag{3.13}$$

This model assumes the beam material is isotropic. The maximum deflection occurs at

$$u_b(0,0)=\frac{-PL^3}{3EI_c}-\frac{Ph^2L(1+\nu)}{8EI_c} \tag{3.14}$$

Simple beam theory predicts a maximum deflection of $PL^3/3EI_c$. As L becomes much greater than h equation (3.14) approaches the deflection value of simple beam theory.

Figure 3.1 is provided to illustrate the difference between plane strain and plane stress displacements. Figure 3.1 plots both the deflections for a plane strain and plane stress model under the same applied load *P* where the subscript *S* denotes the plane strain model and the subscript *T* denotes the plane stress model. The plane strain model is slightly stiffer than the plane stress model because of added Poisson's effects.

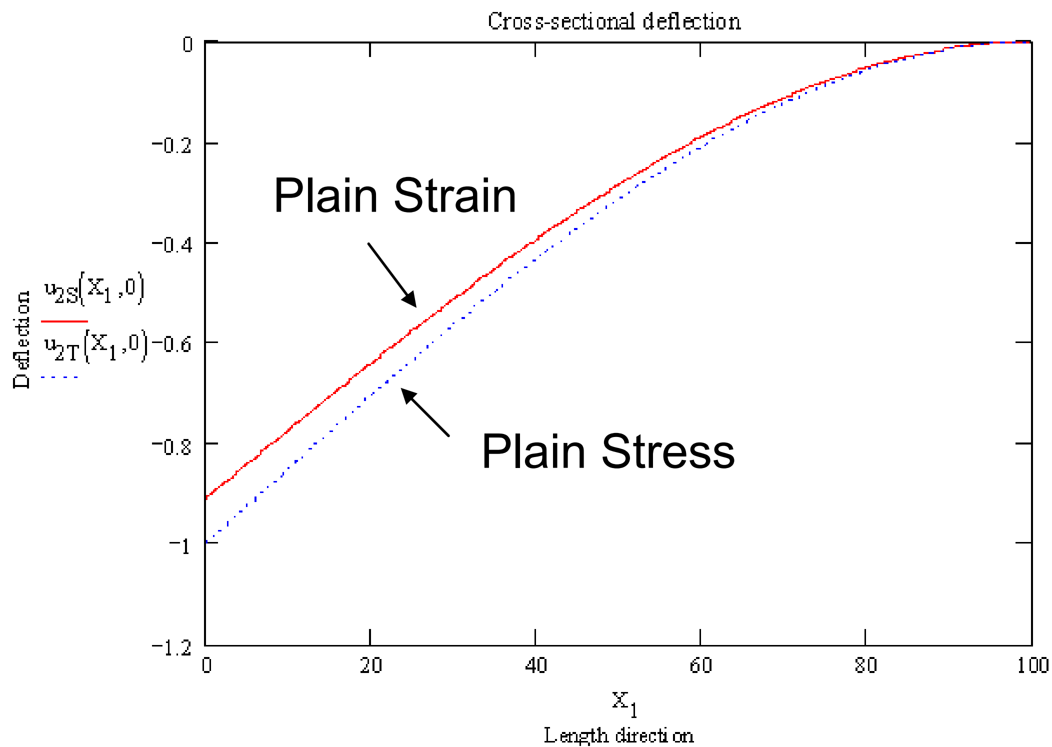

Figure 3.1. Beam deflection plot for both the plane strain and plane stress

If the beam has multiple layers with various elastic moduli, the modulus weighted method is used to normalize the layer's moduli. Figure 3.2 shows how a rectangular cross-section of a beam with different Young's moduli , *E*, can be converted into a beam with different layer widths corresponding to a ratio of the Young's moduli.

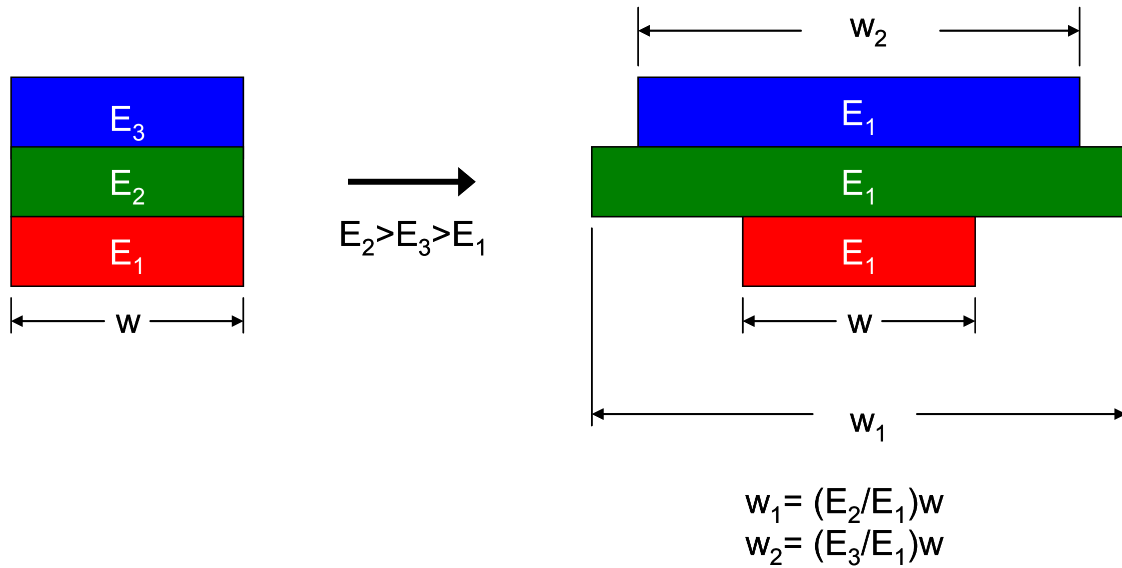

Figure 3.2. Weighted modulus method for composite beams

For example, if a beam has three layers with each layer having different moduli, one of the layers is picked to be the reference layer. The other layers widths change by multiplying the width by the ratio of the layer's modulus to the reference layer's modulus. The weighted modulus method changes the second moment of inertia effectively making the structure more or less stiff.

As mentioned, the plane strain model is slightly stiffer than the plane stress model because of the added Poisson's effect. This is shown empirically for MEMS beams in Hou (2003). Hou's research varied the width parameter of the MEMS beams and held all other variables constant. His work showed how a beam's stiffness changes as a function of width.

During the displacement derivation the stress components are defined and listed below

$$\sigma_{aa} = \frac{P}{I_c} X_a X_b \tag{3.15}$$

$$\sigma_{bb} = 0 \tag{3.16}$$

$$\sigma_{ab} = \frac{P}{2I_c}\left[\left(\frac{h}{2}\right)^2 - X_b^2\right] \tag{3.17}$$

If one considers the maximum stress for normal stress σ_{aa} and shear stress σ_{ab} the corresponding ratio is

$$\left(\frac{\sigma_{aa}}{\sigma_{ab}}\right)_{\max} = \frac{4L}{h} \tag{3.18}$$

The micro-scale beams designed are much much longer than the thickness. Therefore, the shear stress generated from an applied free end load is neglected leaving only the stress in the length direction. This is important to note because the equations are reduced to only having one piezoelectric constant, thus implying that the charge generated from the shear and the stress in the thickness direction has a negligible affect.

Now the equations in Table 2 reduce to Table 3.

Table 3. The equations for plane strain/stress for each beam design (Figures 2.6 and 2.7)

Plane Stress	*Plane Strain*	
$T_1 = c_{1j}^E S_j - e_{31} E_3$	$S_1 = s_{1j}^E T_j + d_{31} E_3$	d_{31} beam
$T_3 = c_{3j}^E S_j - e_{33} E_3$	$S_3 = s_{3j}^E T_j + d_{33} E_3$	d_{33} beam

3.2.1 Unimorph d_{31} Beam model

A uniform d_{31} beam is a cantilever beam composed of two main layers. These two main layers are the substrate layer and the piezoelectric layer. Figure 3.3 shows a typical d_{31} beam.

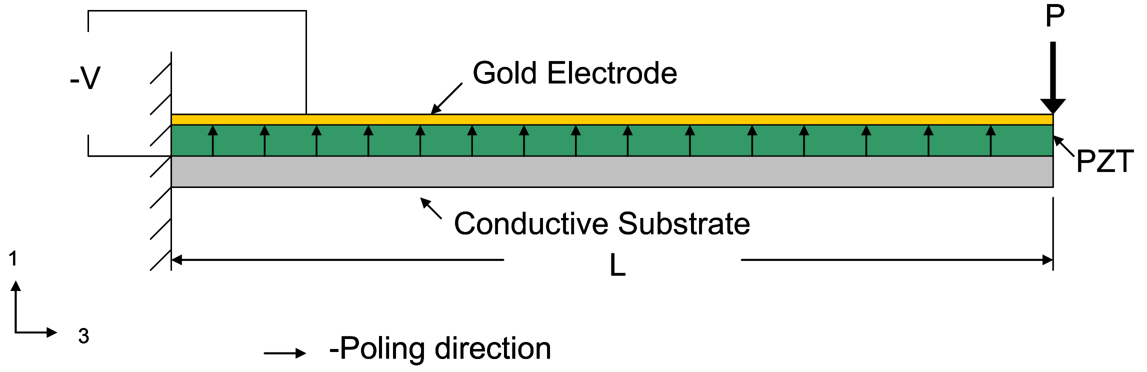

Figure 3.3. Unimorph d_{31} beam

The gold layer in Figure 3.3 is the electrode deposited on top of the piezoelectric layer. This layer is typically thin (~3000 Å) and is commonly neglected in mechanical models. The electrode layer is used to pole the piezoelectric material in the thickness direction. Additionally, the electrode layer is used for sensing or actuation of the structure or for charge collection in an energy harvester.

The energy of a unimorph d_{31} beam is derived from the combination of the piezoelectric and structural layers. The energy of the piezoelectric layer is given by equation (3.7). Substituting the plane stress relationship from Table 3 into equation (3.7) yields

$$dU_p = \frac{1}{2}\left(s_{11}^E T_1 - d_{31}E_3\right)T_1 + \frac{1}{2}\left(-d_{31}T_1 + \varepsilon_{33}^T\right)E_3 \qquad (3.19)$$

The energy in the substrate layer is

$$dU_m = \frac{1}{2}s_{11}T_1^2 \qquad (3.20)$$

The subscript $_p$ is be used to denote the piezoelectric layer and the subscript $_m$ is used to denote the substrate or metal layer. Additionally the superscripts ^{E} and ^{T} will only refer to the material

properties of the piezoelectric material. All non-superscript material properties are for the substrate layer.

In order to solve for the total energy in equations (3.19-3.20) the moment relationship (3.21) has to be imposed.

$$M = \int_{area} T_1 (z - z_c) dydz = \int_z T_1 (z - z_c) Wdz \tag{3.21}$$

Here $(z - z_c)$ is the distance away from the neutral axis z_c. Separating equation (3.21) into the piezoelectric and substrate part yields a moment equation for each layer.

$$M = \int_0^{h_p} T_1^E (z - z_c) Wdz + \int_{-h_m}^{0} T_1 (z - z_c) Wdz \tag{3.22}$$

Assuming that the strain in the 1-direction is equal to

$$S_1 = -\rho (z - z_c) \tag{3.23}$$

where ρ is the radius of curvature, and the neutral axis, z_c, is equal to

$$z_c = \frac{h_p^2 s_{11} - h_m^2 s_{11}^E}{2\left(h_m s_{11}^E - h_p s_{11}\right)} \tag{3.24}$$

the stress, T from Table 3, can be written in terms of equations (3.23-3.24).

$$\left.\begin{aligned} T_1^E &= \frac{1}{s_{11}^E}\left[-\rho(z - z_c) + d_{31}E_3\right] \\ T_1 &= \frac{1}{s_{11}}\left[-\rho(z - z_c)\right] \end{aligned}\right\} \text{for piezoelectric and substrate layer} \tag{3.25}$$

Substituting equations (3.25) into equations (3.19-3.20), the infinitesimal energy is

$$dU_p = \frac{1}{2} s_{11}^E \left(\frac{-\rho(z - z_c) + d_{31}E_3}{s_{11}^E} \right)^2 - d_{31}\left[\frac{1}{s_{11}^E}\left(-\rho(z - z_c) + d_{31}E_3\right)\right] E_3 + \frac{1}{2}\varepsilon_{33}^T E_3^2 \tag{3.26}$$

$$dU_m = \frac{1}{2} s_{11} \left[-\rho(z - z_c)\right]^2 \tag{3.27}$$

Equations (3.26-3.27) are integrated across the volume and Kim (2002) shows that the energy produced from a cantilever beam under a static end load is

$$U_{Gen} = \frac{1}{2}\frac{Q_{Gen}^2}{C_{oc}} \tag{3.28}$$

where Q_{Gen} and C_{oc} are

$$Q_{31Gen} = -\frac{3d_{31}s_{11}s_{11}^E h_m\left(h_m + h_p\right)L^2}{B_{11}}P \tag{3.29}$$

$$C_{31oc} = \frac{\varepsilon_{33}^T WL}{h_p}\left[1 + \left(\frac{3s_{11}^{E\,2} s_{11}h_p h_m^2\left(h_m + h_p\right)^2}{(s_{11}^E h_m + s_{11}h_p)B_{11}} - 1\right)K_{31}{}^2\right] \tag{3.30}$$

and $B_{11} = \left(s_{11}h_p^2\right)^2 + 4s_{11}^E s_{11}h_m h_p^3 + 6s_{11}^E s_{11}h_m^2 h_p^2 + 4s_{11}^E s_{11}h_m^3 h_p + \left(s_{11}^E h_m\right)^2$, $K_{31} = d_{31}\big/\sqrt{\varepsilon_{33}^T s_{11}^E}$. B_{11} is the outcome from doing the integration of (3.26-3.27) and K_{31} is the electro-mechanical coupling.

3.2.2 Interdigitated Unimorph d_{33} Beam Model

The interdigitated beam elicits the d_{33} piezoelectric constant. The d_{33} constant for PZT is commonly known to be twice as large as the d_{31} constant. Therefore, designing a d_{33} structure properly could produce more energy and larger tuning range than a d_{31} structure. Figure 3.4 depicts a common d_{33} beam design. The piezoelectric material is poled towards the anode and all the material underneath the electrode is assumed to be poled. Figure 3.5 illustrates this assumption.

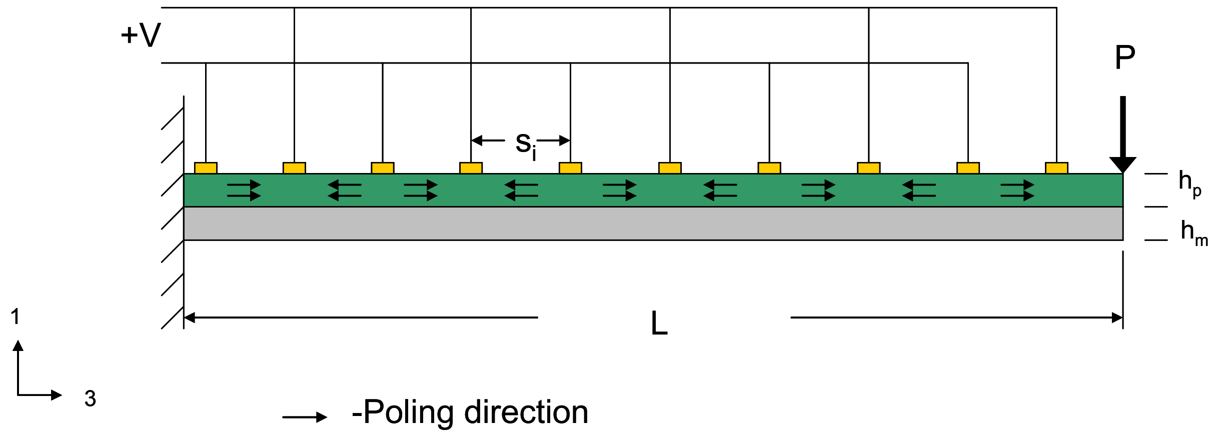

Figure 3.4. Typical interdigitated unimorph d_{33} beam

However, depending on the electrode spacing and the piezoelectric layer thickness this assumption might not be valid. The interdigitated electrode (IDE) non-uniform poling will be considered in Chapter 7.

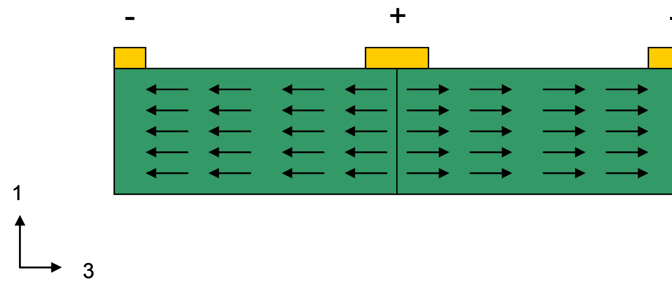

Figure 3.5. Magnified view of the piezoelectric layer of IDE d_{33} beam

The derivation of the energy equations for an IDE d_{33} beam is very similar to the d_{31} beam approach in Section 3.2.1. The step by step derivation is available in Mo (2005). The only difference in the derivations is when the energy is integrated across the volume of the structure. The d_{31} beam model is integrated uniformly across the length while the d_{33} beam is broken up into individual sections between each electrode.

$$U = \sum_{i=1}^{n} \int_{S_i} \int_{0}^{W} \left(\int_{0}^{h_p} dU_p dz + \int_{-h_m}^{0} dU_m dz \right) dydx \tag{3.31}$$

The parameter s_i in equation (3.31) refers to each individual section between the electrodes. For each segment spacing, s_i, if a percentage of the piezoelectric material is considered to be poled in the 3-direction then Q_{Gen} and C_{oc} are

$$Q_{33Gen} = -\frac{3(\%d_{33})s_{33}s_{33}^{E}h_m h_p\left(h_m + h_p\right)}{B_{33}} Pn\left(\sum_{i=1}^{n}(s_i)\right) \tag{3.32}$$

$$C_{33oc} = \left[1 + \left(\frac{3s_{33}^{E\,2}s_{33}h_p h_m^2\left(h_m + h_p\right)^2}{(s_{33}^{E}h_m + s_{33}h_p)B_{33}} - 1\right)(K_{33})^2\right]\sum_{i=1}^{n} C_i \tag{3.33}$$

where

$$C_i = \frac{\varepsilon_{33}^{T} W h_p}{s_i} \tag{3.34}$$

The percent poling factor, $\%d_{33}$, depends on the spacing and will be shown later in Chapter 7 that the percent factor approaches one as the spacing, s_i, increases. Therefore, different spacing values will correspond to different percent poling factors. Q_{gen} and C_{oc} are left in a summation form because the parameter s_i can be varied depending on the electrode spacing. $B_{33} = \left(s_{33}h_p^2\right)^2 + 4s_{33}^{E}s_{33}h_m h_p^3 + 6s_{33}^{E}s_{33}h_m^2 h_p^2 + 4s_{33}^{E}s_{33}h_m^3 h_p + \left(s_{33}^{E}h_m\right)^2$ and $K_{33} = \%d_{33} \big/ \sqrt{\varepsilon_{33}^{T}s_{33}^{E}}$.

3.2.3 Comparing Unimorphs

In order to compare the performance of the d_{31} and d_{33} unimorph, the parameters of the energy are investigated. From equation (3.28) both of the d_{31} and d_{33} unimorphs' energy is a function

of Q_{Gen} and C_{oc}. Taking the ratio of these parameters will create some insight on how each of these structures compare. Equation (3.35) is the ratio of the d_{33} unimorph's capacitance to the d_{31} unimorph's capacitance.

$$\frac{C_{33oc}}{C_{31oc}} = \left(\gamma_1\left(\frac{K_{33}}{K_{31}}\right)\right)\frac{\sum_{i=1}^{n}\frac{\varepsilon_{33}^{T}Wh_p}{s_i}}{\frac{\varepsilon_{33}^{T}WL}{h_p}} \tag{3.35}$$

γ_1 is related to the ratio of s_{33}^{E}/s_{11}^{E} and other structural parameters.

$$\frac{Q_{33gen}}{Q_{31gen}} = \frac{\gamma_2\left(\frac{\%d_{33}}{d_{31}}\right)n^2\sum_{i=1}^{n}(s_i)}{L^3} \tag{3.36}$$

where γ_2 is also related to the ratio of s_{33}^{E}/s_{11}^{E} and other structural parameters.

Analyzing equations (3.35-3.36) one can determine which design will be better for its application. For instance, depending on the application if the ratios are greater than one then the d_{33} unimorph should be considered. If the ratios are less than one a d_{31} unimorph should be considered. Moreover, lower C implies that the structure is well-suited for tuning and higher Q implies that the structure is good for energy harvesting. Since $d_{33} > d_{31}$ for PZT the ratios naturally seem to lean towards a d_{33} unimorph. One would think that the d_{33} unimorph is the best design. But because of the percent loss factor, the charge generated Q_{33gen}, is typically less than Q_{31gen} which implies that the d_{33} unimorph is not as well suited for energy harvesting applications.

3.3 DYNAMIC BENDING MODEL

Since the electric displacement and stress equations (3.5-3.6) are coupled, the stiffness of a unimorph is not just dependent on the elastic modulus and second moment of inertia. Therefore, a coupled elastic modulus expression needs to be used. By assuming a uniform electric field and charge in a piezoelectric element, the voltage and current of the actuator or sensor can be written in the Laplace domain as

$$V(s) = LE_3(s) \qquad I(s) = sA_c D_3(s) \tag{3.37}$$

If the piezoelectric element is modeled to match that of a simple spring-mass system the stress and strain can be written as follows

$$T(s) = \frac{F_a(s)}{A_C} \qquad S(s) = \frac{Y(s)}{L} \tag{3.38}$$

In Clark (2000) the above relationships (3.37-3.38) were used to show that the effective stiffness for a d_{33} mode structure can be modeled as

$$s^{SU} = s_{33}^{E} - \frac{d_{33}^{2} A_c}{L} Z^{EL} \tag{3.39}$$

Z^{EL} is the impedance that is seen at both electrodes. If the electrodes are shunted with a passive electrical component, Z^{EL} has a maximum and minimum depending on the shunt condition. At zero impedance or short circuit the effective compliance reduces to

$$Z^{EL} = 0 \rightarrow s^{SU} = s_{33}^{E} \tag{3.40}$$

Equation (3.39) makes the assumption that the entire structure is covered with an electrode thus allowing the entire piezoelectric layer to be short circuited. At maximum impedance (no shunt) or open circuit the impedance approaches the structures capacitance and the effective compliance goes to

$$Z^{EL} = C_{oc} \rightarrow s^{SU} = s_{33}^{E} - \frac{d_{33}^{2}}{\varepsilon_{33}^{T}} \tag{3.41}$$

Equation (3.41) is the minimum compliance the structure will have. However, in order for a bending beam to have the compliance of (3.41) the beam can not have an electrode layer. This is because equation (3.39) is derived based on the assumption that the piezoelectric layer has constant stress. This is not the case for a bending beam. The linearly decreasing stress of a bent cantilever beam will create a non-uniform charge distribution that will be averaged by an electrode layer. It will be shown later that via testing that a cantilever beam open circuit frequency can be adjusted if the electrode area of the structure decreases.

After identifying equation (3.39) the bending frequencies of a unimorph beam can now be defined from the commonly know exact solution of a cantilever beam (Inman, 2001) as

$$\omega = (\beta_n L)^2 \sqrt{\frac{EI}{\rho_m A L^4}} \tag{3.42}$$

A unimorph piezoelectric cantilever beam, however, has two layers. Therefore, equation (3.42) needs to be modified so that it can correctly model a two layer beam. In Muriuki (2004), equation (3.42) was adjusted to compensate for a two layer beam as follows

$$k = \beta^4 L\left(E_m I_m + E_p I_P\right) \tag{3.43}$$

$$m = L\left(\rho_m A_m + \rho_p A_p\right) \tag{3.44}$$

Then equations (3.43-3.44) can be substituted into the following equation to determine the unimorph's bending frequencies

$$\omega = \sqrt{\frac{k}{m}} \tag{3.45}$$

Equation (3.45) works well for a d_{31} unimorph beam but does not tend to capture the structural stiffness of a d_{33} unimorph beam. This is because the d_{33} beam piezoelectric layer in

not uniformly poled. Areas in the piezoelectric layer, mainly the portions underneath the electrodes, do not match the compliance of equation (3.39). Equation (43) considers piezoelectric material that is fully poled (i.e. the direction of the dipoles all point in the ± 3-direction). However, this is not true for the d_{33} beam (which will be shown by FEA). For this reason a different frequency equation is desired to better model the effects of non-uniform poling.

One way of modeling a beam with different stiffness parameters along the length is to use the Moment-Area Theorems (Popov, 1999). Figure 3.6 shows a d_{33} beam with light blue areas

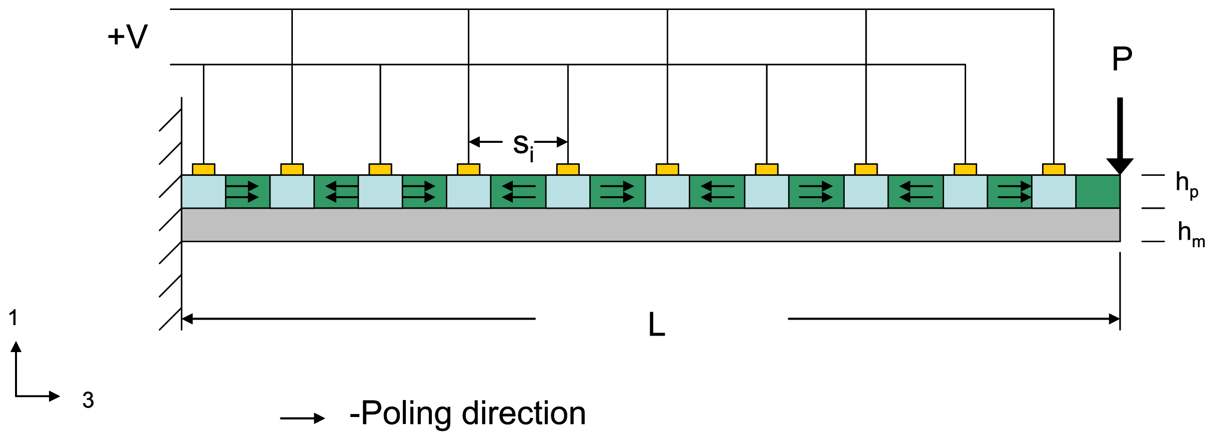

Figure 3.6. A d_{33} unimorph cantilever beam illustrating the areas underneath the electrode that have different stiffness properties

underneath each electrode. The light blue areas are shown to illustrate where the piezoelectric material has different stiffness properties. To help simplify the model, *m* non-uniform poling areas are assumed to exist for *m* electrodes. From the Moment-Area Theorems, the tip deflection δ_L for a cantilever is

$$\delta_L = \sum_{n=1}^{m+p} \Phi_n x_n \tag{3.46}$$

where x_n refers to the centroid of each Φ_n and

$$\Phi_n = \int_{s_{n-1}}^{L} \frac{M(n)}{EI(n)} dx - \Phi_{n-1}$$

(3.47)

$$\Phi_{n-1} = \int_{s_{n-1}}^{L} \frac{M(n)}{EI(n)} dx$$

and p is equal to the number of fully poled sections. x refers to the distance on the length of the beam. All negative and zero subscripts are zero for equation (3.47). Φ_n is the area under the curve that is created from the slope *M(n)/EI(n)*. The x-centroid of each first moment area is calculated using the following equation

$$x_n = \frac{\int_{s_{n-1}}^{L} x(x-L)dx}{\int_{s_{n-1}}^{L} (x-L)dx} \tag{3.48}$$

where x_n is the distance from the end L to the centroid of Φ_n. Then equations (3.47-3.48) are substituted into (3.46) to produce the corresponding tip deflection. Thus, the effective stiffness parameter is equal to

$$k_{eff} = \frac{P}{\delta_L} \tag{3.49}$$

It is important to note that E remains constant and $I(n)$ alternates between a fully poled value and non-uniform poled value. $I(n)$ is derived from the modulus-weighted method presented in Section 3.2 and in many static textbooks (Popov, 1999).

After solving for the effective stiffness, the effective mass needs to be calculated. From Rayleigh's Method for flexures, effective mass for a cantilever beam is calculated by the following equation

$$m_{eff} = \frac{m_L}{[y(L)]^2} \int_0^L [y(x)]^2 dx \qquad (3.50)$$

Equations (3.49-3.50) can now be substituted into equation (3.45) to get

$$\omega = \sqrt{\frac{P}{\frac{m_L}{[y(L)]^2} \int_0^L [y(x)]^2 dx}} \qquad (3.51)$$

Equations (3.43-3.44) and (3.51) are two models that successfully capture the dynamics for the d_{31} and d_{33} unimorphs, respectfully. Equations (3.43-3.44) were derived from exact beam solution (3.42) in order to predict the bending frequencies of a d_{31} unimorph. Equation (3.51) was developed in order to model the non-uniform poling areas from the d_{33} model.

3.4 MATHEMATICAL MODEL INACCURACIES

There are four mathematical inaccuracies that should be noted for some of the equations developed in Sections 3.2-3.4. First, each beam model neglects the clamped end effects that are commonly ignored because of Saint-Venants principle (Borrelli, 2006 and Ruan 2000). The second inaccuracy comes from the linear assumption for radius of curvature. MEMS devices are know to bend much more than large scale beams. The third inaccuracy is from the dynamic model neglecting viscous and structural (thermo-elastic) damping. MEMS devices are known to have large viscous damping effects from squeeze film and Couette damping (Nieva, 2006). The last mathematical inaccuracy is neglecting shear during beam bending. During shear the d_{15} piezoelectric constant is activated. Even though shear stress was presumed to be much less than

normal stress, the d_{15} constant is typically twice as large as d_{33} and therefore neglecting the electrical effects from shear is not a completely valid assumption (Parashar 2005).

3.4.1 Clamped End Effect

Since no simple mathematical models can predict the clamped end stresses a finite element analysis (FEA) model is shown to help illustrate the clamped end effect. Figure 3.7 shows a plate with a fixed or zero displacement on the left end and an end deflection on the right side.

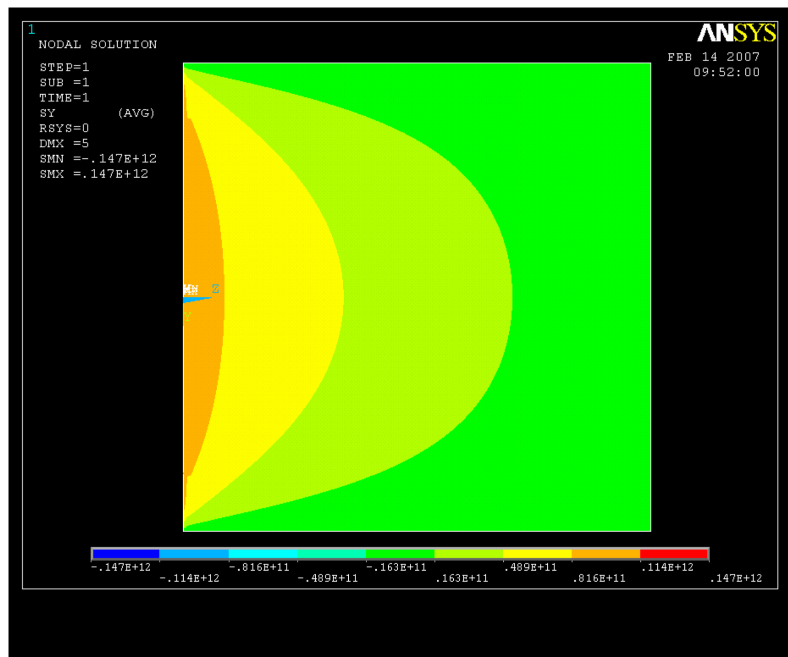

Figure 3.7. The y-stress of cantilever plate that is deflected into the page

Here one notices the stress in the y-direction resulting from the fixed displacement boundary condition. As Saint-Venant principles states the effects from the fixed end are negligible at distances greater than the width. Saint-Venant principle is shown to apply for Figure 3.7. If one considers a stress in the y-direction for a d_{31} or d_{33} unimorph, from the constitutive equations

(Table 2) there are two possible outcomes for the energy equations. One outcome is the adding of the charge produced from the introduction of another stress. The other is the cancellation of charge. From equation (2.4) the *d* matrix of PZT has 5 piezoelectric constants. d_{31}, d_{32}, and d_{33} all relate to the stress applied in the 1, 2, and 3 normal directions, respectively. The other constants, d_{15} and d_{24}, relate to shear stress applied in the 4 and 5 directions. The constants d_{31} and d_{32} have the opposite sign of d_{33}. For the d_{31} unimorph the 3-direction is in the thickness direction and the 1 and 2 correspond to the length and width directions, respectively. Thus, stress in the length direction and the stress in the width direction when multiplied by the *d* constants effectively add. The converse happens for the d_{33} unimorph because of the opposite sign of d_{32} and d_{33}. These two scenarios can either increase or decrease the electro-mechanical coupling.

3.4.2 Linear Bending Assumption

The second inaccuracy comes for the assumption that is commonly used to derive beam equations. This assumption is that the gradient of the displacement is much less than one. However, as previously noted MEMS beams can bend far greater than macro scale beams. The exact equation for the radius of curvature is shown below (Ginsberg, 2005).

$$\frac{1}{\rho} = \frac{\left|\dfrac{d^2y}{dx^2}\right|}{\left[1+\left(\dfrac{dy}{dx}\right)^2\right]^{\frac{3}{2}}} \tag{3.52}$$

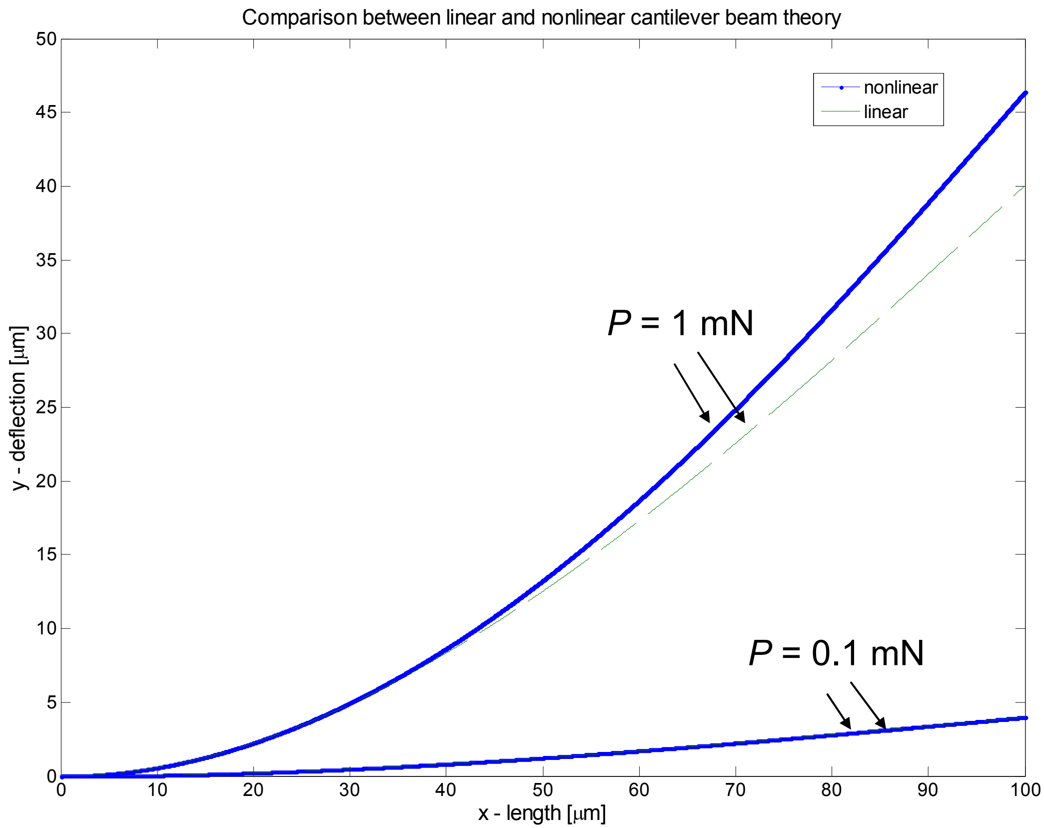

Figure 3.8. Plot represents the cantilever beam deflection for a linear and nonlinear model

A numerical model was developed that compared the nonlinear curvature, equation (3.52), to that of the static model equation (3.53), shown in Figure 3.8. The numerical model uses the 4th order Runge-Kutta method to solve equation (3.52). Equation (3.52) is compared to the static deflection model, equation (3.53-3.54), where

$$\frac{dy}{dx} << 1 \tag{3.53}$$

and $\frac{1}{\rho}$ becomes

$$\frac{1}{\rho} = \left| \frac{d^2 y}{dx^2} \right| \tag{3.54}$$

The material parameters and dimensions are defined in Table 4. The tip load was 0.1 mN for the lower deflection curves and 1mN for the upper deflection curves in Figure 3.8.

Table 4. Parameters used to equate the deflections shown in Figure 3.8

Beam	Length [μm]	Width [μm]	Heigth [μm]	Young's Modulus [MPa]
1	100	10	0.1	1.00E+07
2	100	10	0.1	1.00E+07

Figure 3.8 does show that miniscule inaccuracies do occur for the beam with the 0.1 mN load but are within limits of other assumptions. A 15% difference is shown for more of an extreme scenario that has a 1 mN load. Moreover, when a tip deflection of a cantilever beam becomes near the region of half the length the linear model becomes inaccurate.

3.4.3 Neglecting Damping

The dynamic models derived in Section 3.3 neglect the effects of structural and viscous damping. For a single degree of freedom system the dynamic response can be modeled as follows

$$\ddot{x} + 2\zeta\omega_n\dot{x} + \omega_n{}^2 x = f_o \cos\omega t \tag{3.55}$$

From equation (3.55) the damped natural frequency is derived to be

$$\omega_d = \omega_n\sqrt{1-\zeta^2} \tag{3.56}$$

ζ was assumed to be much less than one causing equation (3.56) to approach ω_n. However, as noted in Nieva (2006) for a MEMS device the smaller the distance from the ground plane to the

beam the larger the viscous damping. Therefore depending on the gap distance equation (3.56) can create a large inaccuracy when comparing the model to the experimental results.

3.4.4 Neglecting Shear Stress

The fourth inaccuracy of the mathematical models is neglecting shear. Shearing the d_{33} unimorph causes the d_{15} constant be activated. Because the d_{15} constant is typically two to three times as large as the d_{33}, shearing the piezoelectric layer makes the structure have a higher electro-mechanical coupling. Therefore, the shear stress produced during beam bending can effectively stiffening the beam. However, as mentioned before equation (3.18) shows that neglecting shear is an acceptable assumption for long thin beams. But because the d_{15} is two to three times as large as d_{33}, the shear stress becomes amplified making equation (3.18) a less valid assumption. Additionally, it is worth noting that for shorter and thicker beams neglecting shear becomes an invalid assumption.

4.0 MEMS BEAM DESIGN AND PROCESSING

In this section the MEMS die design and processing is reviewed and discussed. In MEMS a die is the portion of the wafer that holds the device. Many dice are packed onto a single wafer. Thus, for every batch many MEMS dice can be tested. The processing steps used are discussed and the parameters are provided. Post-processing measurements were taken to help characterize beam curl and undercutting. Measurements are provided for both the beam curl and undercutting and reasons are given for each phenomenon.

4.1 DIE DESIGN

As previously noted the work presented is a continuance of MEMS sol-gel derived PZT cantilever processing that Frederick (2006) did. The processing work picks up where Frederick left off. In Frederick's processing work, she created a die design that had various MEMS cantilever beams. Figure 4.1 is the die design. The die has cantilever beams with many different length and width dimensions and interdigitated electrode (IDE) patterns. Some beams are rectangular and others are trapezoidal shaped. All the beams are designed to be cantilever like meaning each has a clamped and free end. The different IDE patterns consist of beams with single, double and triple sets of IDEs on a single beam. A single IDE pattern has the capability

of sensing or actuating. The double IDE pattern has the ability to do two of the three following: sense, actuate, and or tune. And the triple IDE pattern has the ability to sense, actuate, and tune.

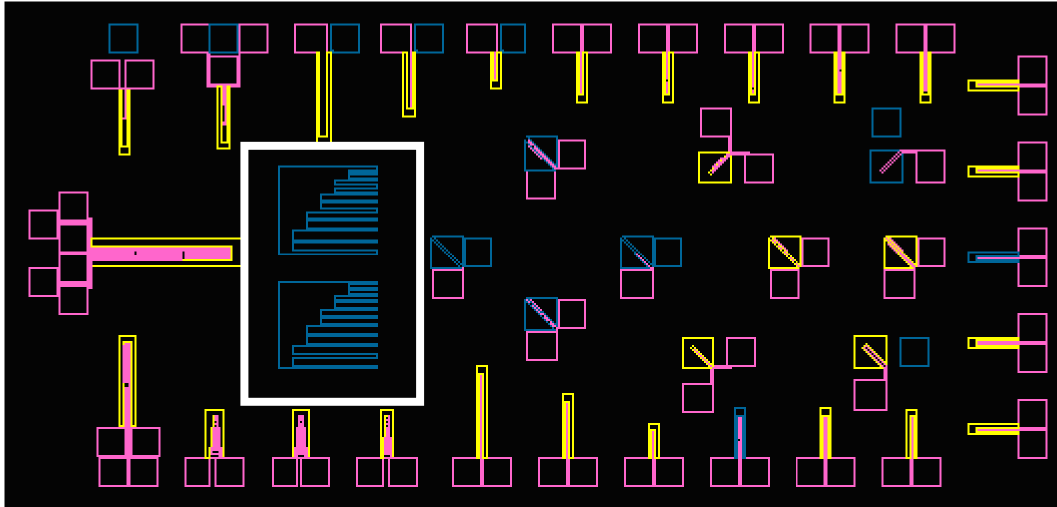

Figure 4.1. The die design for the mask layout

The blue area circled by a white perimeter box in the above Figure 4.1 is a compilation of various beams without electrodes that are used to gauge the amount of residual stress that might exist after releasing the beams. The die shown in Figure 4.1 was patterned onto a multilayer wafer. There are over a hundred die on the wafer that was tested.

4.2 PROCESSING STEPS

Three processing plans were developed in Frederick (2006). The beams tested in the current work were developed in Frederick's thesis and follow "Process Plan 2". "Process Plan 2" consists of the following steps shown Figure 4.2.

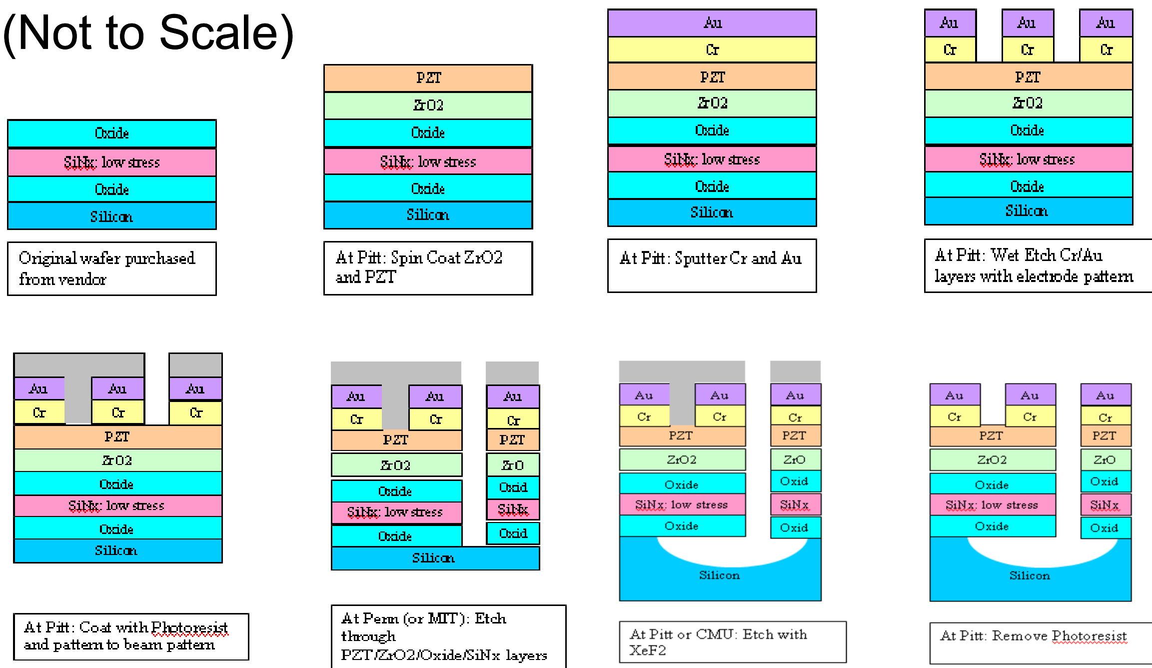

Figure 4.2. "Process Plan 2: RIE BCl_3:Cl_2 Step after Electrode Patterning" (Frederick, 2006)

The processing was continued at the XeF_2 dry etching stage. After the XeF_2 dry etching the final processing stage is the removal of the AZ410 photoresist. The AZ410 photoresist was used as a protective mask during the RIE etching at MIT. Table 5 lists the various thicknesses for each layer of the wafer.

Table 5. Different layer thicknesses

Layer	Thickness [μm]
Oxide1	0.10
SiNx	0.40
Oxide2	0.10
ZrO2	0.05
PZT	0.48
Cr	0.21
Au	0.21

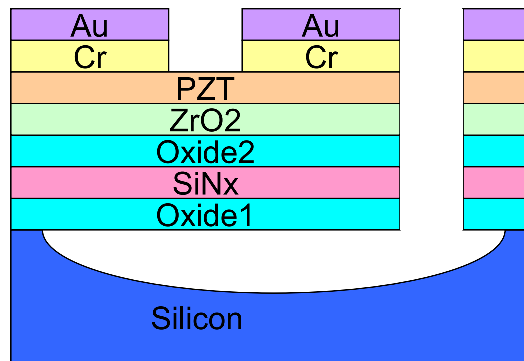

4.3 XEON DIFLUORIDE ETCHING

Xeon difluoride (XeF_2) dry etching was initially done in the MEMS lab at Carnegie Mellon University (CMU). The etching tool used was the Xactix® Xetch Xenon Difluoride Etching System X1 series. XeF_2 is known to be highly selective towards etching silicon in comparison to photoresist, silicon dioxide, aluminum, chromium, and titanium nitride. Therefore, the selectivity of XeF_2 made it highly desirable for structural release. Another beneficial feature of XeF_2 dry etching is that the etching is considered isotropic. Isotropic etching means that the etching substance does not prefer any plane orientation of the material being etched.

No etch rates were documented for CMU's Xactix® tool. However some common knowledge is available about the dry etching tool. High XeF_2 pressure (maximum 3 torr) results in faster etching rates and adding N_2 slows down the etch rate. In order to formulate an etching recipe, both the horizontal and vertical etch rates are desired. Consequently, the first stages of dry etching used a quarter of the MEMS PZT cantilever wafer in order to characterize the vertical and horizontal etch rates. Table 6 lists the processing parameters used for the dry etching.

Table 6. CMU's XeF_2 dry etching parameters

Sample	# of cycles	etch time/cycle	XeF2 pressure	N2 Pressure
1/4 wafer	27	60 sec	3 torr	0 torr

XeF_2 etch rates will vary depending on etching channel's width and the position on the wafer. An etching channel's width is the gap produced during the reactive ion etching processing step. These gaps are the pits that allow the XeF_2 gas to reach the silicon material. These gaps

can also be view as channels or ducting that permits the XeF_2 to attack the silicon. Because of the XeF_2 selectivity the beams are released by XeF_2 etching the silicon underneath them.

Three etch trials were completed using the parameters listed in the above table. At this point in order to characterize the etch rates a piece of the ¼ wafer was broken off using a diamond pen for scanning electron microscopy (SEM) examination. Figures 4.3 and 4.4 are SEM cross-sectional pictures of the sample piece cut from the ¼ wafer. From the SEM pictures and measurements made using the SEM software, the conclusion was made that for large open etching channels (>50 µm) the horizontal/vertical etch rates are 0.52 µm/min and 0.65 µm/min, respectively. For a smaller etching channel of around 10-20 microns, the calculated horizontal/vertical etch rates are 0.45 µm/min and 0.57 µm/min, respectively.

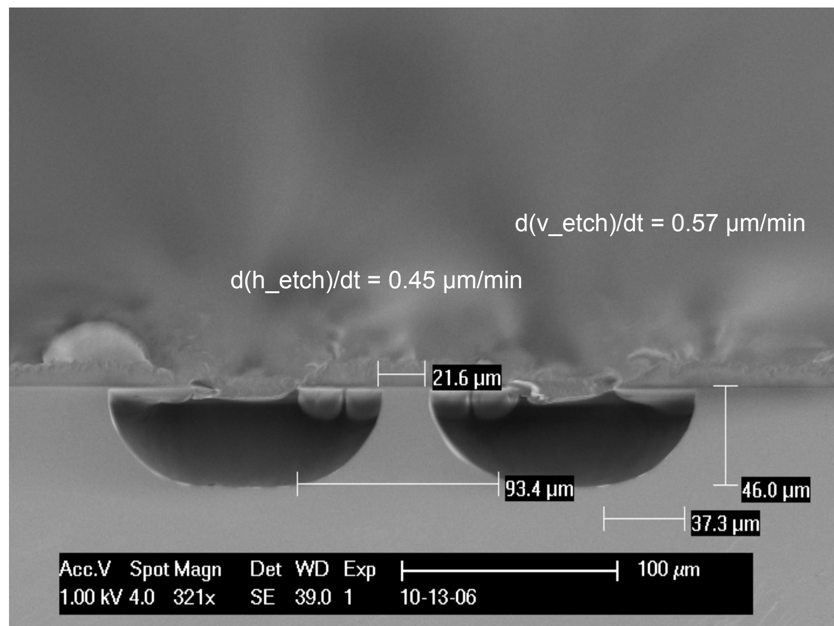

Figure 4.3. Horizontal and vertical etch rates for a 20µm opening using the process parameters in Table 6

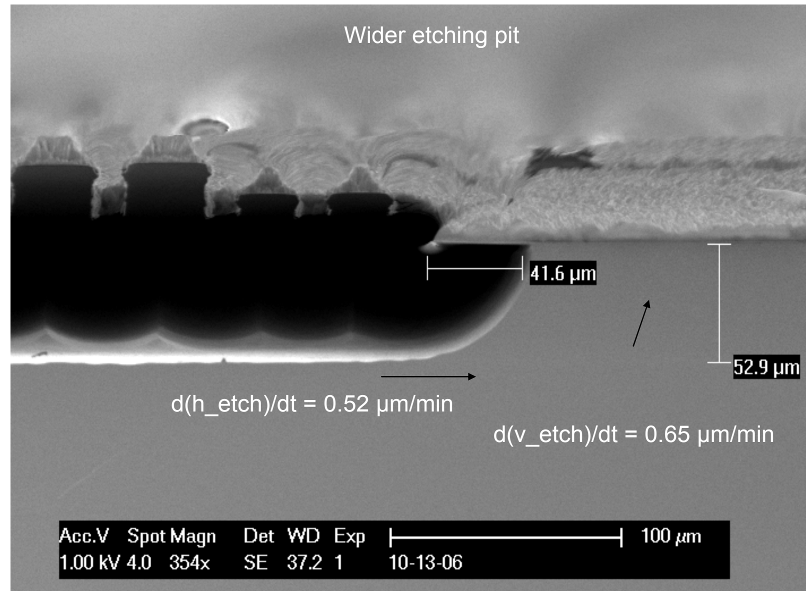

Figure 4.4. Horizontal and vertical etch rates for a larger opening using the process parameters in Table 6

After the etch rates were determined for Carnegie Mellon Univeristy's Xactix® XeF_2 tool, the tool's vacuum pump broke making the system inoperable. This dilemma created motivation for the installation of the University of Pittsburgh's recently ordered XeF_2 system. The etching tool used was the Xactix® X2 series XeF_2 dry etching tool. Unlike CMU's Xactix® tool, Pitt's X2 series tool has a dual pressure chamber that allows for an almost timeless transition between etching cycles. The dual pressure chamber reduces the total time it takes to etch a sample. Table 7 provides the processing parameters for using Pitt's tool.

Table 7. Pitt's XeF_2 dry etching parameters

Sample	# of cycles	etch time/cycle	XeF2 pressure	N2 Pressure
1/4 wafer	30	60 sec	2 torr	4 torr

Comparing Tables 6 and 7 one may notice the difference in parameters. The XeF_2 pressure was decreased and the N_2 pressure was increased. These changes reduced the etch

rates. Slowing down the etch rate will cause the vertical and horizontal etch rates to approach one another making the etch more isotropic. Additionally, slower etch rates will reduce the etching temperature. Using the parameters in Table 7, the XeF_2 etch became very isotropic and had an etch rate of 0.28 μm/min for both small and large channels. Because Pitt's XeF_2 Xactix etcher was dual stage, the etching time requirements were dramatically reduced. Therefore, the shorter overall etching time period allowed for the beams to be etched at a slower rate making the etch very isotropic.

4.4 PHOTORESIST REMOVAL

After the XeF_2 dry etching was complete the AZ410 photoresist was removed. This was done by submerging the wafer piece in a beaker full of an acetone solution. The solution was agitated until the majority of the visible photoresist was removed. The sample was then moved into a new acetone bath. Further, agitation was conducted for about five minutes. Viewing the surface under the microscope finally insured that the photoresist removal process worked sufficiently. Figure 4.5 shows the released beams with the photoresist removed. As one can notice from Figure 4.5 upon removal of the photoresist, the beams curled to a large degree. This will be discussed in the subsequent section.

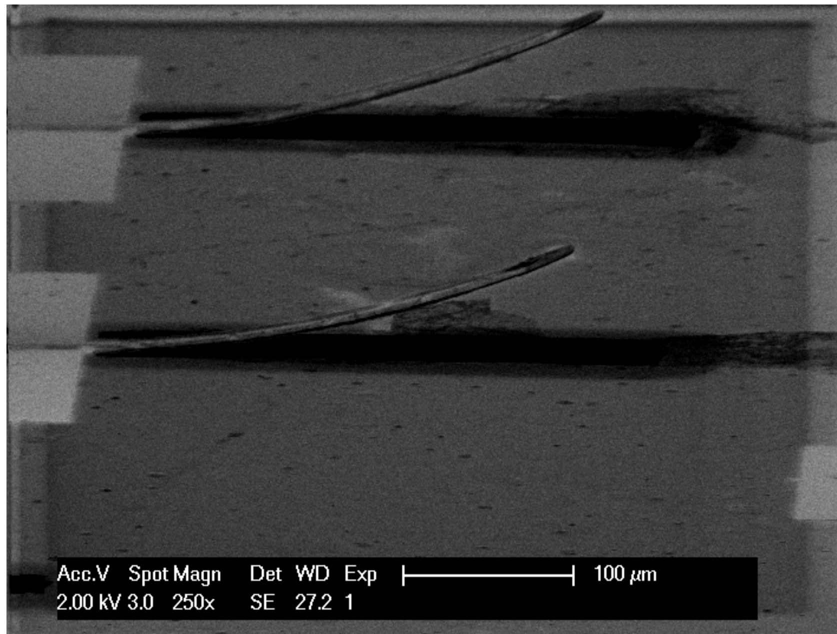

Figure 4.5. SEM photograph of the released beams

4.5 CURLING OF BEAMS

After the structural release and the removal of photoresist, it was obvious that the beams curled. The reason is because vertical stress gradients existed in the multilayered beams. During the processing of this wafer, Frederick did not provide layer by layer laser interferometric profilometer measurements. Laser interferometric profilometer measurements provide data that can be used to measure wafer curvature and the corresponding residual stresss of each layer. The residual stress values had to be pursued in a different manner. The calculation of residual stress created by each layer is limited to a lumped mathematical model with many assumptions. Table 8 lists the residual stress measurements done in Jeon (2005). The residual stress measurements done in Jeon are given as a range of values (i.e. 630/610 [MPa]). This table is provided as a

basis for comparison. The processing steps in Jeon are highly comparable to the processing steps in Frederick (2006).

Table 8. Mechanical properties and residual stresses of films deposited in Jeon (2005)

Parameters	PZT1	PZT2	PZT3	PZT4	ZrO2	SiO2 (thermal)	SiO2 (PECVD)	SiNx
Elastic Modulus [GPa]	63	63	63	63	244	69	69	313
Poisson Ratio	0.30	0.30	0.30	0.30	0.27	0.15	0.15	0.29
Residual Stress [Mpa]	630/610	-115/-125	75/65	113/105	400/350	-280/-330	35/-15	210/170

However, the single difference between the cross-sections of Frederick and Jeon's work is that in Frederick (2006) an extra layer of SiO_2 was below the SiN_x. This was because the wrong wafers were order. Therefore, in order to ensure proper adhesion with ZrO_2 Frederick sent the wafer's to get the extra layer of SiO_2. With further investigation it was found that both of the SiO_2 layers were deposited by LPCVD (aka thermal). Relating this discovery to Table 8 implies that there is a large amount of compressive residual stress in the beams before release.

In order to predict where the neutral axis is the follow equation (4.1) was used and derived from the modulus-weighted method (Popov, 1999).

$$Z = \frac{2h_1^2 + n_1 h_2\left(h_1 + \frac{h_2}{2}\right) + h_1 h_2 + n_2 h_3\left(2h_1 + h_2 + \frac{h_3}{2}\right) + n_3 h_4\left(2h_1 + h_2 + h_3 + \frac{h_4}{2}\right)}{2h_1 + h_2 + h_3 + h_4} \tag{4.1}$$

Equation (4.1) considers the five layer MEMS beam consisting of $SiO_2/SiN_x/SiO_2$/PZT/Au. n_1, n_2, and n_3 are ratios of the following young's moduli: SiN_x/SiO_2, PZT/ SiO_2, and Au/SiO_2, respectively. Section 3.2 provides more information about the derivation of equation (4.1). Equation (4.1) revealed that the neutral axis is about 0.78 microns from the bottom. This implies that both of the SiO_2 layers are below the neutral axis. Therefore, since LPCVD of SiO_2 produces a compressive residual stress and both the SiO_2 layers are below the neutral axis the

excessive beam curl after release is easier to understand. Moreover, the expansion of the bottom layer to release the residual stress causes the beams to curl up after release.

In order to calculate the total amount of residual stress in the beam, measurements were taken using a microscope with an x-y-z stage. The microscope was used to determine the height of the deflection for the beams being tested. The microscope was used as follows:

1) At the beginning of each measurement, the microscope was focused at the base of the beam

2) The z-stage displacement reading was zeroed out

3) The stage was slowly zoomed out (zooming out will cause the focus to travel up the beam and away from the base)

4) When the microscope was focused at the tip of the beam the z-displacment was recorded

Various beams were measured to determine the radii of curvature. Additionally, non-IDE patterned beams were measured to help predict if any extra residual stress might have been developed in the Au/Cr layers. The assumption was made that the beam curvature matched that of a circle. From geometry and knowing both the out-of-plane tip displacement and beam length the following formula was derived (4.2)

$$\delta_o = 2r\,sin^2\left(\frac{L_o}{r}\right) \tag{4.2}$$

where δ_o is the planar tip displacement, *r* is the radius of the circle, and L_o is beam length before the beam was released. L_o was assumed to remain constant. Equation (4.2) was numerically solved for *r*.

Using the radius predicted by equation (4.2), equation (4.3) was used to calculate the effective internal stress gradient, σ_1 of a beam after release but before bending (Senturia, 2001).

Figure 4.6 provides a plot of the effective internal stress gradient, σ_1, of the beam after release but before bending.

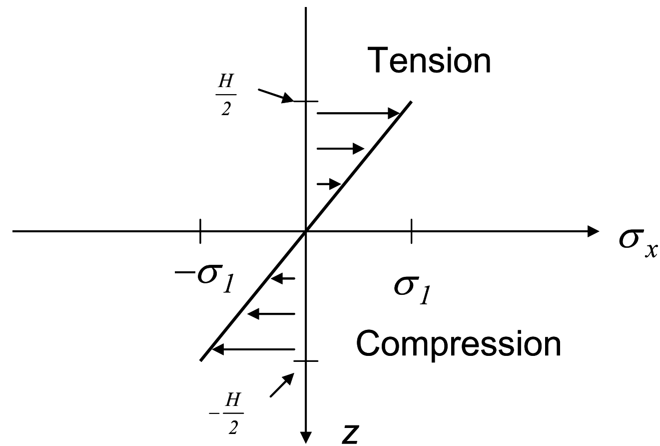

Figure 4.6. Plot of the internal stress gradient of a beam after release but before bending

Plate bending is taken into account in Equation (4.3) because the film stress gradient is also in the width direction.

$$r = \frac{Eh}{2(1-\nu)\sigma_1} \tag{4.3}$$

Table 9 provides the results from the microscope measurements. Equations (4.2-4.3) are used to calculate the radius of curvature and stress gradient in Table 9.

Table 9. Residual stress values for various beams across the wafer

	Beam #	L_o [µm]	δ_o [µm]	$\frac{1}{r}$ $[\mu m]^{-1}$	σ_1 , %E [MPa]	Deflection Predicted by Stoney's Formula [µm]
Gold Layer	1	200	40.8	1952	0.051	21.9
	2	200	41.7	1910	0.052	22.5
	3	300	57.3	3128	0.032	30.9
	4	300	58.0	3100	0.032	31.1
	5	300	59.0	3044	0.033	31.6
	6	300	59.8	3002	0.033	32.1
	7	300	59.8	3002	0.033	32.1
	8	300	62.1	2890	0.035	33.4
	9	300	67.3	2666	0.038	36.2
	10	300	74.1	2414	0.041	39.9
No Gold Layer	11	200	40.1	1987	0.050	21.6
	12	200	57.4	1384	0.072	30.9
	13	300	108.6	1639	0.061	58.8
	14	300	99.3	1795	0.056	53.7
	15	400	168.9	1867	0.054	91.9
	16	400	151.8	2083	0.048	82.3
	17	500	193.2	2554	0.039	104.7
	18	500	225.2	2182	0.046	122.7
	19	600	302.5	2329	0.043	165.5
	20	600	300.1	2347	0.043	164.3

E, h and ν are the material's modulus, height of the beam, and Poisson ratio respectively. The stress gradient in the MEMS beams is 0.045 $\%E$ ±0.004 $\%E$ and was determined at 90% certainty. Since the total effective modulus was unknown, the stress gradient was left in terms of a constant Young's Modulus, E. The stress gradient is approximated to be about 10-90 Mpa. The gold layer actually reduced the radius of curvature implying that the gold film had no compressive residual stress because the deflection would have increased. In order to help verify the result listed in Table 9, *Stoney's formula* (Stoney, 1909) was used to check the results. Equation (4.4) is *Stoney's formula*

$$\delta_o = \frac{3\sigma(1-\nu)}{E}\left(\frac{L}{h}\right)^2 \tag{4.4}$$

where σ is the applied stress. *Stoney's formula* predicted about half the measured deflection and is provided just to show that the measured tip deflections are within reasonable values. The online source, http://www.physics.mcgill.ca/SPM/sensor/stress.htm, states that Stoney's equation can be 100% inaccurate and is only applicable to scenarios where the beam has a top or bottom thin film with residual stress. Hence, the method provided here is a better way of finding the stress gradient in comparison to *Stoney's formula*.

4.6 XEON DIFLUORIDE UNDERCUT

The Xactix® XeF_2 recipe used at Pitt (Table 7) provided a slower more isotropic etch. Because the etching is isotropic the beams are undercut. The shaded area in Figures 4.7 and 4.8 depict the substrate undercut resulting from the XeF_2 etching. The undercut for Figure 4.7 was measured to be about 50 µm. The undercut for Figure 4.8 was less because the XeF_2 had smaller area for the gas to penetrate through. Figure 4.8's undercut was measure to be about 40 µm.

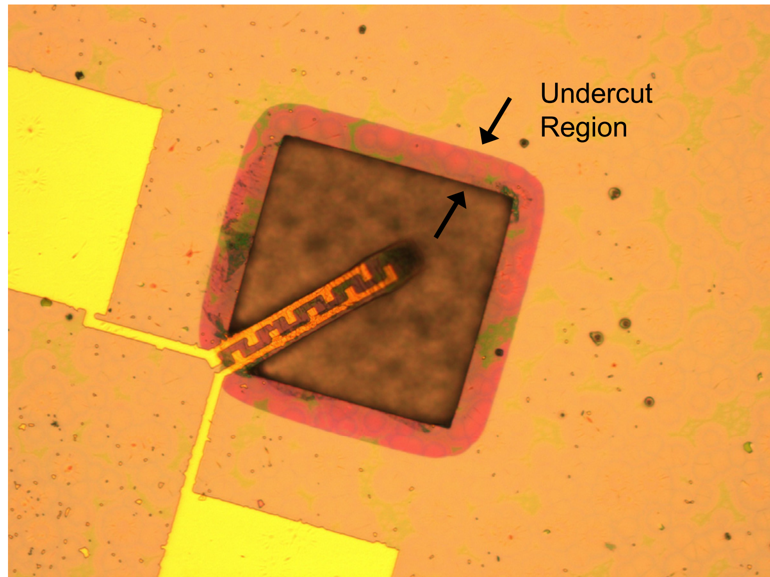

Figure 4.7. Diagonal beam, (110) direction, with a large etching channel illustrating the undercut resulting from the XeF_2 etching

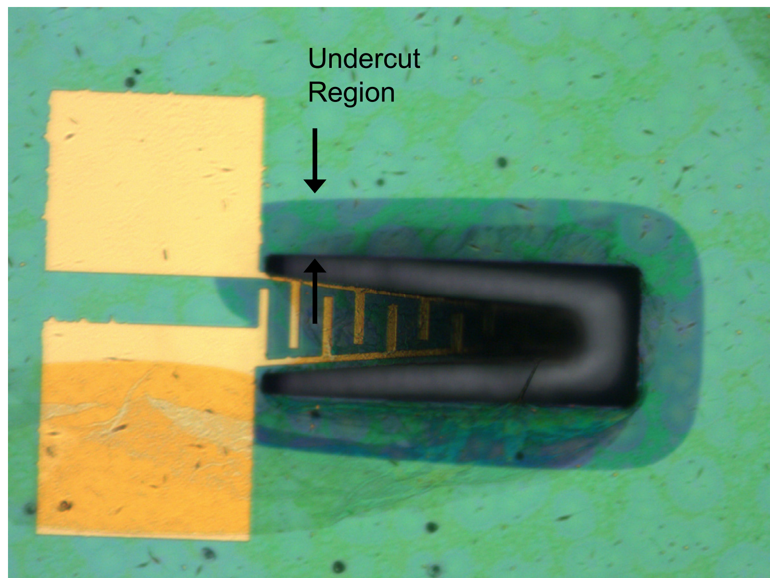

Figure 4.8. Transverse beam, (100) direction, with a small etching channel illustrating the undercut resulting from the XeF_2 etching

Undercutting the cantilever will affect the natural frequencies of the beam. This is because the clamped end boundary conditions (zero deflection and zero deflection gradient) are no longer valid. The clamped end turns into a compliant end where there is deflection and bending. The natural frequencies will therefore decrease because the base is now compliant.

5.0 MODAL FININTE ELEMENT ANALYSIS

Finite element analysis (FEA) has become a popular and powerful tool for modeling the multi-physics of structures. In Lowrie (1999) FEA was shown to flawlessly model piezoelectric d_{31} and d_{33} unimorph sensors and actuators. Lowrie provided proof through experimental verification that FEA can be used as a tool to model the behavior of piezoelectric structures. In the present work an FEA model is developed to help predict the dynamical behavior of a d_{33} unimorph sensor. The Coupled-Field Analysis Guide from ANSYS™'s help menu was used as reference. Two separate FEA models were developed in order to help predict the natural frequencies for a rectangular and trapezoidal beam. Figures 4.7 and 4.8 where modeled using ANSYS™ 10.0 finite element analysis software (FEA). Figure 4.7 will be referred to as the diagonal beam and Figure 4.8 will be referred to as the trapezoidal beam from here on after. The FEA model used μMKS units as material properties to model the dynamics. Each beam model had two dynamic cases: open circuit and short circuit. The beam curl and undercutting were also modeled. This helped determine the consequences associated with the undercutting and curl.

5.1 FEA BEAM MODEL

The three layered d_{33} interdigitated electrode diagonal and trapezoidal beams were modeled using ANSYS™ 10.0. The three layers consist of a substrate, piezoelectric (active), and electrode layer. In order to model the behavior associated with the piezoelectric layer a coupled field analysis was undertaken. Solid 95 elements were used to model the substrate and electrode and Solid 226 coupled field elements were used to model the piezoelectricity. Table 10 lists the material properties in μMKS used for both FEA models. μMKS are recommended by ANSYS™ (ANSYS™ 10.0, Coupled-Field Analysis Guide) to be used for micro-scale devices. This allows for the dimension of the model to be in microns. The PZT layer was considered to be isotropic but was put into ANSYS as a 6x6 isotropic compliance matrix.

Table 10. Material property values used in FEA model in μMKS units

Substrate		PZT		Electrode	
Density	ρ = 2.20E-15	Density	ρ = 7.60E-15	Density	ρ = 1.928E-14
Young's Modulus	E = 7.50E+04	Young's Modulus	E = 3.00E+04	Young's Modulus	E = 8.00E+04
Poisson's ratio	v = 0.17	Poisson's ratio	v = 0.30	Poisson's ratio	v = 0.30
		Permittivity	ε_x = 900		
			ε_y = 900		
			ε_z = 1100		
		d constant	d_{31} = -1.9E-4		
			d_{32} = -1.9E-4		
			d_{33} = 3.9E-4		
			d_{24} = 5.0E-4		
			d_{15} = 5.0E-4		

Since the material properties were never tested, the values listed in Table 10 are from www.memsnet.org. This website has a comprehensive list of material properties with different processing techniques. Piezoelectric constants are provided for sol-gel PZT deposition methods that were used in the simulation. After the solid model was developed a modal analysis was

conducted using the Block Lanczos solver in order to produce the natural frequencies and mode shapes of the structure.

5.1.1 Diagonal Beam

The 30µm x 200µm diagonal beam was modeled in ANSYS and is shown in Figure 5.1. The left end has zero displacement boundary conditions at its cross-section. The sections between each electrode from the left end to the right end in Figure 5.1 have alternating piezoelectric *d* constants. The *d* constants alternate in a manner of being positive then negative. The alternating *d* constants surface when the interdigitated beams are poled. The IDE geometry causes the poling direction to alternate.

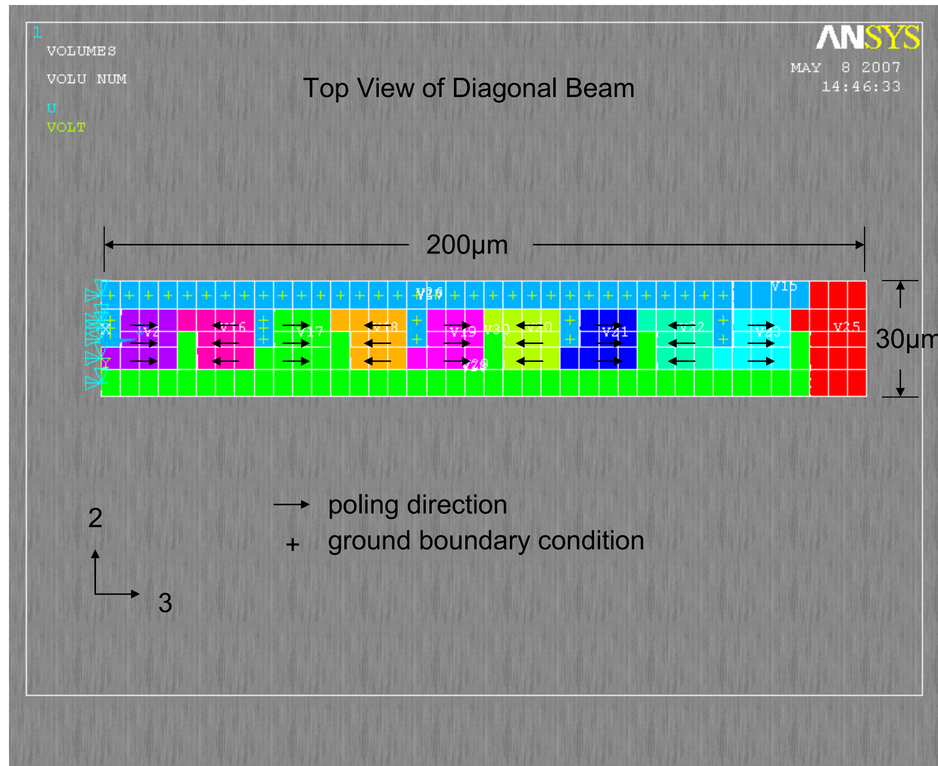

Figure 5.1. The diagonal d_{33} unimorph beam model illustrating the alternating poling directions

Having to model the alternating *d* constants is actually an inherent flaw in the FEA model. In order to successfully model the IDE beam, the poling should first be simulated which would then be applied to the dynamic model. However, no ANSYS model was ever published that successfully models both the non-uniform poling from the IDE layout and the modal analysis together. The alternating *d* constants method was used to help better predict the behavior from the IDE.

The diagonal beam was modeled two ways to consider two poling conditions. The first poling condition is the lower stiffness limit. The lower limit only considers that the areas between the electrodes are poled. The first set of simulations considered the area underneath the electrodes to be "dead" or not poled. This implies that the piezoelectric material is purely mechanical and does not have any electro-mechanical couplings. The dead areas were treated in ANSYS™ by zeroing out the piezoelectric *d* matrix.

The second poling condition is the upper stiffness limit. This condition considers the piezoelectric layer fully poled in the length or 3-direction. The second set of simulations model the area underneath the electrodes having a complete *d* matrix where the values are listed in Table 10. This assumption will make the open circuit case stiffer in comparison to the simulations that consider the area underneath the electrodes to be dead. Because there is some poling under the electrodes the experimental results should lie somewhere in between the lower and upper stiffness limits.

5.1.2 Trapezoidal Beam

The trapezoidal d_{33} unimorph beam model is shown in Figure 5.2. Figure 5.2 depicts the corresponding dimensions of the trapezoidal beam. The beam consists of three layers: substrate, piezoelectric, and electrode. The left end's (the wider, clamped end) cross-section has a zero boundary condition in the 1, 2, and 3 directions. The trapezoidal beam is 50% longer than the diagonal beam and is therefore predicted to have lower natural frequencies.

Unlike the diagonal d_{33} unimorph beam model, the trapezoidal model did not take the alternating poling directions into account. This was because the model became too large and a desktop PC could no longer run the simulation. However for frequency analyses, the poling direction, either being 0° or 180°, has no effect on the modal frequency values.

Both sets of simulations matched the procedure performed on the diagonal beams. The first set of simulations considered the area underneath the electrode to be dead. The second set of simulations considered the entire piezoelectric layer to be poled in the length or 3-direction.

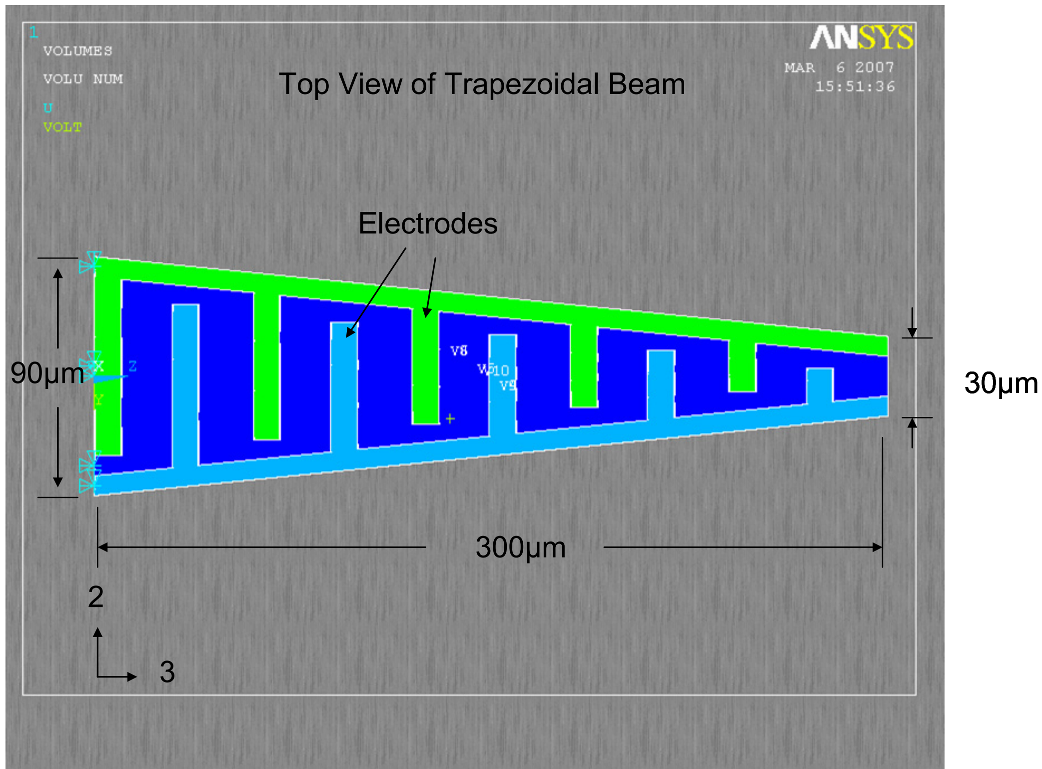

Figure 5.2. The dimensions of the trapezoidal d_{33} unimorph beam

5.1.3 Simulation Results

The results from the ANSYS simulations are in Table 11. Table 11 has two different sets of results for both the diagonal beam and the trapezoidal beam. This is because the beams were modeled to take into account 1) no poling of the area underneath the electrodes and 2) complete piezoelectric layer poling in the 3-direction. In Table 11 the "DA" listed after Diagonal Beam 1 and Trapezoidal Beam 1 refers to the model that considered the Dead Area underneath each electrode. Considering the first mode of the diagonal beam, the percent difference (equation 6.1) in OC and SC frequencies is as large as 0.65% or as small as 0.27%. For the trapezoidal model's first mode the percent difference is 1.02% for the dead area simulation and 1.08% for the completely poled piezoelectric layer simulation.

Table 11. Simulation results from the diagonal and trapezoidal d_{33} unimorph beam model

Diagonal Beam 1 -DA	1st Mode [Hz]	2nd Mode [Hz]	3rd Mode [Hz]	4th Mode [Hz]	5th Mode [Hz]
Open Circuit	19346	117530	214150	320400	399240
Short Circuit	19293	117150	210360	318860	397930
Δ_f	0.27%	0.32%	1.77%	0.48%	0.33%
Diagonal Beam 2	**1st Mode**	**2nd Mode**	**3rd Mode**	**4th Mode**	**5th Mode**
Open Circuit	19419	117840	215000	321100	404140
Short Circuit	19293	117150	210360	318860	397930
Δ_f	0.65%	0.59%	2.16%	0.70%	1.54%
Trapezoidal Beam 1 -DA	**1st Mode**	**2nd Mode**	**3rd Mode**	**4th Mode**	**5th Mode**
Open Circuit	9456.5	50325	99907	134280	245580
Short Circuit	9359.6	49907	99856	133310	245440
Δ_f	1.02%	0.83%	0.05%	0.72%	0.06%
Trapezoidal Beam 2	**1st Mode**	**2nd Mode**	**3rd Mode**	**4th Mode**	**5th Mode**
Open Circuit	9461.6	50354	100240	134360	246350
Short Circuit	9359.6	49907	99856	133310	245440
Δ_f	1.08%	0.89%	0.38%	0.78%	0.37%

5.2 MODELING UNDERCUT

As discussed in Section 4 during the XeF_2 processing the beams were undercut. Therefore, the base is more compliant and undercutting will affect the dynamical model's natural frequencies. In order to understand how undercutting may affect the natural frequencies a diagonal single layer beam was modeled with an undercut.

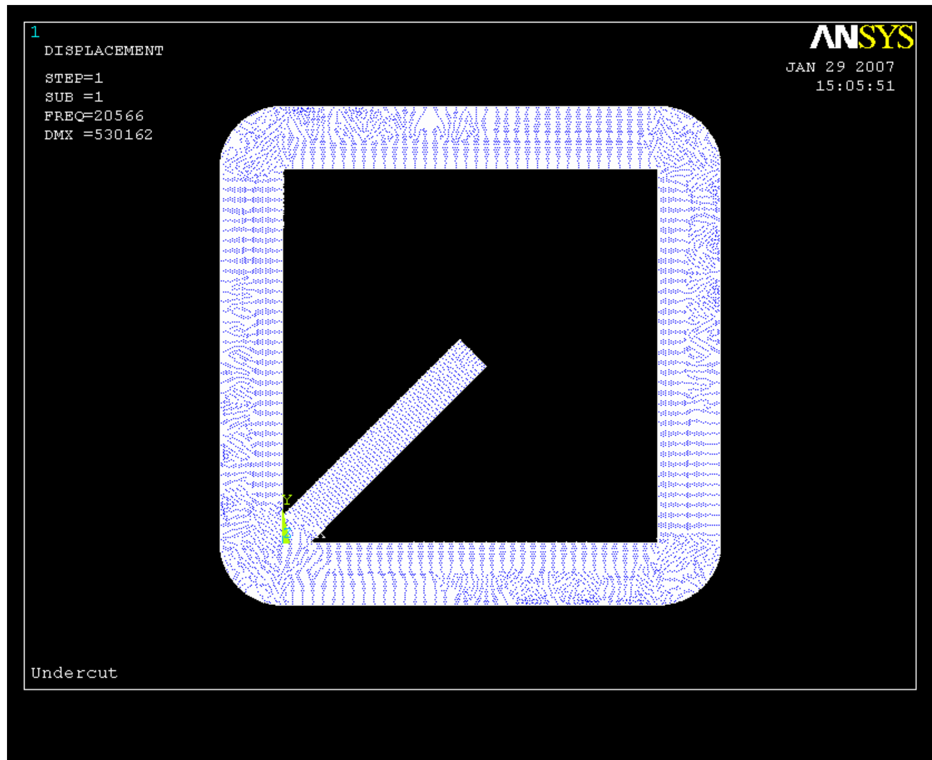

Figure 5.3. The diagonal d_{33} unimorph model with an undercut

If one compares Figures 4.7 and 5.3 the geometric similarities are easily noticeable. Figure 5.3 matches the beam dimensions of the diagonal beam shown Figure 4.7 and assumes a 50µm undercut. Figure 5.3 was compared with the same single layer beam with no undercut. Table 12 provides the difference in natural frequencies when comparing an undercut beam to a beam without an undercut.

Table 12. Compares a single layer beam with and with out an undercut

	1st Mode [Hz]	2nd Mode [Hz]	3rd Mode [Hz]	4th Mode [Hz]
No undercut	23818	149252	311868	418780
Undercut	20566	123790	288699	413270
% difference	-13.65%	-17.06%	-7.43%	-1.32%

As predicted the undercut reduces the stiffness of the structure and all the natural frequencies are reduced.

5.3 MODELING BEAM CURL

After the beams were released, the residual stress in the deposited layers of the wafer caused the beams to curl. In order to understand how the natural frequencies change when the shape is no longer straight, a FEA curved beam model was constructed. This model had the same beam dimensions as the undercut model. Figure 5.4 illustrates the curved beam model. The upward deflection is 40μm which is comparable to the deflection measured in Section 4.5

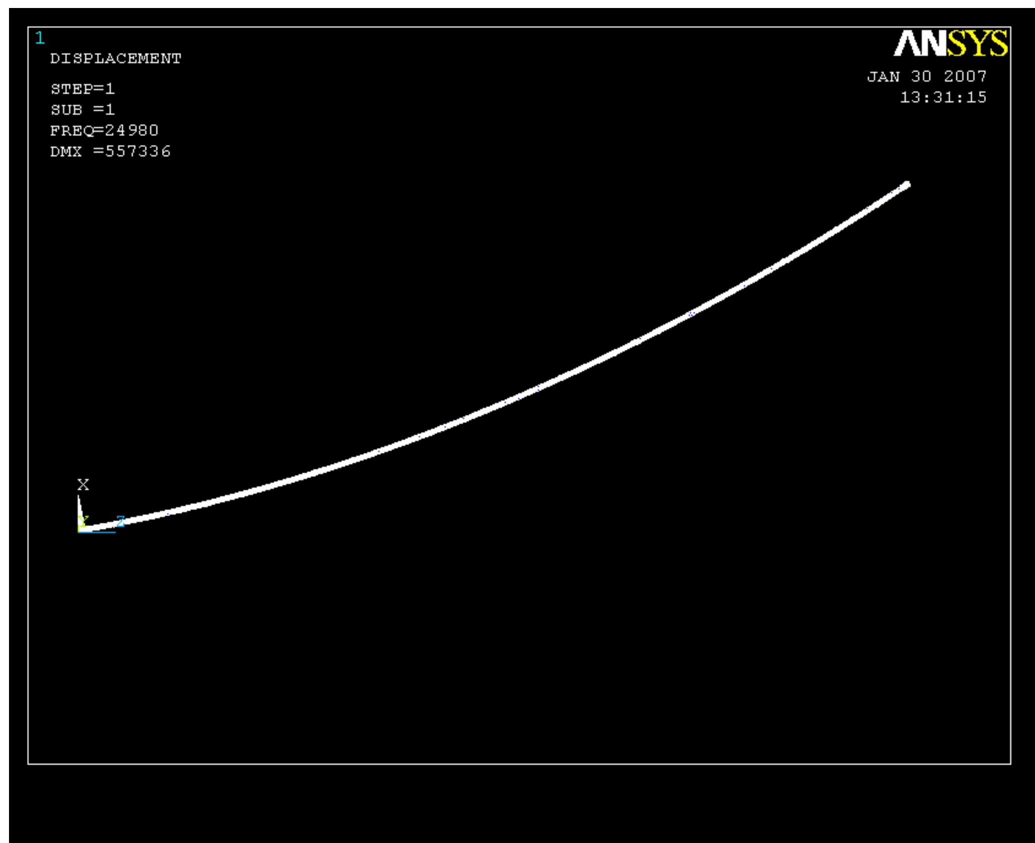

Figure 5.4. Single layer curve beam FEA model

Table 13 is provided to show how the majority of the natural frequencies increase when a beam is modeled with curvature.

Table 13. Compares single layer beam natural frequencies with and without an initial curvature

	1st Mode [Hz]	2nd Mode [Hz]	3rd Mode [Hz]	4th Mode [Hz]
No curvature	23818	149252	311868	418780
Curvature	24980	153920	220500	434970
% difference	+4.88%	+3.13%	-29.30%	+3.87%

It is important to note, however, the large decrease in the 3rd mode. The 3rd mode for this model is first torsional mode. The reason the 3rd mode decreases for the curved beam is because more inertia is produced about the 3-axis. The curved geometry allows for more inertia when the beam is twisting. This can be seen if one were to apply a static torque at the base of a beam. The tip would both translate and rotate. When a beam is straight the translation does not occur. Therefore, the end translation associated with a base torque also implies that the first torsional mode should decrease because the introduction of more mass. Consequently, it is expected that the torsional mode will be much lower in the experimental case when compared to the values predicted by the model in Section 5.1.

5.4 COMPARING THE UNDERCUT AND CURVED FEA MODEL

From Tables 12 and 13 the natural frequency values are shown to decrease for the undercut model and increase for the curved model. The combined effect from undercutting and curling is believed to be nearly balanced. The decreasing in structural rigidity from the undercut model and the increasing in structural rigidity from the curved model effectively balances out for net zero outcome. This is valid for both cases except for the 3rd mode. The 3rd mode's natural frequency decreases for both cases. Therefore, it is predicted that the 3rd mode for the

experimental measurements will be much less than what is predicted by the two models provided in Section 5.1 and 5.2.

6.0 FREQUENCY TESTING AND EXPERIMENTATION

MEMS and macro-scale testing was performed. Both the micro-scale and macro-scale testing was done to show how a structure's frequency can be tuned. The results showed that IDE MEMS sol-gel derived PZT has the capability to be tuned between open circuit and short circuit frequencies. This is a crucial step in resonant tuning of MEMS structures because during the literature review conducted no research was found that experimentally showed sol-gel PZT as a means of tuning resonant structures. The other method of tuning investigated considered a passive way to increase a millimeter scale d_{31} unimorph's open circuit frequency by removing portions of the electrode layer. The MEMS sol-gel derived PZT beams and the d_{31} unimorph beam experimentations illustrated that PZT can be tuned between open and short circuit frequencies and above the open circuit frequency, respectively.

6.1 LASER DOPPLER VIBROMETER FREQUENCY AND MODE SHAPE TESTING

Modal frequencies and shapes were tested using a Polytec μLDV at Carnegie Mellon Univeristy (CMU). However, in order to make frequency measurements the MEMS d_{33} IDE beams had to be scored and broken into separate pieces that were about die size. Each die was then mounted on a wire bonding chip. The wire bonding chip acts as bridge from the micro-scale to the scale

where wires can be manipulated and connected to a measurement tool. Wires were then bonded from the MEMS die to the wire bonding chip using a Kulicke and Soffa Model 523 wire bonder.

After wire bonding the beams were then poled under high electric field to orient the dipoles of the PZT. At this point the beams are ready to be tested.

A vibration stage was built for the micro laser doppler vibrometer (μLDV) measurements. The vibration stage was intended to act as a low pass filter. Because MEMS scale devices are high frequency, the vibration stage protects the MEMS beams from the base transmission of high frequencies.

6.1.1 Wire Bonding

Wire bonding was performed so that the beams had the capability of being electrically connected. Additionally, the MEMS beams were initially in an unpoled state. Wire bonding allowed the beams to be poled.

Wire bonding was performed with the Kulicke and Soffa Model 523 wire bonder in Pitt's JASMiN lab. Using this tool is a very lengthy process. 20-30 μm aluminum wire has to be first threaded through a hole in a stylus that cannot be seen by the naked eye. Precision tweezers help alleviate some of the problems during threading but patience and persistence are a must.

The wire bonder produces a mechanical bond. During bonding the stylus will come into contact with the wafer's bonding pad. When the stylus comes into contact with the wafer's bonding pad, the stylus vibrates. The vibration literally melts the wire to the bonding surface. The first bond is followed by the second and final bond onto the wire bonding chip.

Four parameters need to be adjusted in order to make a successful bond. These parameters are controlled by dials on the wire bonder and are as follows: search, power, force

and tail length. The power setting is the vibration amplitude of the stylus and the force setting is the contact force made when the stylus touches the bonding surface. The search parameter was not used. The tail length is the excess wire produced after the first bond is made. Figure 6.1 is provided to illustrate what the bond looks like under a microscope at 10x.

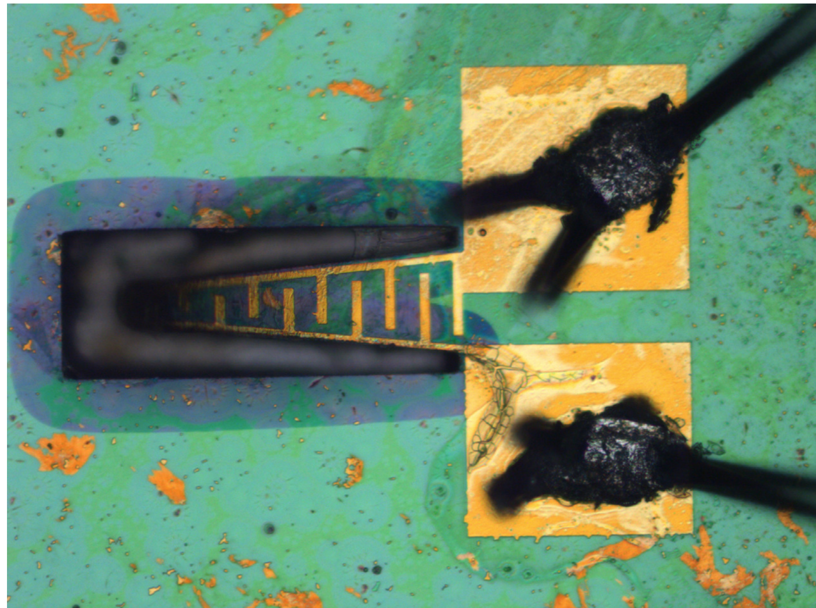

Figure 6.1. Trapezoidal beam illustrating the wire bonded to the gold pads

After both bonds are made the MEMS die and wire bonding chip package is ready for poling. Figure 6.2 shows one of the MEMS beam packages ready for poling and testing.

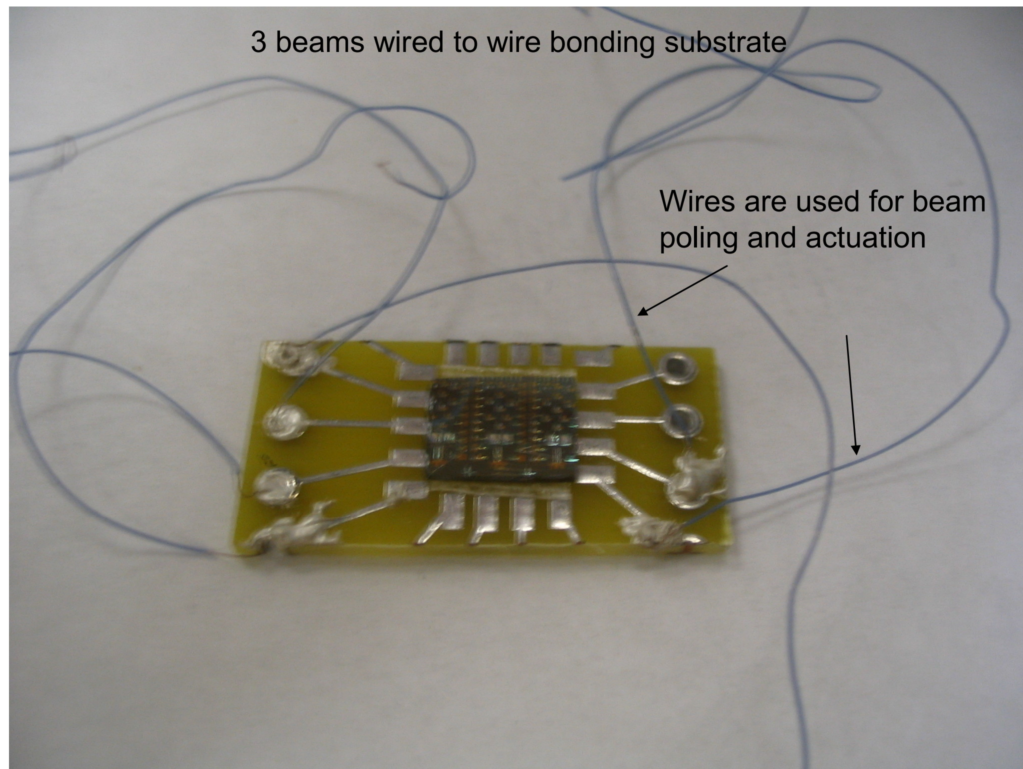

Figure 6.2. MEMS piece wire bonded to chip

In order to understand the amount of electrical impedance added when the wire bond is made, the contact resistance was measured using an Ohm meter. Wire was bonded from contact pad to contact pad on the wire bonding chip. The total resistance was measured collectively which consider the two contact resistances, and the wire resistance. The resistance measured was less than one Ohm. Consequently, contact resistance was therefore assumed to play no role in the electrical operation of the beams.

6.1.2 Poling the MEMS d_{33} IDE Beams

The sol-gel derived PZT creates a piezoelectric layer that is initially in an unpoled state. The dipoles are randomly oriented and need to be aligned in order to produce a net piezoelectric

effect. The dipoles are aligned when subjected to a high electric field. The following steps are used to pole the MEMS piezoelectric beams.

Poling Procedure

1.) First test to make sure the electrodes are not shorted

2.) Place the bonding chip and beam on a hot plate and electrically connect the beams to high voltage power supply

3.) Heat the hot plate to 100°C

4.) When the hot plate gets to the set temperature apply a steadily increasing electric field until the field reaches 4.25-3.5 V/μm. The final voltage value will be the distance between the IDE multiplied by the electric field.

5.) Heat for 30 minutes then turn off the hot plate

6.) When hot plate and wire bonding chip are at room temperature slowly decrease the electric field until zero

In order to understand why these beams are poled at an elevated temperature, please refer to the domain poling section (Section 2.1.1).

Measuring the deflection of MEMS piezoelectric beams while varying the poling electric field was done in Hong, 2006. Hong poled beams with different electric fields. Subsequently, tip deflection measurements were made when the beams were actuated with various voltages. Hong reported that the beams deflected the most when they were poled at high electric fields. The knowledge gained from Hong was applied to the above poling recipe. However if too high of a poling voltage is used arching may occur. Figure 6.3 shows what can happen when an electric field is too high during poling.

Figure 6.3. Illustration of a beam that literally exploded during poling. This was the result from an electric field that was too large

6.1.3 Vibration Stage

Following poling, the MEMS beams were tested using a μLDV. However, in order to minimize the amount of vibration noise during the μLDV measurements a low pass vibration stage was built.

A low pass vibration stage when modeled as a single degree of freedom system consists of a relatively large mass connected to a compliant spring. Relating the single degree of freedom system to equation (3.45), the fundamental frequency will be low relative to what is being tested. Frequencies greater than the fundamental frequency will be attenuated and thus whatever is stationed on top of the mass will barely see any high frequencies transmitted from the base.

In order to emulate the spring-mass single degree of freedom system, a vibration stage was built. A relatively large seismic mass in comparison to the test mass was placed onto a compliant spring-like surface. 3/4" neoprene foam rubber was used as the compliant surface.

The neoprene foam rubber was cut in a 6x6" section where a 73g cylindrical mass was placed in the middle. On top of the seismic mass a 5x5x2mm PI Technology PZT excitation source was used to vibrate the MEMS beams. The actuator was picked to have linear frequency response function greater than 300kHz. The vibration stage is shown in Figure 6.4.

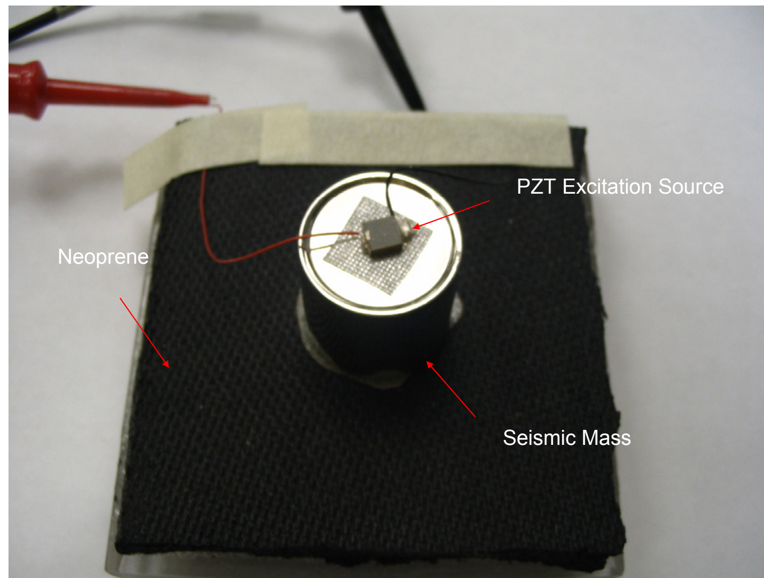

Figure 6.4. Overhead view of the low-pass vibration stage used

In order to verify that the vibration stage shown in Figure 6.4 has fundamental frequencies below 1 kHz two different types of vibration measurements were taken. The first measurement was done as a way of checking to make sure the first natural frequency of the system was adequately low. The second vibration measurement was done using a μLDV to ensure the linear frequency response of the PZT base actuator.

The first vibration measurement was performed using an accelerometer. This was done by using an inductive shaker as the base vibration source. The shaker frequency was swept manually using a function generator. The output amplitude of the accelerometer was visually watched. Table 14 provides the fundamental frequency values obtained during this measurement.

The accelerometer's output was attenuated to low amplitude noise after the frequencies listed in Table 14. This signal attenuation acts as evidence for a low pass filter. The surface spring constant values listed in Table 14 are inferred from the mass and frequency data.

Table 14. First vibration measurement data and calculated surface spring constants

Vibration Stage Frequency Measurements and Calculated Spring Constants

Measurement	Siemic Mass	Accelerometer Mass	Frequency	Surface Spring Constant
1	73grams	23grams	117.2Hz	1.318kN/m
2	73grams	23grams	146.5Hz	2.060kN/m

The second vibration measurement was done using the μLDV at CMU. This measurement was done in order to ensure that the frequency response of the vibration stage and excitation source (PZT shaker) on top of the seismic mass remained constant at high frequencies. A non-constant frequency response would imply that energy transferred into the systems would vary and not remain constant. This could result in false readings. A pseudo-random voltage signal was used to excite the PZT exciter. The frequency response of the vibration stage is shown in Figure 6.5. The measurement setup of the μLDV is provided in Figure 6.6.

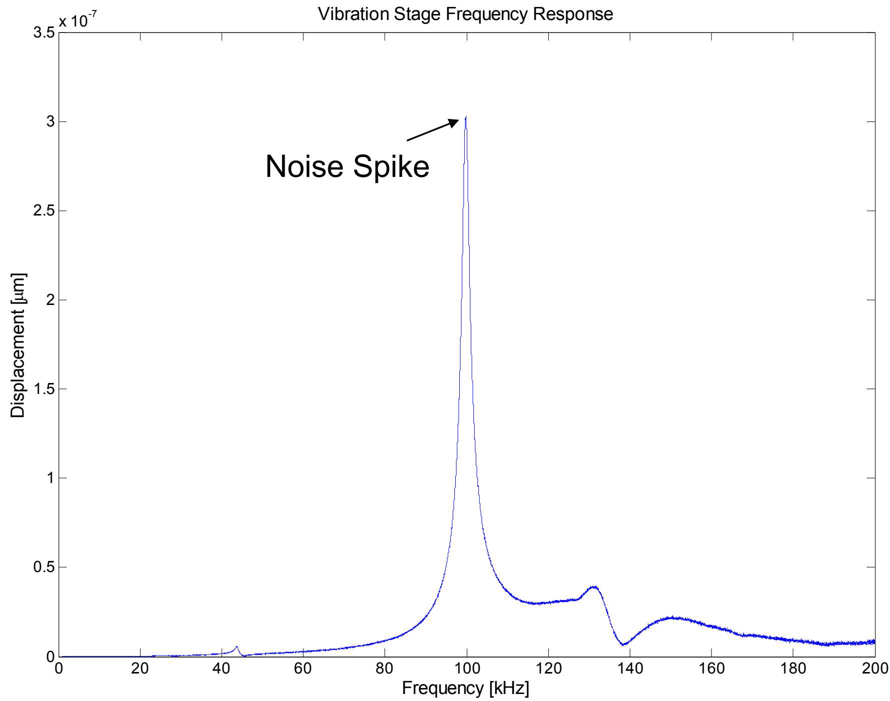

Figure 6.5. The frequency response of the vibration stage when the PZT shaker is excited

The vibration stage acted as a good low pass filter. The frequency response of the vibration stage system remained linear except around the noise spike at 99.5 kHz. The noise spike was concluded through both multiple scan point, non-reference analyses, and the fact that the peak remained in the same location for different test packages to be some kind of non-mechanical electrical noise. Ignoring the noise spike, the vibration stage acted as a good low pass filter. The PZT excitation source's response remained flat from 1 kHz to 80 kHz. Verifying that the stage had a fundamental frequency below 1 kHz and that the excitation response remained flat both provided reasonable justification that the vibration stage built was applicable to MEMS beams frequency measurements.

6.1.4 MEMS μLDV and Mode Shape Measurements

A Polytec MSA-400 Micro System Analyzer (μLDV) was used to make frequency measurements of the MEMS beams. The beams were placed onto the vibration stage on top of the PZT exciter. Two lasers were used to provide the frequency response data. One of the lasers is used as the output signal and the other laser is used as the reference signal. Inside the Polytec μLDV both of the lasers initially goes through a beam splitter so the reflected signal can be compared to a stationary signal. During measurements the reference laser was positioned at a stationary base position of the beam and the output signal laser was placed on the beam. Both areas where the laser was placed had to have good reflectivity. The laser light is then modulated from the vibrating structure and reflected back to the objective. Ideally, the output signal laser should be placed at the tip of the beam when measuring the fundamental frequency but because the beams curled after release this was impossible. Therefore, the output signal laser was placed as far as possible from the beam's base while still allowing adequate laser reflection.

The base excitation source was excited using a high voltage pseudo-random signal. A wide signal bandwidth was used to first establish the MEMS beam's response and subsequently the natural frequencies. Then after the natural frequencies were verified the signal bandwidth was decreased to focus around a specific natural frequency. The pseudo-random signal was amplified using a Krohn-Hite Model 7500 high voltage amplifier. This amplifier is designed to have a large linear bandwidth of amplification. Figure 6.6 is the schematic of the μLDV measuring system used at CMU.

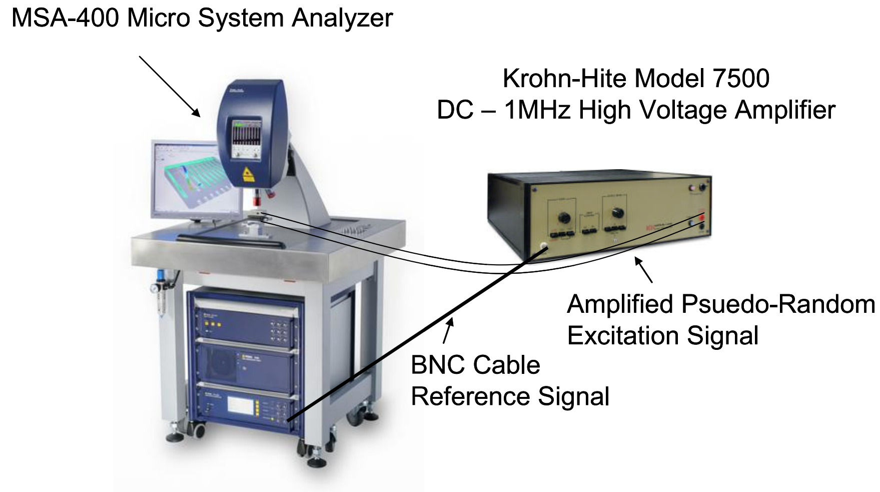

Figure 6.6. Schematic of the μLDV measuring system used at CMU

Two types of beams where tested. The first series of tests obtained frequency data for the diagonal beams shown in Figure 4.7. The diagonal beams where chosen for two reasons: 1) the beams had electrodes that were aligned properly and 2) the beams had large and deeper etching pits. As mentioned before, during processing the electrode layer was slightly misaligned. The misalignment is thought to be from the residual stress gradient through the wafer's thickness. Luckily, most of the diagonal beams remained aligned. The large etching pits were also advantageous because squeeze-film damping is much lower. Squeeze-film damping depends highly on the distance from the bottom of the beam to the substrate. The large etching pits had a faster etching rate and, therefore, had a greater distance from beam to substrate.

The diagonal beams were tested three ways: 1) beam excitation, 2) open-circuit, and 3) short circuit. The beam excitation case is when the beams were electrically connected to the amplified pseudo-random voltage signal. The open and short circuit cases correspond to using the PZT exciter as the vibration source. Open circuit means the leads on the MEMS diagonal

beam are not connected to anything while short circuit means that the leads are connected to each other. Figure's 6.7-6.9 are frequency response plots of each testing case, respectively.

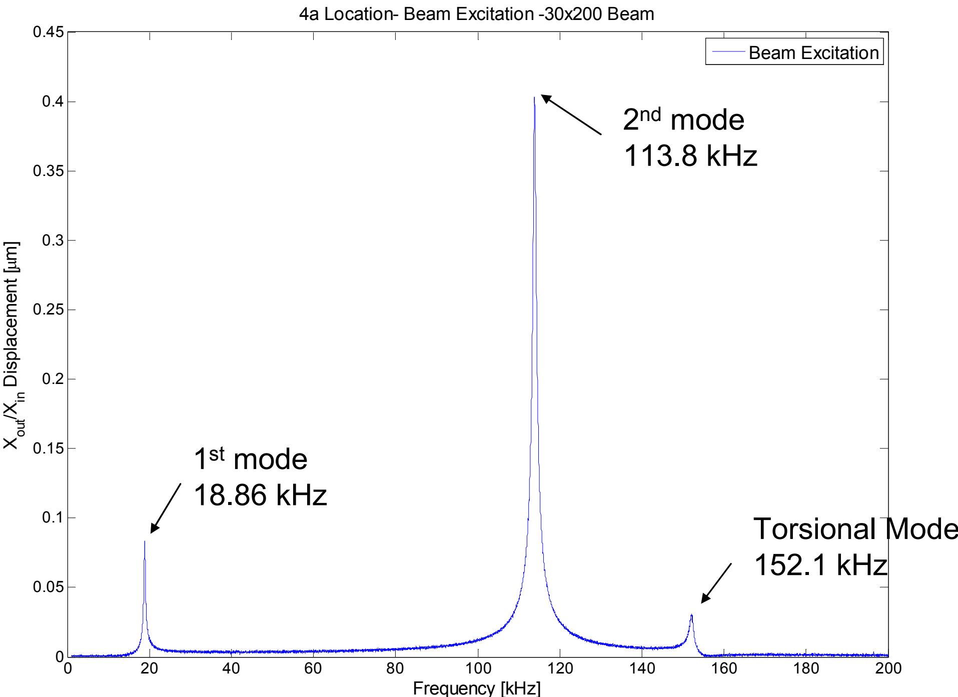

Figure 6.7. Diagonal Beam Excitation- Displacement-out per displacement-in frequency response

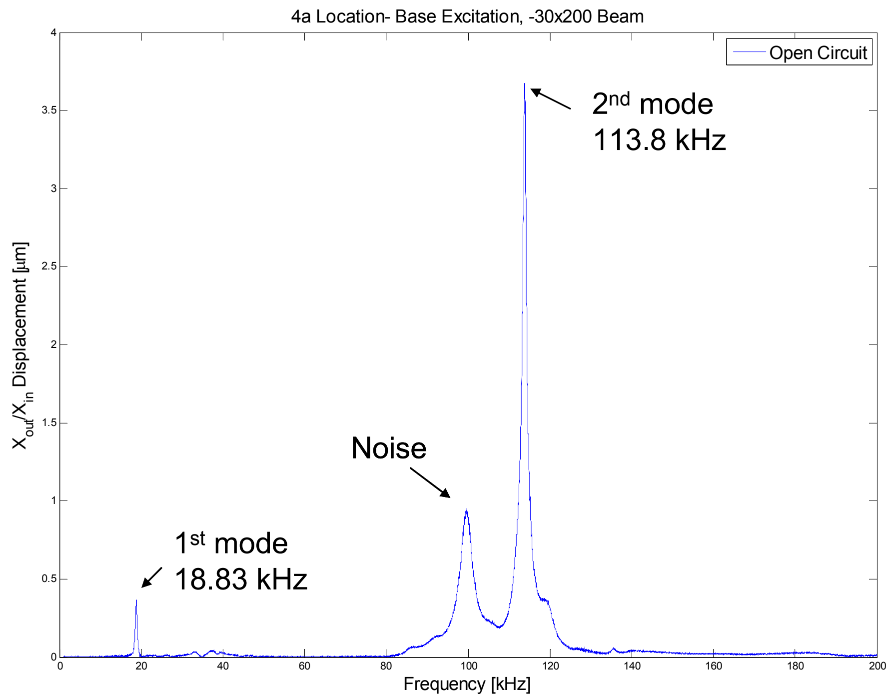

Figure 6.8. Base Excitation, Open Circuit Diagonal Beam- Displacement-out per displacement-in frequency response

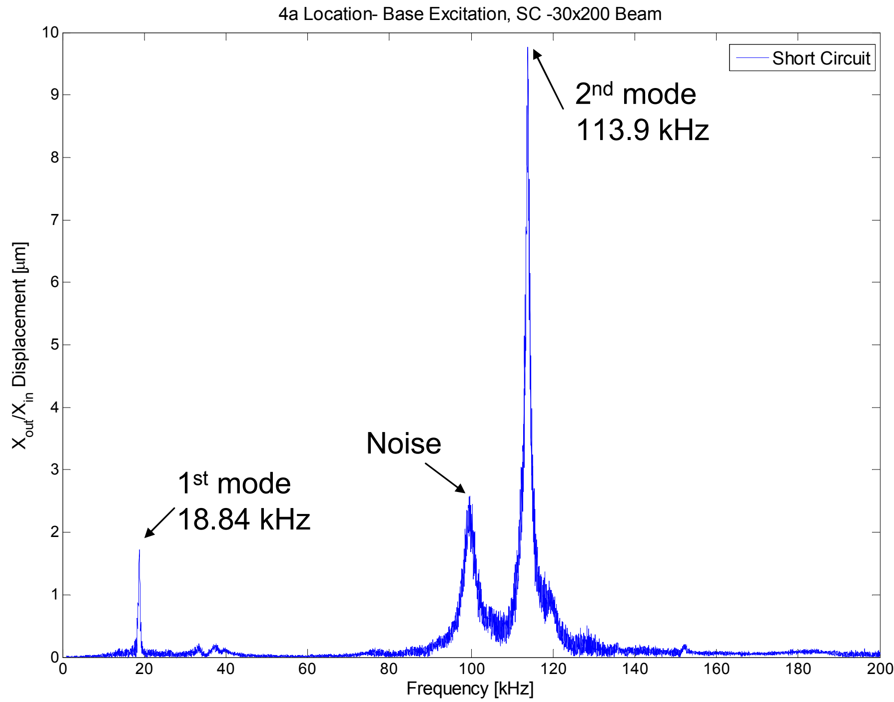

Figure 6.9. Base Excitation, Short Circuit Diagonal Beam- Displacement-out per displacement-in frequency response

From Figures 6.8-6.9 the OC modal frequencies actually decrease rather than as expected increase from their SC counterparts. The pseudo-random input signal was changed to focus around the first mode. No difference was found between the open circuit frequency and short circuit frequency. The conclusion was made that even though the PZT was successfully poled (Figure 6.7 was evidence) the difference between open circuit and short circuit was undetectable. The reason for this will be explained in IDE Poling Optimization, Chapter 7.

The next set of beams to be tested is the trapezoidal beams (Figure 4.8). These beams were tested in the same manner as the diagonal beams. Frequency measurements were obtained for beam excitation, open-circuit base excitation, and short-circuit base excitation. Figure's 6.10-6.12 plot the displacement response functions.

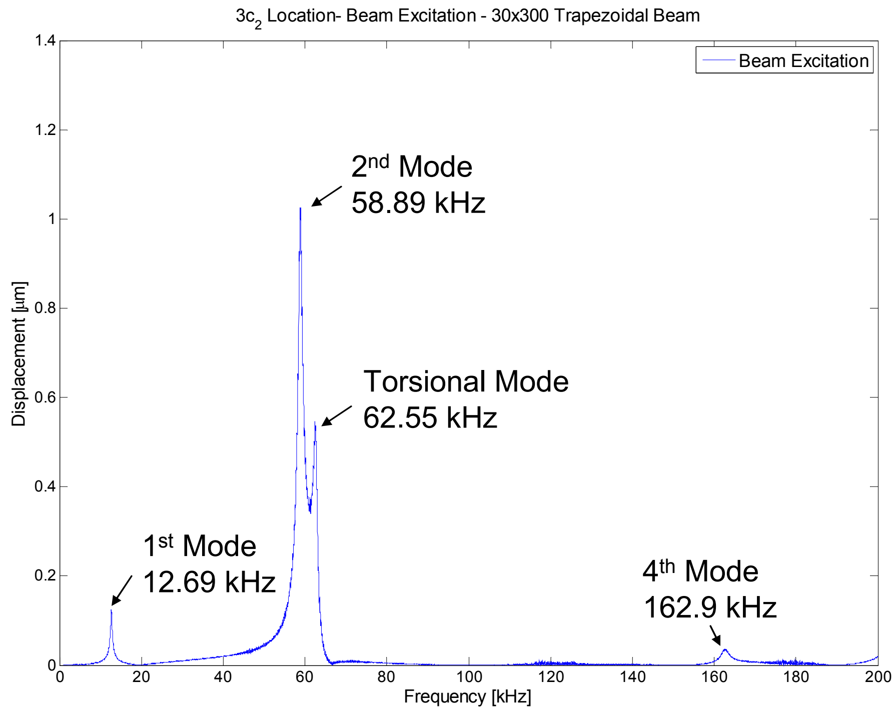

Figure 6.10. Trapezoidal Beam Excitation- Displacement-out per displacement-in frequency response

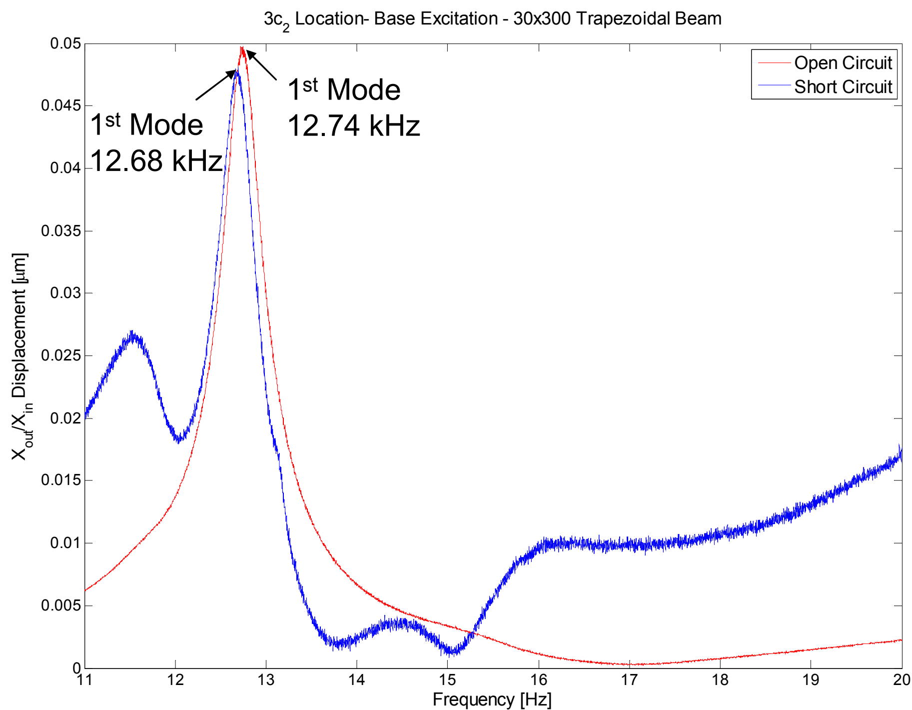

Figure 6.11. Trapezoidal Beam – Open and short circuit frequency response for the 1st mode

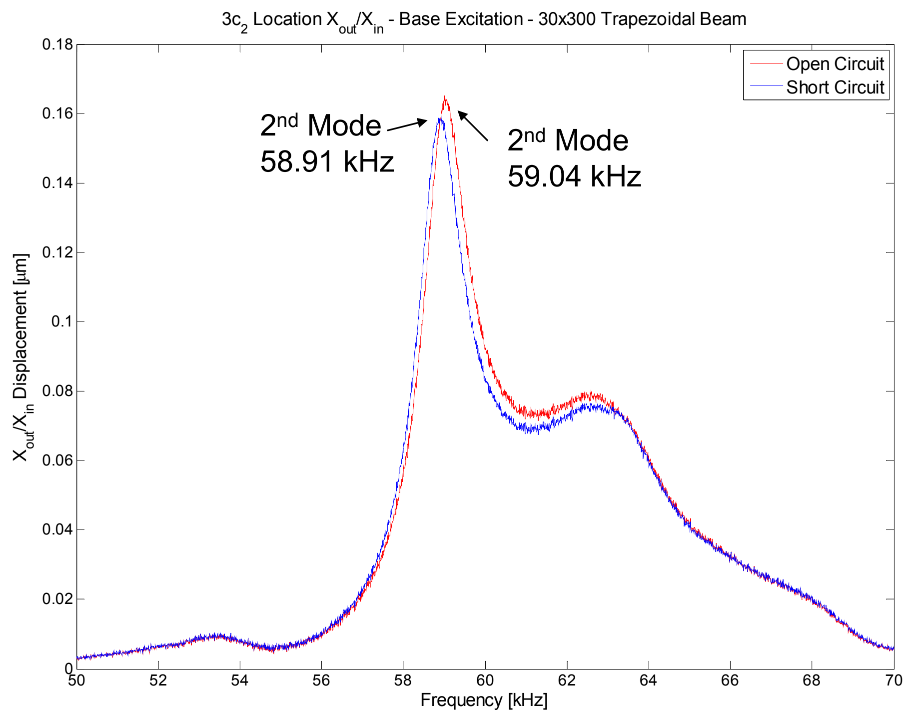

Figure 6.12. Trapezoidal Beam – Open and short circuit frequency response for the 2nd mode

Figure's 6.11-6.12 illustrate that the trapezoidal beams have different bending frequencies for the open circuit case and short circuit case.

6.1.5 μLDV Results

The modal frequency results are listed in Table 15 and are compared to the modal analysis conducted using ANSYS™. In order to characterize the open circuit to short circuit frequency range the following equation is used to define the percent tuning, Δ_f, associated with the sol-gel derived PZT beams

$$\Delta_f = \frac{f_{oc} - f_{sc}}{f_{oc}} \tag{6.1}$$

where f_{oc} is the open circuit frequency and f_{sc} is the short circuit frequency. The frequency resolution using the Polytec μLDV with a fft length of 12800 is 1.562 Hz, 7.810 Hz, and 15.625 Hz for bandwidths of 20 kHz, 100 kHz and 200 kHz, respectively.

Table 15. The experimental and simulation percent tuning

Diagonal Beam 1	1st Mode	2nd Mode	3rd Mode	4th Mode
Simulation 1-DA				
OC	19346	117530	214150	320400
SC	19293	117150	210360	318860
Δ_f	0.27%	0.32%	1.77%	0.48%
Simulation 2				
OC	19419	117840	215000	321100
SC	19293	117150	210360	318860
Δ_f	0.65%	0.59%	2.16%	0.70%
Testing				
OC	18.78-19.14 kHz	113.8-113.9 kHz	152.1 kHz	Not tested
SC	18.77-19.13 kHz	113.8-113.9 kHz	152.1 kHz	Not tested
Δ_f	-0.05%-0.00%	-0.09%-0.00%	0.00%	Not tested

Trapezoidal Beam	1st Mode	2nd Mode	3rd Mode	4th Mode
Simulation 1-DA				
OC	9456.5	50325	99907	134280
SC	9359.6	49907	99856	133310
Δ_f	1.02%	0.83%	0.05%	0.72%
Simulation 2				
OC	9461.6	50354	100240	134360
SC	9359.6	49907	99856	133310
Δ_f	1.08%	0.89%	0.38%	0.78%
Testing				
OC	8.975-13.82 kHz	56.09-59.04 kHz	62.55 kHz	Not tested
SC	8.969-13.81 kHz	55.95-58.91 kHz	62.55 kHz	Not tested
Δ_f	0.30-0.60%	0.20-0.40%	0.00%	Not tested

The reason why the diagonal beams had negative and nearly undetectable change in frequency is investigated in Chapter 7.

The lower limit of the frequency ranges listed for trapezoidal beam testing results is calculated by subtracting the maximum short circuit frequency from the minimum open circuit frequency. Likewise, the upper limit on the trapezoidal frequency range is determined by subtracting the minimum short circuit frequency from the maximum open circuit frequency. Therefore, the frequency range listed in Table 15 captures the variability in the data measured.

From Table 15, one may notice the large difference between the simulation 3rd mode and the experimental testing 3rd mode (the 3rd mode here is the 1st torsional mode). The FEA modal simulations did not take into account the undercutting and curvature of the MEMS beams. This was because the simulated undercut model decreased the modal frequencies and the curved model increased the modal frequencies. Therefore, the net effect from undercutting and curvature was assumed to balance out. However, the 3rd mode for both simulations decreased. Therefore, the large difference in experimental and simulation was expected.

6.2 MACRO-SCALE OPEN CIRCUIT TESTING

Open circuit testing was also performed using a millimeter scale beam. The sole purpose for this testing was to show that the open circuit modal frequencies can be increased. In recent literature, Muriuki (2004), Frederick (2006), and Charnegie (2007), the open circuit condition was considered to be the maximum stiffness scenario. Therefore, they showed that structural frequencies can be tuned below the open circuit condition by adding a shunt capacitor. The following equation was used to characterize the change in compliance.

$$s^{SU} = s_{33}^{E} - \frac{d_{33}^{2} A_c}{L} Z^{EL} \tag{6.2}$$

As mentioned in Section 3.3, equation (6.2) was derived in Clark (2000) assuming a constant stress. Constant stress implies that charge will form uniformly on the electrode. However, stress is linearly varying for a beam with an end load. The maximum stress occurs at the base and when related to the piezoelectric constitutive equations (Table 2), the base is the

point of maximum electric field. Unlike Clark's model the electric field is no longer constant but is linearly varying in the beam model. Thus, the charge produced is no longer constant.

The electrodes layer on the PZT is used in a manner to capture the charge generated from bending. However, the electrode actually averages the charge generated because it's conductive (allowing charge migration) making the voltage generated constant on the electrode. Since charge and voltage are related by capacitance both charge and voltage become constant (not length dependent). Constant voltage on the electrode implies than that the electric field is constant. This means that when a beam is fully covered by an electrode the beam is not as stiff as equation (6.2) because the electric field through the PZT layer is an averaged electric field. If the electrode is not fully covering the beam, from the base to a distance d, the electric field through the PZT thickness increases. The maximum stiffness case occurs when the beam does not have an electrode layer. The case where the beam is fully covered by an electrode and open circuit means that the stiffness is somewhere between the no electrode case and the fully covered electrode case where the leads are short circuit.

To show that the OC beam condition is not truly the stiffest condition, a PZT beam was dynamically tested. The PZT beam was a d_{31} bimorph which has 0.2667 mm PZT on both sides of the 0.254 mm aluminum substrate. The beam dimensions were 36 mm length by 30 mm width. The beam's base was excited by an inductive shaker. Siglab Model 20-42 was used to characterize the frequency response when a random signal was amplified and inputted into a shaker. After each measurement the beam's electrodes were etched incrementally 1 mm from the free end. Etching the electrodes decreased the beam's capacitance. Eight frequency measurements were taken and the PZT electrodes were etched for a total amount of 7 mm from the free end. Figure 6.13 plots these results.

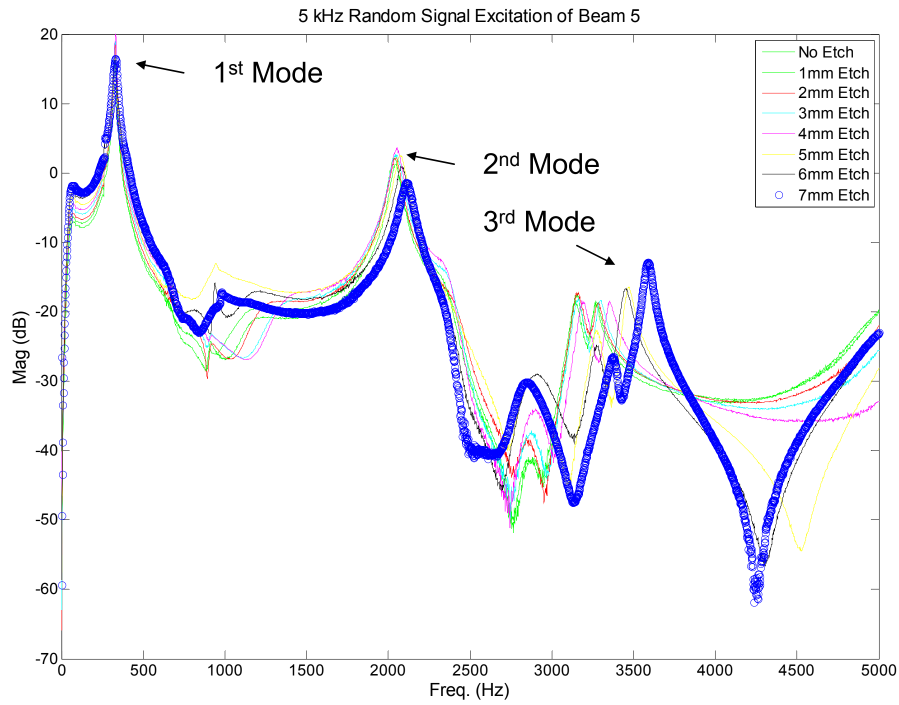

Figure 6.13. Plot illustrates how the OC frequency can be shifted if the beam's electrode is partially removed

Figure 6.14 is close up of the second mode. The frequency shift is easily noticeable.

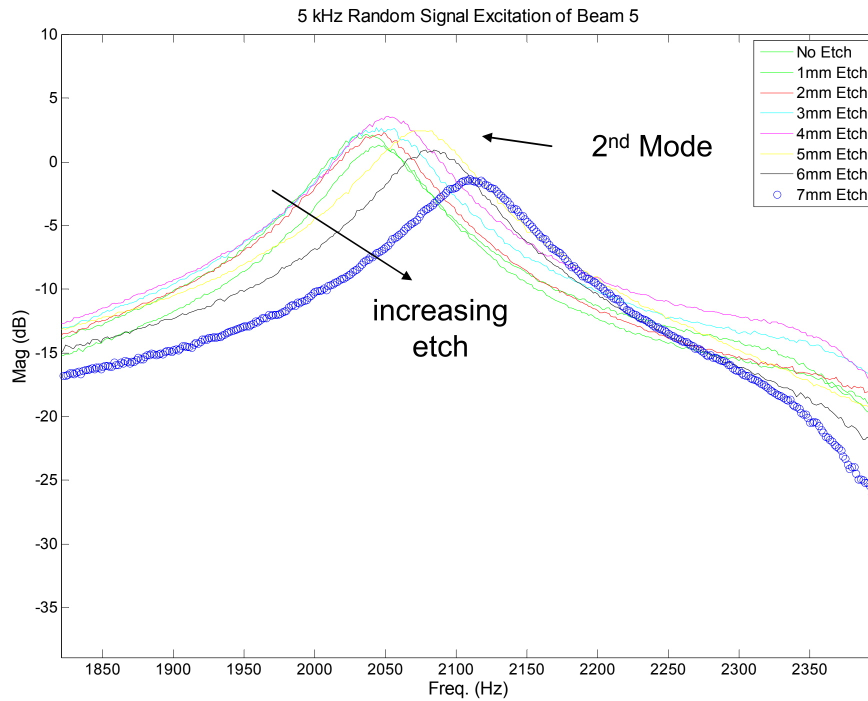

Figure 6.14. Close up of the second mode

The blue circles correspond to 7mm etch which is the highest frequency.

Figure 6.14 shows how the effective stiffness of the beam increases when the electrode is etched. The maximum stiffness condition cannot be electrically measured because the electrodes would not exist anymore and therefore the beam could not be electrically connected.

Figures 6.13 and 6.14 are great evidence that a piezoelectric structure's open circuit frequency can be increased. This has a significant impact on modeling the tunablility of piezoelectric structures. Future work is needed to help mathematically characterize what is happening in Figures 6.13 and 6.14.

6.3 RESULTS SUMMARY

The experiment results are listed below

- A vibration stage was built that is suitable for MEMS dynamics
- MEMS IDE sol-gel derived PZT trapezoidal beams are shown to have a tuning range of 0.3-0.6% of the open circuit frequency
- The open-circuit frequency of a millimeter-scale PZT beam is shown to increase when the electrode area is decreased

Each experimental result showed that piezoelectric applications have the ability to tune their resonant frequency between an open-circuit and short circuit frequency. Additionally, the open-circuit frequency is redefined to be a frequency between the maximum stiffness case and the short-circuit case.

7.0 INTERDIGITATED ELECTRODE ANALYSIS AND OPTIMIZATION

The poor results from the diagonal beam measurements in Section 6.1 motivated IDE analysis and subsequently the IDE optimization. The poling electric field was first examined to help understand why there was no difference between open circuit and short circuit frequencies for the diagonal MEMS beams. Following the simulation of the diagonal beam's poling electric field, the non-uniform electric field loss mentioned in Section 3.2.2 is reiterated. A model is produced that simulates various IDE geometries and calculates the electric field density in the piezoelectric layer. An optimal electrode width to piezoelectric layer thickness ratio is found from the FEA simulations. Finally, the planar IDE loss or percent poling is analyzed. The percent poling values obtained can be related to equations (3.35-3.36).

7.1 SIMULATION OF POLING ELECTRIC FIELD

In order to understand why the diagonal beams performed so poorly during the open and short circuit frequency tests an FEA model was created. The diagonal beams were poled successfully. Figure 6.7 is evidence of the beam being actuated. Therefore, the electro-mechanical coupling for a 3-direction stress was thought to be somehow deteriorated such that actuation was still achievable, but tuning was not.

To better understand what direction the PZT is being poled for the IDE configuration a model was built that simulated the electric field during poling. Figure 7.1 shows the top view of the IDE diagonal beam. The picture on the left in Figure 7.1 is the actual ANSYS™ model. The picture on the right of Figure 7.1 shows the same picture as on the left except that the IDE electrodes are superimposed onto the model to making the IDE easier to distinguish.

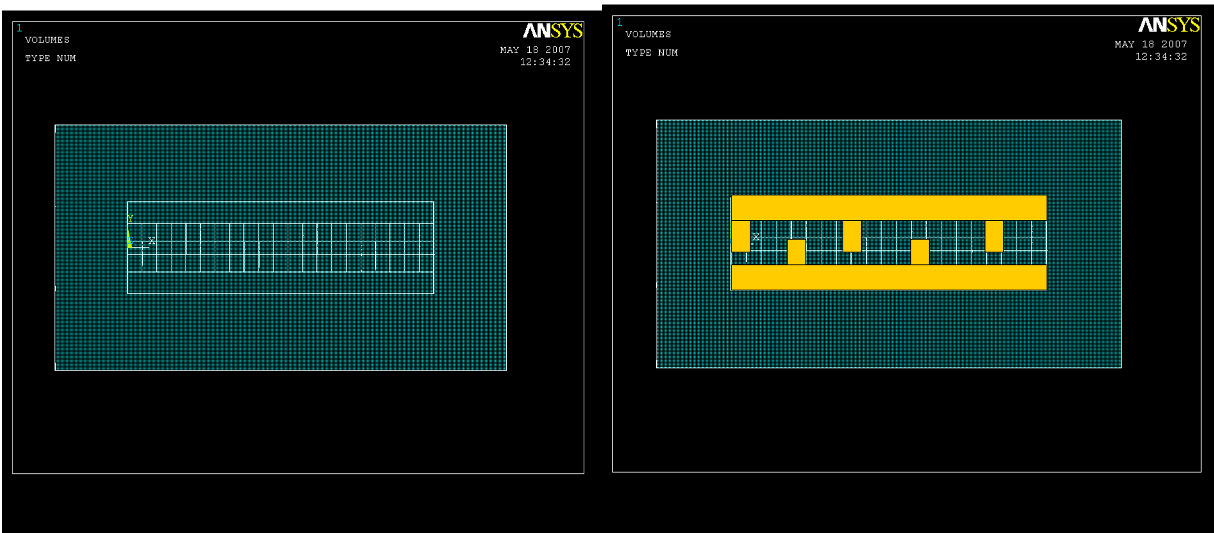

Figure 7.1. 3-D FEA model of the diagonal beam

The beam is surrounded by air to help accurately model the electric field. The green area in Figure 7.1 resembles air. Inside the green area is the diagonal beam. Two electrodes on each side of the beam run down the length of the beam. These electrodes are connected to electrode fingers that run parallel to the width.

The poling voltage was set to 75 Volts on one electrode and 0 Volts on the other. The electric field results are shown in Figure 7.2.

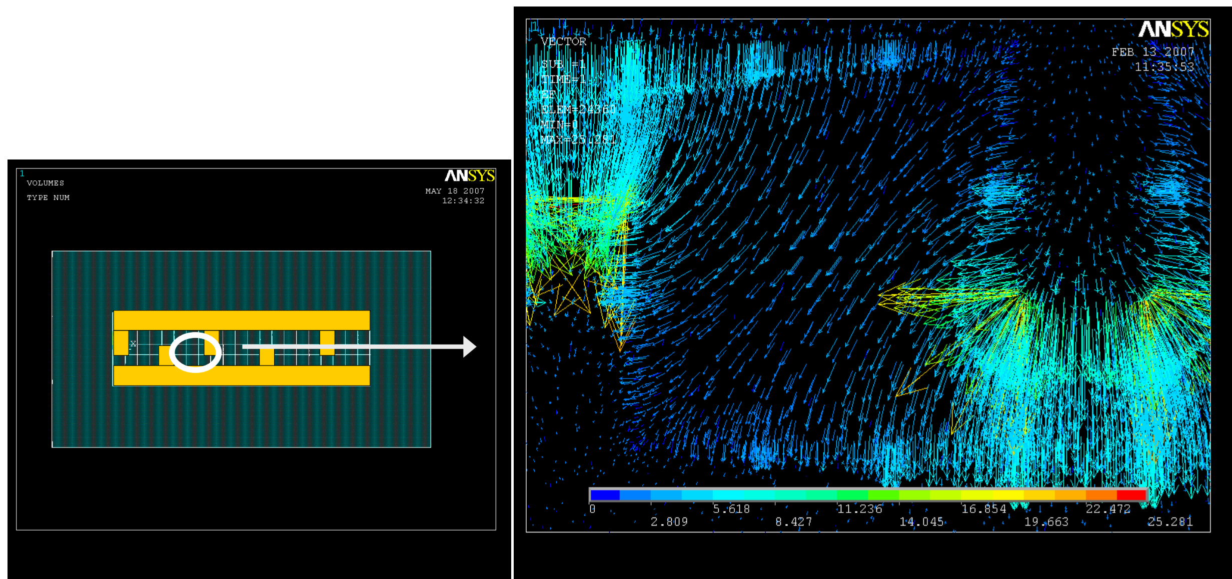

Figure 7.2. Electric field between two electrodes for the diagonal beam

Figure 7.2 shows a close-up of the electric field vectors between two electrodes. The picture to the left in Figure 7.2 highlights the area in between the electrodes where the picture on the right is zoomed into. Since the electrodes are conductive they appear as darker spots on Figure 7.2. This analysis was 3D so some of the electric field vectors do point in directions into and out of the page. The corona effect is produced at the corners and edges of the electrode. This is because the magnitude of electric field is inversely proportional to radius of curvature. The poling electric field has two major directions: 1) the diagonal direction between each electrode and 2) in the width direction. Therefore conservatively, less than half (and probably much lower) of PZT was poled in the length or the assumed 3-direction. The 3-direction is assumed to be in the length direction for an IDE d_{33} unimorph.

A small amount of the PZT being poled in the length direction provides some better insight on why the diagonal beam's OC and SC frequencies were not different. Another reason for undetectable differences in frequencies could be from poor PZT quality. The combination of

poling the PZT incorrectly and the possibility that the PZT had relatively small *d* constants provides better insight on why the OC and SC frequencies for the diagonal beam were nearly the same.

7.2 IDE ELECTRO-MECHANICAL LOSS

When poling a piezoelectric material using an IDE (interdigitated electrode) configuration, electric fields under the electrode are not in the assumed 3-direction along the length of the beam. This is shown in Figure 7.3. Non 3-direction electric field implies that the piezoelectric layer is not completely poled in a single direction. Therefore, in the region underneath the electrodes, stress in the 3-direction cannot be completely coupled with the d_{33} constant of the material.

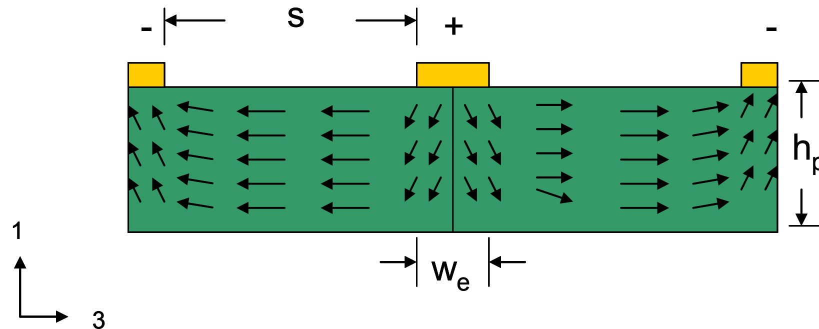

Figure 7.3. Illustration of the non-uniform electric field that exists underneath the electrodes during poling

No method has been developed that investigates the exact loss associated with IDE poling. Equations (3.35-3.36) use a $\%d_{33}$ factor that represents the amount of poling between

and under each electrode that is in the assumed 3-direction. In order to characterize $\%d_{33}$ FEA was utilized.

Subsequently, after the IDE beam is poled the dipoles are non-uniform. This is because some of the dipoles will be pointing in the diagonal/skewed direction. A dipole pointing in the diagonal direction (having a length-direction component and a thickness-direction component) will have an output in that corresponding diagonal direction. Output here is being used as a generalized term that can be related to either the strain output from an applied electric field or an electric field output from an applied stress. FEA is also used to characterize the percent output from various IDE geometries.

7.3 INTERDIGITATED ELECTRODE FEA OPTIMIZATION

In order to characterize the non-uniform poling orientation developed from the high electric field applied during poling, ANSYS™ software was used. Similar work was also done in Bowen (2006). However, Bowen (2006) considered a PZT-fibre composite with, more importantly, IDEs on both the top and bottom sides of the sample. The IDE considered here has only one IDE pattern which is on top of the beam. To date no resource has been published that examines a MEMS scale unimorph IDE poling electric field. It is also important to note that the following analyses assume grain sizes for sol-gel PZT are to be relatively small (500-1000 Å) and very dense (Kwon, 1999). The results found here are close to what was found in Bowen (2006) only slightly higher.

A 2-D ANSYS™ model (in the plane shown in Figure 7.3) was made consisting of two electrodes on top of a PZT layer. The PZT layer was mounted on top of a substrate layer. Figure

7.4 illustrates the ANSYS 2-D model and its corresponding dimensions. Here the IDE electrode width is divided by two because when a structure has multiple IDEs half the electrode is associated with one poling direction and the other half electrode is associated with the other poling direction (as shown in Figure 7.3 where the center electrode contributes to poling on its left and right).

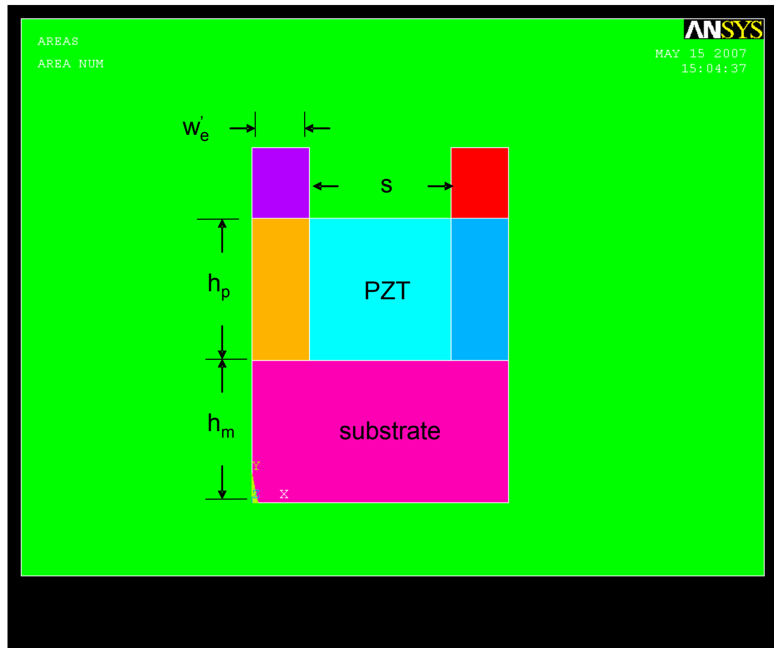

Figure 7.4. 2-D ANSYS model with variable dimensions

Plane 230 elements were used to model the electric field produced during poling. Table 16 list the electric properties used in the simulation. The values are scaled down to μMKS units.

Table 16. Electrical values used for IDE Optimization

Material	Relative Permittivity	Resistivity [Ohm/μm]
Air	1.0005	3.00E+07
PZT	x: 900 y: 900 z:1100	1.00E+00
Electrode	0	1.00E+07
Substrate	4	1.00E-14

The command “emunit, epzro, 8.8542e-6” had to be used to change the permittivity constant into μMKS units.

Referring to Figure 7.4 the simulation was conducted as follows:

- The spacing, *s*, between the electrodes was varied from 1.0-40.0 μm
- For each spacing value the, ratio w'_e/h_p was varied from 0.1-20.0
- The poling voltage is dependent on the spacing, *s*, and is equal to $V_{poling} = 4s$. This creates what would be a constant electric field if the PZT were located directly between the electrodes.
- After each simulation the electric field inside the PZT layer was searched through its area and electric field values greater than 1 V/μm were set equal to one or otherwise zero. The 1 V/μm threshold assumes that the PZT is successfully poled.
- The resulting electric field data was integrated and average by dividing by the PZT area, $(w_e + s)h_p$
- The average electric field was divided by the poling electric field value to get a percent of PZT poled value

The main assumption for the simulations is that the PZT was considered to be successfully poled if the corresponding electric field was greater than or equal to 1 V/μm. Figure 7.5 shows the results from the ANSYS simulations. The plot illustrates the percent of PZT poled for both increasing electrode width to PZT layer thickness ratio and electrode spacing. It is worth noting that a spacing value of 40 μm is large and the high voltage associated with the poling may lead to arching.

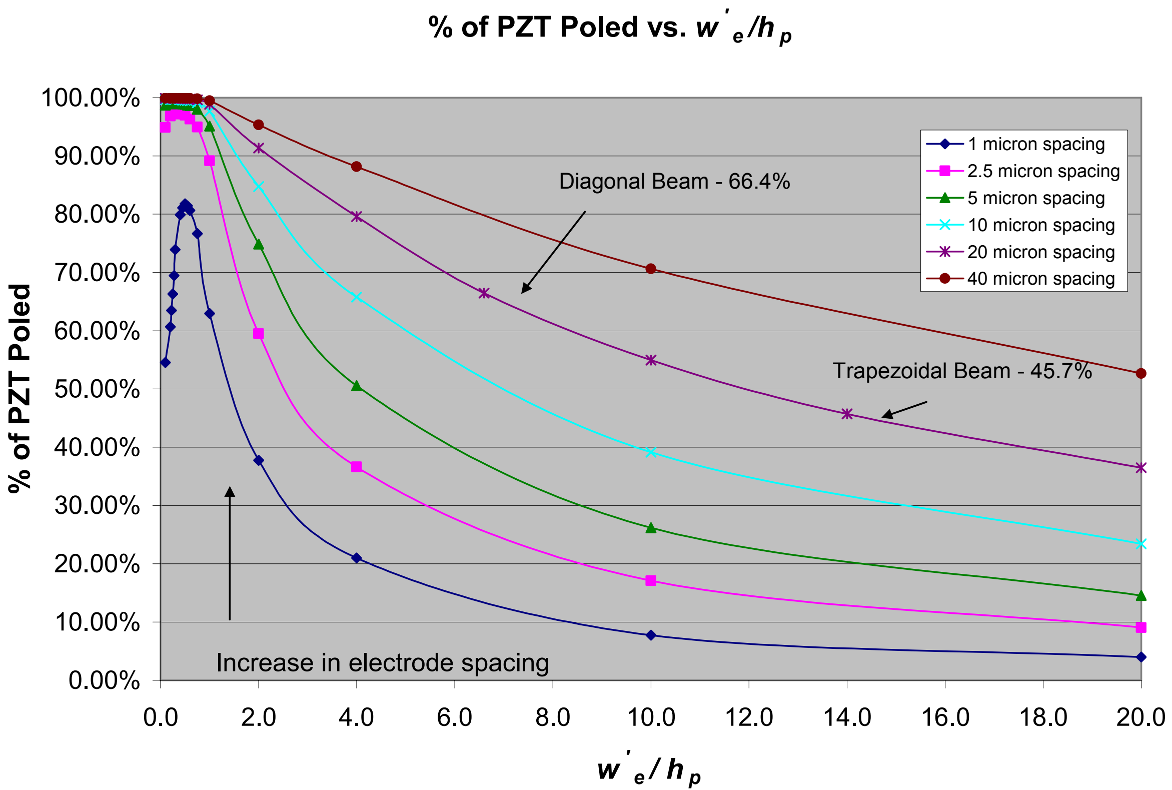

Figure 7.5. ANSYS IDE spacing optimization for various electrode width to piezoelectric layer thickness ratios

Figure 7.5 is a plot of the electrode width to thickness ratios, w'_e/h_p, range from 0.1 to 20.0. Two critical factors were realized from Figure 7.5: 1) larger w'_e/h_p dramatically decreases the percent of PZT poled underneath and between the electrodes and 2) small spacing values also decrease the amount of PZT poled. The MEMS beams tested, are marked on the plot in Figure 7.5. The diagonal beam was calculated to have 66.4% of the PZT poled and the trapezoidal beam was calculated to have 45.7% of the PZT poled.

The reason why the percent poled value changes for various electrode width to thickness ratios, w'_e/h_p, is because of the following. As the electrode width approaches zero the electric field does not have the capability to penetrate all the way through the thickness. Increasing the electrode width allows more electric field to reach the bottom of the PZT. At an electrode width

to piezoelectric layer height ratio (w'_e/h_p) of around 1, the electric field is able to completely penetrate to the bottom of the PZT layer. Larger w'_e/h_p ratio develops excess material/area developed by the increasing electrode width to decrease the amount of PZT poled.

Figure 7.5 shows the amount of PZT poled from the IDE layout. However, this figure has no relation to the direction of the dipoles, just whether the PZT is poled or not. Therefore, in order understand the amount of output associated with an IDE layout similar simulations were performed that analyzed the length direction output from the resulting IDE layout.

The same ANSYS™ model was used to investigate the performance, called the resulting "output" (induced strain or electric field), of the IDE layout. This analysis assumes that the PZT is already perfectly poled in the length direction. But because of the non-uniform electric field created by the electrodes, the output is less than perfect for different IDE geometries. Referring to Figure 7.4 the simulations were conducted as follows:

- The spacing, *s*, between the electrodes was varied from 1.0-40.0 μm
- For each spacing value the, ratio w'_e/h_p was varied from 0.1-20.0
- The input voltage is dependent on the spacing, *s*, and is equal to $V_{poling} = 4s$. This creates what would be a constant electric field if the PZT were located directly between the electrodes.
- After each simulation the electric field inside the PZT layer in the length direction was integrated
- The resulting electric field integration value was averaged by dividing by the PZT area, $(w_e + s)h_p$
- The average electric field in the length direction was then divided by the input electric field value to get a percent of length direction output

Figure 7.6 plots the percent output in length direction for various electrode width to PZT thickness ratios. The larger w'_e/h_p ratios were recorded for each spacing value and the plot is provided in Appendix A.1. It was concluded that after a w'_e/h_p ratio of 2 for any spacing, the percent poled in the length direction, the assumed 3-direction, dramatically reduced.

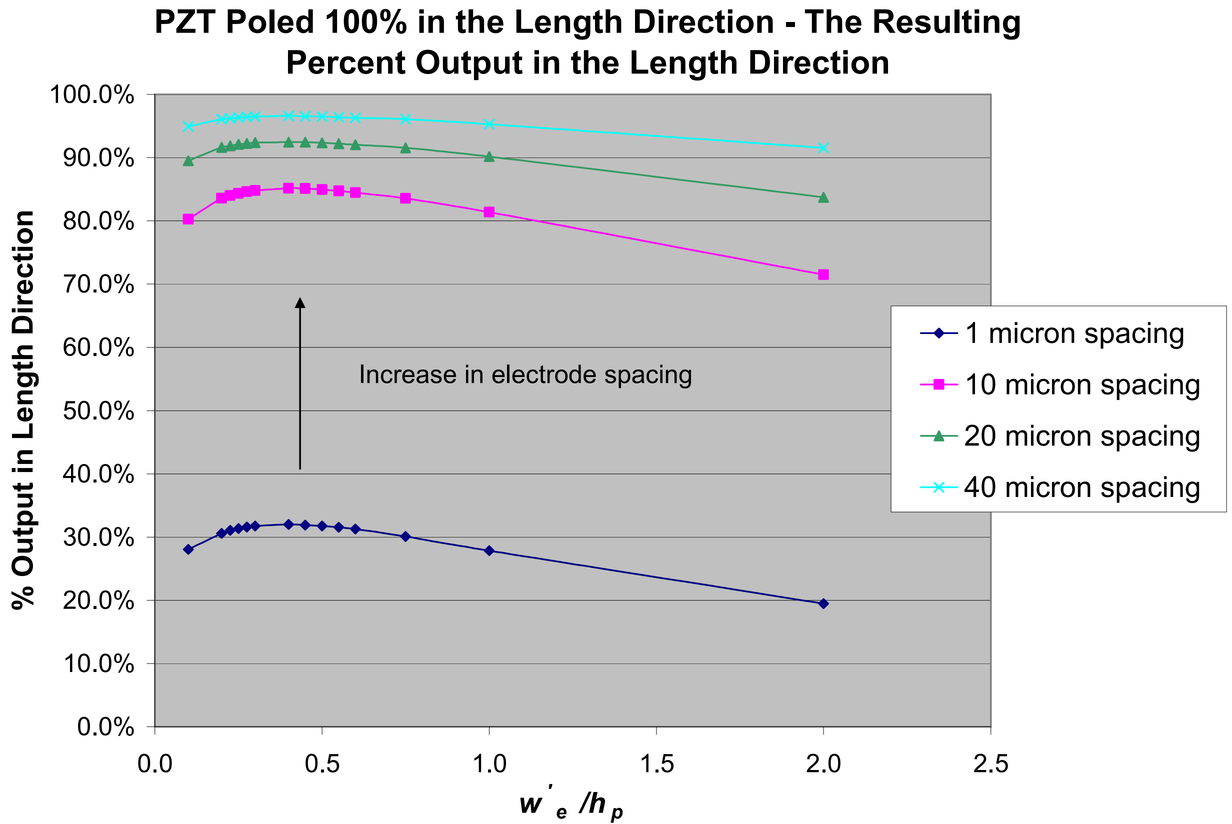

Figure 7.6. The percent output associated for increasing electrode width to thickness ratios and various spacing

For each spacing the w'_e/h_p ratio was optimal at about w'_e/h_p =0.4. Figure 7.6 considers the electrode width divided by two. When w'_e/h_p =0.4 the length direction electric field average was nearly maximum for every spacing value. If an IDE beam has multiple electrodes (as shown in Figure 7.7) than the w'_e/h_p is double. A maximum percent output value of 100% considers the electric field in the PZT layer to be completely pointing in the length direction. From Figure 7.6,

as spacing, *s*, increases the output in the length direction will approach 100%. This is purely because the spacing is becoming relatively much larger than the electrode width.

Doubling optimal w'_e/h_p ratio of 0.4 (to account for back-to-back IDEs) is very close the optimal electrode width to substrate thickness ratio, 0.5, presented in Bowen (2006). The larger optimized ratio value is expected since the current analysis only considers a single IDE pattern in comparison to Bowen's dual IDE pattern (being on both the bottom and top of the piezoelectric material). Adding an IDE pattern on the bottom of the piezoelectric layer allows for the electric field from each IDE to only have to penetrate half way through the thickness, thus allow a smaller electrode width to substrate thickness ratio.

The diagonal beam, Figure 4.7, had a w_e/h_p = 6.6. This ratio corresponds to a percent length direction output value of 60%. The trapezoidal beam, Figure 4.8, had a w_e/h_p = 14. The trapezoidal beam's percent output value is approximately 42%. Table 17 is provided to show the percent of material poled for each spacing at the optimal w_e/h_p ratio of 0.4.

Table 17. Values obtained from FEA for the percent output of PZT that is poled in the Length/3-Direction with respect to electrode spacing

s [μm]	% Output in the Length Direction
1	32.0
10	85.1
20	92.5
40	96.6

7.4 PLANAR INTERDIGITATED ELECTRODE LOSS

Figure 7.7 shows a top view of a typical IDE layout. In order to connect all the electrodes, electrode strips have to run down each side of the PZT's surface. These electrode strips produce an electric field in the width direction.

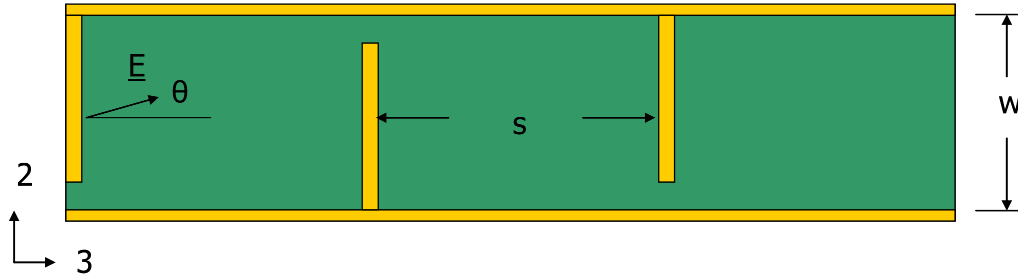

Figure 7.7. Top view of IDE layout

The electric field during poling is now defined by the following equation

$$\underline{E} = E_2 \underline{e_2} + E_3 \underline{e_3} \tag{7.1}$$

where

$$E_2 = \frac{V_p}{w} \tag{7.2}$$

$$E_3 = \frac{V_p}{s} \tag{7.3}$$

$$\theta = arctan\left(\frac{s}{w}\right) \tag{7.4}$$

As w decreases the electric field becomes stronger in the 2-direction and θ increases. The electro-mechanical coupling from a 3-direction stress becomes correspondingly smaller. Figure

7.8 is a plot that illustrates how the percentage of poling is dependent on the beam width to electrode spacing, *w/s* , ratio.

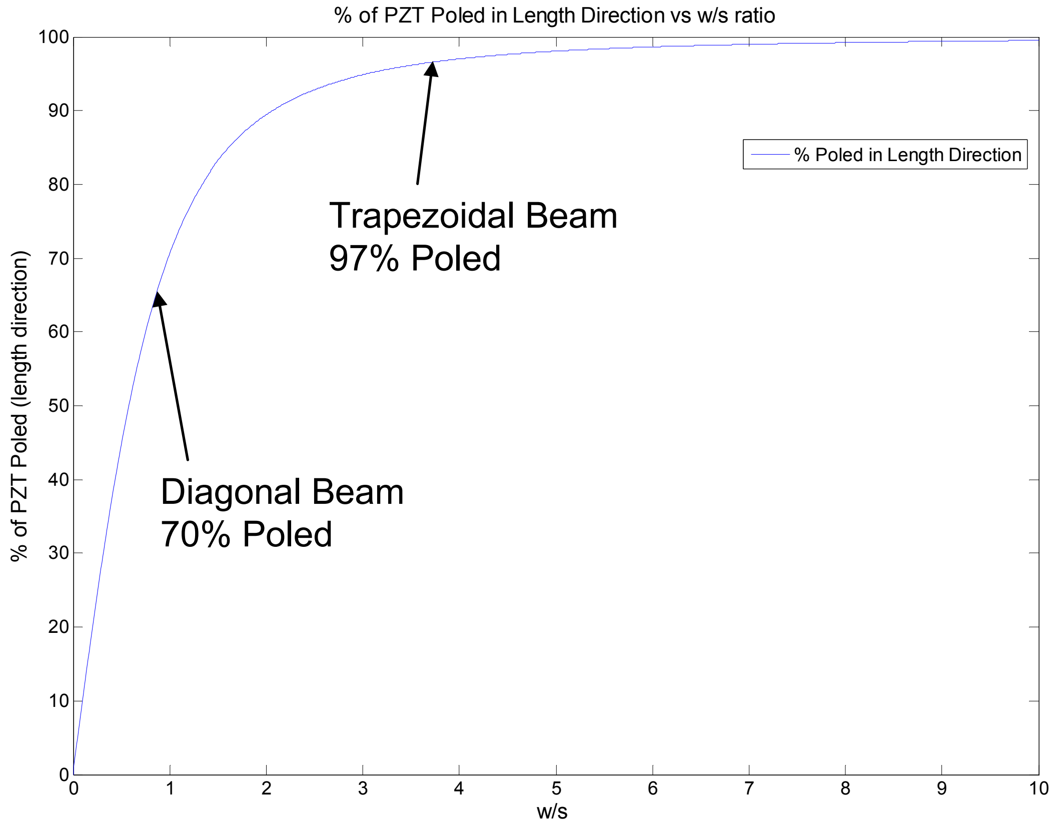

Figure 7.8. % of poling plot under a constant electric field for the IDE layout in Figure 7.6

Figure 7.8 illustrates that if the width to electrode spacing is large enough, the % of poling will be almost 100%. This is because the electric field in the width direction becomes weak relative to the electric field in the length direction.

The diagonal beam, Figure 4.7, had a w/s = 0.99. This ratio corresponds to a percent length direction poling value of 70%. The trapezoidal beam, Figure 4.8, had a w/s = 4 for the first electrode. The first electrode spacing is the area of high stress during first mode bending.

Therefore, it is the most important area to be poled. The trapezoidal beam's percent poling value is approximately 97.0%.

7.5 INTERDIGITATED RESULTS SUMMARY

After doing the FEA poling analysis, optimization and planar electrode loss analyses the following was gained:

- The performance of PZT is highly dependent upon the electrode layout
- Large spacing and small w_e/h_p ratios allow the majority of the PZT to be poled
- The optimal output (best performance) of the IDE beam has a w_e/h_p ratio was 0.8
- Making the width large with respect to the spacing increases the amount of material poled in the 3-direction

There is a design tradeoff between both the poling analysis and optimal ratio discovered versus the beam's width loss. In order to pole the majority of material underneath the electrode the spacing should be large (large enough so the PZT can still be poled without arching) while keeping the w_e/h_p ratio small and ideally around 0.8. But increasing the electrode spacing means the resulting beam's width has to be increased. So depending on the length of the beam, the beam design could be more like a plate.

For MEMS IDE beams the optimal w_e/h_p ratio is nearly impossible to design around for sol-gel PZT films of 0.1 μm – 2 μm thickness. This is because of photolithography limitations. The smallest dimension a standard photolithography process can produce is about 3 μm. Assuming then an electrode width of 3 μm requires, optimally, a sol-gel PZT layer thickness of 3.75 μm. A 3.75 μm thickness is very large for a sol-gel process and is hard to produce

crack/hillock-free. Therefore, for a MEMS IDE device the most important design parameters, excluding the optimal w_e/h_p ratio, are the electrode spacing and width.

The above three bullets help address the issue of when is it advantageous to use IDE structure in comparison to a d_{31} unimorph structure. Since d_{33} is typically twice as large as d_{31} for PZT the percent of material poled in 3-direction should be greater than 50%. In order to obtain the total value of the poled PZT, the percent poled from the IDE optimization must be multiplied by the percent poled in planar analysis. This relationship is shown in equation (7.5).

$$(\% poled)_{nonuniform} \times (\% poled)_{planar} \times (\% output)_{IDEoptimization} > 50\% \tag{7.5}$$

If (7.5) is not met than one should design a d_{31} unimorph.

The percent poled values obtained for the diagonal and trapezoidal beams in Sections 7.3-7.4 are listed in Table 18. From the results in Table 18, the diagonal beams should have been designed to be d_{31} unimorphs instead of d_{33} unimorphs. The trapezoidal beams total percent poled value is 18.6%. Consequently, a d_{31} unimorph should have also been designed for the trapezoidal beams instead of a d_{33} unimorph. If the electrode width would have been reduced into half the trapezoidal beam could have worked well as a d_{33} unimorph having 58% of the PZT poled. However, a caveat of the trapezoidal design is since the width decreases for the trapezoidal beams the total percent poled value will decrease at spacing areas farther away from the base.

Table 18. Total of PZT poled in the length direction for diagonal and trapezoidal beams

	% Poled	% Output -IDE	% Output -Width	Total Percent Output - equation (7.5)
Diagonal Beam	66.4%	60.7%	70.0%	28.2%
Trapezoidal Beam	45.7%	42.0%	97.0%	18.6%

In order to help meet (7.5) the IDE d_{33} unimorph should be designed to have the largest spacing and width allowable. Both of these parameters will increase the percent poled factors. After determining the amount the PZT is poled in the length direction, one can make a better design decision on whether to use a d_{33} unimorph or a d_{31} unimorph.

8.0 CONCLUSION

Two types of MEMS cantilever beams, d_{31} unimorph and d_{33} unimorph, were mathematically modeled. Equations (3.35-3.36) are developed in order to compare the performance of each design. The d_{33} unimorph equations were derived using a percent poling factor. The percent poling factor rises from the non-uniform electric field during piezoelectric layer poling. A modal analysis was also conducted for the d_{33} unimorph using ANSYS™.

Following the mathematical models and ANSYS™ simulations, two types of MEMS d_{33} unimorph beams were tested. The first type tested was the diagonal beam. The diagonal beam performed poorly and no difference between open-circuit and short-circuit frequencies was detected. The diagonal beam was thought to have a very low percent poling factor. Subsequently, because the diagonal beams did not produce any good results, the trapezoidal beams were tested. The wide base associated with the trapezoidal beams was thought to enhance the percent poling factor. A percent tuning range of 0.2% - 0.6% was measured.

The next experimental work done was testing the change in frequency of a macro-scale PZT d_{31} unimorph. Frequency measurements were taken as the length of the electrode, relative to the base of the beam, was decreased via chemical etching. The experimental results showed that the stiffness of the beam could be significantly increased as the beam's electrode length decreased.

Next, the percent poling factor was investigated. ANSYS™ was used to simulate various electrode width to PZT layer thickness ratios (w_e/h_p) for four different electrode spacing values. Additionally, a percent output in the length direction was determined for each spacing w_e/h_p ratio. For every electrode spacing value, an optimal w_e/h_p was found to consistently be 0.8. As spacing increased the percent output in the length direction also increased.

Finally, the effect of having the electrodes run down both sides of a beam was examined. Having larger beam width to spacing ratios (w/s) was shown to increase the percent poling factor. This is because as the width increases the electric field contribution in the width direction becomes smaller and the beam is, therefore, poled more in the length direction.

The work presented will assist in the design of MEMS or macro scale piezoelectric devices. Piezoelectric actuators, sensors, or harvesters can be designed in a more flexible manner allowing the designer to understand the caveats associated with a d_{33} unimorph devices. Choosing the proper intedigitated electrode layout and beam dimensions can nearly double the performance of a d_{33} unimorph device. Thus, designing a proper d_{33} unimorph device will increase the actuator's actuation, the sensor's sensitivity and the harvester's energy harvesting.

8.1 FUTURE WORK

In Section 6.2 a marco-scale bimorph d_{31} beam was dynamically tested. After each frequency measurement was taken the beam's electrode was etched an additional 1 mm from the free end. As the electrode was etched farther away from the free end, the beam's natural frequencies increased correspondingly. This increase in frequency effect was thought to be from the non-

constant stress in the beam. Therefore, future work is needed to develop a model that can predict the type of behavior shown experimentally.

In Chapter 4 when the MEMS beams were released the beams curled. This was due from the extra layer of SiO_2 deposited via low pressure chemical vapor deposition (LPCVD). In order to alleviate beam curl, it is recommended in the future to use wafer's that have a layer of SiN_x deposited on top of the Si followed by the LPCVD SiO_2. Additionally, wafer curvature measurements after each processing deposition will help determine how much residual stress is in each layer.

The XeF_2 undercut also needs to be addressed. One recommendation is extend the electrodes past the base of the beam. When the beams are undercut a portion of the beam's base is subject to bending stress. Therefore, extending the electrodes past the base can help capture some of the stress exerted in the undercut region. Below, the future work is summarized in bullets.

Finally, develop and test IDE beams that are relatively wide in comparison to electrode spacing. Also the electrode width to PZT thickness ratio should be reduced to the smallest tangible by MEMS processing. The IDE beams should then be compared to d_{31} beams on the same MEMS wafer. Comparing the performance of d_{33} and d_{31} beams will help prove the effectiveness of the percent poling and percent output topics covered in Section 7.3-7.4.

- Produce a new mathematical model that takes into account the linearly varying electric field when modeling piezoelectric beams
- Experimentally prove the mathematical model described above
- Address the curling issue by removing the extra SiO_2 layer and making wafer curvature measurements after each layer is deposited during processing

- Compensate for the XeF_2 undercut by extending the base of each beam
- Develop and test IDE beams that have dimensions that correspond to small electrode width to PZT layer thickness ratios and large beam widths. Compare the develop IDE beams to similarly developed d_{31} beams.

APPENDIX A

A.1 AVERAGE ELECTRIC FIELD PLOT

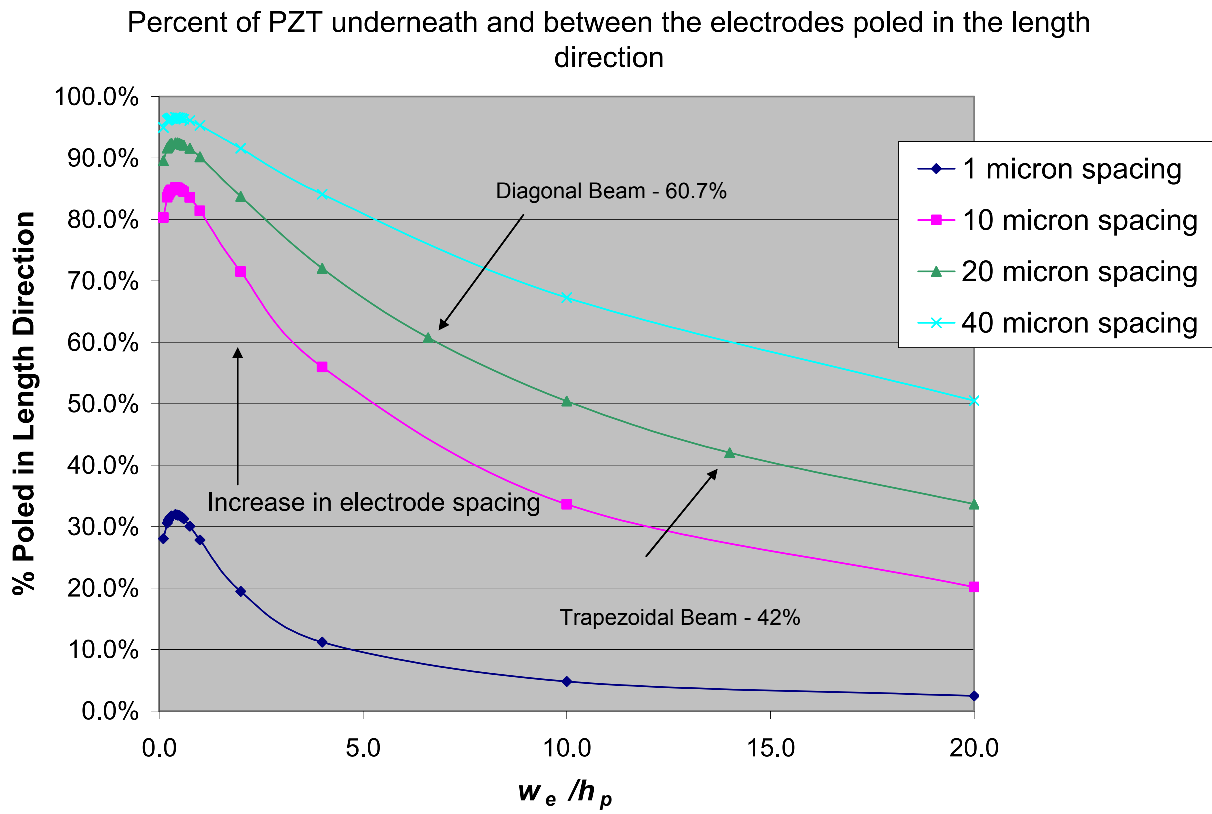

BIBLIOGRAPHY

ANSYS™, Coupled-Field Analysis Guide, Release 10.0 Documentation for ANSYS

Baerwald, H. G. (1957). *Phys. Rev.* 105, 480-6

Ballato, A., Gualtieri, J. G., Kosinski, J. A. (1995). Ferroelectric materials for thin-film and membrane resonators. IEEE.

Borrelli, A., Horgan, C. O., Patria, M. C. (2006). Saint-Venant end effects for plane deformations of linear piezoelectric solids. *International Journal of Solids and Structures*, 43, p. 943-956.

Bowen, C. R., Nelson, L. J., Stevens, R. (2006). Optimisation of interdigitated electrode for piezoelectric actuators and active fibre composites. *J. Electroceram*, 16:263-269.

Charnegie, D. (2007). Analysis and Fabrication of MEMS Tunable Piezoelectric Resonators. M.S. Thesis, University of Pittsburgh, Pittsburgh.

Che, L., Cheng, J., Yu, S. (2007). The effect of $LaNiO_3$ buffer layer thickness on the electric properties of $Ph(Zr_{0.53}Ti_{0.47})O_3$ thin films deposited on titanium foils. *Materials Letters*, v 61, n 14-15, p. 3068-3070.

Chen, B., Huang, C., Wu L. (2003). Crack alleviation processing of lead zirconate titanate thin films deposited by sol-gel method. *Thin Solid Films* 441, p. 13-18.

Cheng, J., Meng, Z. (2001). Thickness-dependent microstructures and electric properties of PZT films derived from sol-gel process. *Thin Solid Films*. 385, p. 5-10.

Choi, W., Jeon, Y., Sood, R. (2006). Energy harvesting MEMS device based on thin film piezoelectric cantilevers. *Journal of Electroceramics*, 17, p. 543-548.

Chou, Ch., Tsai, S., Tu, W. (2007). Low-temperature processing of sol-gel derived $Pb(Zr,Ti)O_3$ thick films using CO_2 laser annealing. *Journal of Sol-Gel Science and Technology*, v 42, n 3, p. 315-322.

Clark, W.W. (2000). Vibration Control with State-Switched Piezoelectric Materials. *J of Intelligent Material Systems and Structures.* Vol. 11.

Collet, M., Walter, V.,Delobelle, P. (2004). Active damping with piezoelectric MEMS devices. *Smart Structures and Materials 2004: Damping and Isolation*, Proc. Of SPIE Vol. 5386.

Cooney, T. G., Francis, L. F. (1996). Processing of sol-gel derived PZT coating on non-planar substrates. *Journal Micromech. Microeng*. 6 261-300.

Dai, C., Xiao, F., Lee, C. (2004). Thermal effects in PZT: diffusion of titanium and recrystallization of platinum. *Materials Science and Engineering*. A 384, p. 57-63.

Date, M., Kutani M., Sakai, S. (2000). Electrically controlled elasticity utilizing piezoelectric coupling. *Journal of Applied Physics*, V87 Number 2.

Davis, C. L., Lesieutre, G. A. Dosch J., (2003). A tunable electrically shunted piezoceramic vibration absorber. SPIE Vol. 3045.

Faheem, Y., Shoaib, M. (2006). Sol-gel processing and characterization of phase-pure lead zirconate titanate nano-powders. *J. Am. Ceram. Soc.* 89 [6] 2034-2037.

Frederick A. A., Clark, W. W., Hu, H. (2005). Analysis of a tunable piezoelectric resonator using interdigitated electrodes. Symposium on Dynamics and Control of Micro and Nanosystems. IMECE 2005-80446.

Frederick, A. (2006). Analysis and Fabrication of MEMS Tunable Piezoelectric Resonators. M.S. Thesis, University of Pittsburgh, Pittsburgh.

Ginsberg, J. (2005). *Advanced Engineering Dynamics*, 2nd Edition, 2005, p. 18.

Guan, M. Liao, W. (2006). On the energy storage devices in piezoelectric energy harvesting. *Smart Structures and Materials 2006: Damping and Isolation,* Proc. of SPIE Vol. 6169.

Hong, Y. K., Moon, K. S., Levy, M. (2006). Single-crystal film piezoelectric sensors, actuators and energy harvesters with interdigitated electrodes. *Ferroelectric*, 342:1-13.

Hou, M. T., Chen, R. (2003). Effect of width on the stress-induced bending of micromachined bilayer cantilevers. *J. Micromech. Microeng.*, 13, p. 141-148.

Hsueh, C. C., Mecartney, M. L. (1990). TEM Analyses of Sol-Gel Derived and Sputtered PZT thin films, NTIS 8p.

IEEE Std 176-1997, IEEE Standard on Piezoelectricity, The Institute of Electrical and Electronics Engineers, 1997.

Inman, D. J., *Engineering Vibration*, 2nd Edition, 2001, p. 465.

Jeon, Y., Sood, R., Jeong, J. (2005). MEMS power generator with transverse mode thin film PZT. *Sensors and Actuators*, A 122, p. 16-22.

John, S., Sirohi, J., Wang, G. (2005). Comparison between PMN and PZT as a driving element in a compact hybrid actuator. *Proceedings of ISSS 2005*, ISSS-2005/SA-15.

Kim, S., 2002. Low Power Energy Harvesting with Piezoelectric Generator. Ph.D Dissertation, University of Pittsburgh, Pittsburgh.

Kim, S.G. (2004). *Piezoelectricity*. Retrieved from http://ocw.mit.edu/NR/rdonlyres/Mechanical-Engineering/2-76Fall-2004/972E0CFB-827D-4CAD-85E6-99EEBD74AFF1/0/lecture_7prt2.pdf.

Ko, F., Hsu, Y., Wang, M. (2007). Fabrication of a gas sensor with a piezoelectric PZT film deposited by a novel hydrothermal microwave-assisted annealing. *Proceedings of the 32nd International Conference on Micro- and Nano- Engineering,* p. 1300-1304.

Kouvatov, A. Steinhausen, R.,Hauke T. (2002). Poling behavior of functionally gradient material bending devices. *Ferroelectrics*, Vol. 273, p. 95-100.

Kwon, Y., Lee, I., Lee, W. (1999). Effect of sol-gel precursors on the grain structure of PZT thin films. *Materials Research Bulletin*, Vol. 34, No. 5, p. 749-760.

Lee, B., He, J., Wu, W. (2006). MEMS generator of power harvesting by vibrations using piezoelectric cantilever beam with digitate electrode. *Smart Structures and Materials 2006: Damping and Isolation*, Proc. of SPIE Vol. 6169.

Lee, J., Lee, S., Park, C. (2007). Effects of residual stress on piezoelectric property of $Pb(Zr,Ti)O_3$ films fabricated by sol-gel process. *Journal of Sol-Gel Science and Technology*, v 42, n 3, *Special Issue on Sol-Gel and Solution-Derived Ferroelectric Materials*, p. 305-308.

Lesieutre, G., Ottman, G., Hofmann, H. (2004). Damping as a result of piezoelectric energy harvesting. *Journal of Sound and Vibration*, 269, p. 991-1001.

Lowrie, F., Cain, M., Stewart M. (1999). Finite element modeling of electroceramics. NPL Report CMMT(A)150, ISSN: 1361-4061.

Mo, C., Kim S., Clark, W. (2005). Analysis of Power Generating Performance for Unimorph Cantilever Piezoelectric Beams with the Interdigitated Electrode. *Proceedings of IDETC/CIE.*

Muriuki, M. 2004, *An Investigation into the Design and Control of Tunable Piezoelectric Resonators*, Ph.D Dissertation, University of Pittsburgh, Pittsburgh.

Nieva, P. M.,McGruer, N. E., Adams, G. G. (2006). Air viscous damping effects in vibrating microbeams. *Smart Structures and Materials 2006: Damping and Isolation*, Proc. of SPIE Vol. 6169.

Ohya, Y., Yahata, Y., Ban, T. (2007). Dielectric and piezoelectric properties of dense and porous PZT films prepared by sol-gel method. *Journal of Sol-Gel Science and Technology*, v 42, n 3, *Special Issue on Sol-Gel and Solution-Derived Ferroelectric Materials*, p. 397-405.

Parashar, S. K., Wagne, U., Hagedorn, P. (2005). Nonlinear shear-induced flexural vibrations of piezoceramic actuators: experiments and modeling. *Journal of Sound and Vibration*, 285, p. 989-1014.

Park, C., Kim, S., Park, G. (2005). Orientation control of lead zirconate titanate film by combination of sol-gel and sputtering deposition. *Journal of Materials Research*, v 20, n 1, p 243-6.

Popov, E., Engineering Mechanics of Solids, 2nd Edition, 1999, p 636-641.

Roundy, Shad, (2005). On the effectiveness of vibration-based energy harvesting. *Journal of Intelligent Material Systems and Structures.* Vol. 16.

Ruan, X., Danforth, S. C., Safari, A. (2000). Saint-Venant end effects in piezoceramic materials. *International Journal of Solids and Structures*, 37, p. 2625-2637

Senturia, S, *Microsystem Design*, 2001, p. 224.

Shi, Z. F., Xiang, H. J., Spencer, B. F. Jr. (2006). Exact analysis of multi-layer piezoelectric/composite cantilever. *Smart Mater. Struct.*, 15, p. 1447-1458.

Slaugther W S, *The Linearized Theory of Elasticity*, 2002, p 260-289.

Sodano, H. A., Inman, D. J., Park, G., (2005). Comparison of piezoelectric energy harvesting devices for recharging batteries. *Journal of Intelligent Material Systems and Structures*. Vol. 16.

Sodano, H. A., Inman. D. J., Park, G. (2005). Generation and storage of electricity from power harvesting devices. *Journal of Intelligent Material Systems and Structures*, Vol. 16.

Sodano, H. A., Lloyd, J., Inman, D. J. (2004). An experimental comparison between several active composite actuators for power generation. *Smart Structures and Materials 2004*, Proc. Of SPIE, Vol. 5390.

Sodano, H. A., Park, G., Inman, D. J. (2004). Estimation of electric charge output for piezoelectric energy harvesting. *Strain,* **40**, p. 49-58.

Stoney G, The tension of metallic films deposited by electrolysis, Proc. Roy. Soc. (Lond.) A 82 (1909) 172-175.

Sze, S.M. (Ed.). (1994). *Semiconductor Sensors*. New York: John Wiley & Songs, Inc.

Wang, Z., Kokawa, H., Takizawa, H. (2007a). Low-temperature processing of lead zirconate titanate thin films by 28 GHz microwave irradiation for MEMS application. *Proceedings of SPIE*, v 6413, *Smart Materials IV*, p. 641308.

Wang, Z., Usuki, H., Kumagai, T. (2007b). Microstructure and electrical properties of lead zirconate titanate thin films deposited by sol-gel method on $La_{0.7}Sr_{0.3}MnO_3/SiO_2/Si$ substrate. *Journal of Sol-Gel Science and Technology*, v 42, n 3, p. 375-379.

Wu, W., Chen, Y., Lee, B. (2006). Tunable resonant frequency power harvesting devices. *Smart Structures and Materials 2006: Damping and Isolation*, Proc. of SPIE Vol. 6169.

Xu, B., Ye, Y. Cross, L. E., (1999). Dielectric hysteresis from transverse electric fields in lead zirconate titanate thin films. *Applied Physics Letters*, Vol. 74, Number 23, 7.

Zhang, Q. Q., Gross, S. J., Tadigadapa, S. (2003). Lead zirconate titanate films for d_{33} mode cantilever actuators. *Sensors and Actuators*, A 105, p. 91-97.

Zhao, H., Ren, T., Zhang, N., (2003). High-frequency properties of PZT for RF-communication applications.

Zhu, M., Kirby, P. B. (2006). Design study of piezoelectric micro-machined mechanically coupled cantilever filters using a combined finite element and microwave circuit analysis. *Sensors and Actuators*, A 126, p. 417-424.